



POLITECNICO
MILANO 1863

DEPARTMENT OF PHYSICS
DOCTORAL PROGRAM IN PHYSICS

**Physical Confinement *versus* Nano-
Electrochemistry: Exploring Adsorption-
Induced Reconstruction of Vicinal Cu(111)
Surfaces Interacting with Sulfate Anions**

Doctoral Dissertation of:
CLAUDIA FILONI

Supervisor:
Prof. Gianlorenzo Bussetti

Co-supervisor:
Prof. Klaus Wandelt

Tutor:
Prof. Alberto Brambilla

October, 14th 2024-XXXVI Cycle

Summary

1. INTRODUCTION	1
1.1 The Emphasis on the Solid-Liquid Interface	1
1.2 The Emergence of Nano-Electrochemistry in Miniaturization and Low-Dimensional Materials	3
1.2.1 The Role of Vicinal Surfaces: Bridging the Gap Between UHV and Electrochemical Systems	7
1.3 EC-STM in Corrosion Analysis: The Case-Study of the Copper System	11
2. CU(111) IN H ₂ SO ₄ 5 MM	23
2.1 The Interaction Between Cu(111) Surface and SO ₄ ²⁻ Anions	23
2.1.1 Sulfate Adsorption and Moiré Structure Formation	35
2.1.2 Desorption Process Overview	38
2.1.3 Unveiling the Moiré-Superstructure: A Comprehensive Analysis through STM Imaging	39
2.2 The Impact of Tunneling Current on the STM Resolution of the Moiré-superstructure	43
3. EXPERIMENTAL EQUIPMENT AND THEORETICAL DESCRIPTION	49
3.1 The Electric-Double Layer (EDL)	49
3.2 STM (Scanning Tunneling Microscope) Basic Working Principle	53
3.3 Electrochemical Tunneling	59
3.4 Evolution of Electrochemical STM Application Over the Years	61
3.5 AFM (Atomic Force Microscope) Basic Working Principle	62
3.5.1 AFM Imaging Modes	64
3.5.2 Fundamentals of Atomic Force Microscope	66
3.6 Electrochemistry	69
3.6.1 The Standard Hydrogen Electrode (SHE)	73
3.7 Understanding Vicinal Surfaces: Key Notions About Their Formation, Structure and Fundamental Principles	75

4. EXPERIMENTAL METHODS	79
4.1 Electrochemical Scanning Probe Microscope (EC-SPM)	79
4.2 Tip Preparation	83
4.3 Solution Preparation (H ₂ SO ₄ 5mM)	85
4.4 Surface Preparation.....	88
4.4.1 Electropolishing	88
4.5 Setting the Experiment.....	89
4.6 Data Analysis.....	92
4.7 Calibration of the Microscope	92
5. EXPERIMENTAL RESULTS AND DISCUSSION.....	95
5.1 Initiating the Experiment: Setup and Initial Procedures.....	95
5.2 Cu(111) in Dilute H ₂ SO ₄ Solution.....	97
5.2.1 Bare Cu(111) in Dilute H ₂ SO ₄ Solution	100
5.2.2 Moiré-superstructure Formation on Cu(111) Surface in Dilute H ₂ SO ₄ Solution	104
5.2.3 Interpretation of Surface Phenomena on Cu(111) in Dilute H ₂ SO ₄ Solution Through Literature Images	110
5.3 Introduction to Vicinal Cu(111) Surfaces Immersed in Diluted H ₂ SO ₄ Solution	114
5.4 Sulfate Adsorption on Vicinal Surfaces: Structural Analysis of Cu(221) and Cu(21 21 16) Surfaces.....	115
5.5 Cu(21 21 16) in Dilute H ₂ SO ₄ Solution: Expected vs Observed Surface Structure.....	116
5.6 Cu(221) in Dilute H ₂ SO ₄ solution	118
5.7 Clarified Analysis of Step Edges on the Sulfate-Covered Cu(111) Surface .	120
5.8 Discussion of Cu(21 21 16) and Cu(221) in Dilute H ₂ SO ₄ solution.....	121
5.9 EC-AFM of Cu(111) in Dilute H ₂ SO ₄ Solution during Anodic Surface Dissolution Process	129
6. CONCLUSION	137

Acronyms

AFM	Atomic Force Microscopy
CE	Counter Electrode
CV	Cyclic Voltammetry
EC-AFM	Electrochemical Atomic Force Microscope
EC-SPM	Electrochemical Scanning Probe Microscope
EC-STM	Electrochemical Scanning Tunneling Microscope
EDL	Electric Double-Layer
emf	electro-motive force
FCC	Face-Centered Cubic
HER	Hydrogen Evolution Reaction
HOPG	Highly Oriented Pyrolytic Graphite
LDOS	Surface Local Density of States
LEED	Low-Energy Electron Diffraction
OER	Oxygen Evolution Reaction
ORR	Oxygen Reduction Reaction
RE	Reference Electrode
SEM	Scanning Electron Microscopy
SHE	Standard Hydrogen Electrode
SHINERS	SHELL-Isolated Nanoparticle-Enhanced Raman Spectroscopy

Acronyms

SPM	Scanning Probe Microscopy
STM	Scanning Tunneling Microscopy
UHV	Ultra-High Vacuum
WE	Working Electrode
XRD	X-Ray Diffraction
XPS	X-ray Photoelectron Spectroscopy

Index of Figures

1. Figure 1.1: [37] STM images of an H₂TMPyP layer on iodide modified Cu(111) (phase I). (a) Monolayer with three rotational domains; image parameters: 41.10 nm × 41.00 nm; I_t = 0.1 nA, U_b = 416 mV, E = -350 mV vs Ag/AgI. (b) Molecular arrangement; image parameters: 27.77 nm × 27.70 nm; I_t = 0.1 nA, U_b = 135 mV, E = -350 mV vs Ag/AgI; inset: molecular rotation by 17° vs direction of rows. The small arrows indicate crystallographic directions (211) and (110) of the Cu(111) substrate. 12
2. Figure 1.2: [50] Electrochemistry of the systems Cu(111) (solid line) (modified from ref. [51]) and Cu(001) (dashed line) (modified from ref. [52]) in 0.1 M NaOH; left: OH adsorption is visible in the underpotential range of oxidation for Cu(111) (modified from ref. [53]) and Cu(001) (modified from ref. [52]). 14
3. Figure 1.3: [50] (a) EC-STM image of metallic Cu(111) (modified from ref. [52]) in 0.1 M NaOH at -0.80 V_{SHE} after reduction of the native oxide. (b-d) Series of EC-STM images showing the growth of the OH adsorbate (ads) layer on Cu(111) in 0.1 M NaOH at -0.6 V_{SHE}; adlayer islands and bare substrate are marked ad and M, respectively (modified from ref. [53]). 16
4. Figure 1.4: [50] EC-STM image of OH adsorbate structure formation on Cu(111) in the potential range before oxidation, in 0.1 NaOH / 0.01 NaCl after a potential step to -0.58 V_{SHE} (from ref. [49]). 17
5. Figure 1.5: [54] Cyclic voltammogram of Cu(111) in 0.1 M HClO₄; scan rate dE/dt = v_{scan} = 10 mV/s; H: hydrogen evolution; O/O': oxygen-containing species ad-/desorption; D: anodic copper dissolution; X, unknown..... 18
6. Figure 1.6: [54] STM images of the (4 × 4) structure in pure 0.1 M HClO₄ at different tunneling parameters, 6.2 nm × 6.2 nm. (a) E = -150 mV, U_b = 50

	mV, $I_t = 20$ nA; (b) $E = -325$ mV, $U_b = 5$ mV, $I_t = 50$ nA; (c) $E = -250$ mV, $U_b = 100$ mV, $I_t = 10$ nA; (d) $E = -250$ mV, $U_b = 40$ mV, $I_t = 40$ nA.	19
7.	Figure 1.7: [54] (a) STM image of the (1×1) Cu(111) structure under pure 0.1 M HClO ₄ , 4.3 nm \times 4.3 nm; $E = -160$ mV, $U_b = 4$ mV, $I_t = 50$ nA. (b) Surface topography at more positive potentials, 40.6 nm \times 40.6 nm; $E = +50$ mV, $U_b = 100$ mV, $I_t = 1$ nA.	20
8.	Figure 1.8: [54] STM images of the (4×4) structure in the presence of cinchonidine at different tunneling parameters, 6.2 nm \times 6.2 nm. (a) $E = -300$ mV, $U_b = 80$ mV, $I_t = 20$ nA; (b) $E = -300$ mV, $U_b = 60$ mV, $I_t = 20$ nA; (c) $E = -300$ mV, $U_b = 40$ mV, $I_t = 50$ nA; (d) $E = -350$ mV, $U_b = 9$ mV, $I_t = 50$ nA.	21
9.	Figure 2.1: [45] Pourbaix diagram calculated at $[Cu^{2+}] = 10\mu\text{M}$ and $[SO_4^{2-}] = 5\text{mM}$ at 25°C . The area highlighted in light blue, that corresponds to $\text{pH} = 2$, is the region of our interest, for a diluted solution of H ₂ SO ₄ 5 mM.	24
10.	Figure 2.2: [45] Typical steady-state cyclic voltammogram of a Cu(111) electrode in 5mM H ₂ SO ₄ ; scan rate $dE/dt = v_{\text{scan}} = 10\text{mV/s}$	25
11.	Figure 2.3: [60] 26 nm \times 26 nm; rotational domains (1, 2, 3) of the sulfate-induced Moiré structure; bias voltage $U_b = 100$ mV; tunneling current $I_t = 1$ nA; electrode potential $E = 210\text{mV}$	26
12.	Figure 2.4: [45] Moiré pattern formed on Cu(111) in 5mM H ₂ SO ₄ as reported by Maurice et al. [61]. The STM images are captured at $U_b = -0.1 V_{\text{SHE}}$, $E_{\text{tip}} = 0.15$ V, $I_t = 1$ nA. (a) The Moiré pattern at nanometric resolution, 50 nm \times 50 nm, z range = 1.13 nm; (b) Atomic resolution showing the adsorbed sulfate ions and the co-adsorbed cations in a zigzag arrangement in between the sulfate rows, 7.9 nm \times 7.9 nm, z range = 0.12 nm.	27
13.	Figure 2.5: [45] (a) Model of the structure of the sulfate adlayer forming a $(\sqrt{3} \times \sqrt{7})$ structure on the Cu(111) surface.	28

14. Figure 2.6: [63] Moiré structure, $7.6 \text{ nm} \times 7.6 \text{ nm}$, $I_t = 1 \text{ nA}$, $U_b = -120 \text{ mV}$, $E = -56 \text{ mV}_{\text{RHE}}$ 31

15. Figure 2.7: [60] (a) In situ STM image of the sulfate-free Cu(111) electrode measured potentiostatically in solution. Image size $3 \text{ nm} \times 3 \text{ nm}$; bias voltage $U_b = -10 \text{ mV}$; tunneling current $I_t = 30 \text{ nA}$; electrode potential $E = -215 \text{ mV}_{\text{RHE}}$; positive potential sweep. 32

16. Figure 2.8: [60] Morphological changes induced by sulfate adsorption on Cu(111) in $5 \text{ mM H}_2\text{SO}_4$ solution. (a) Before sulfate adsorption; image size $340 \text{ nm} \times 340 \text{ nm}$; bias voltage $U_b = -20 \text{ mV}$; tunneling current $I_t = 1 \text{ nA}$; electrode potential $E = -266 \text{ mV}_{\text{RHE}}$, positive potential sweep. (b) After sulfate adsorption; $340 \text{ nm} \times 340 \text{ nm}$; $U_b = -20 \text{ mV}$; $I_t = 1 \text{ nA}$; $E = 155 \text{ mV}_{\text{RHE}}$, positive potential sweep. 34

17. Figure 2.9: [60] (a-c) Morphology of the Cu(111) surface after desorption of the sulfate adlayer as a function of time; recording time for all three images 15 minutes. Tunneling parameters for all images: Size $256 \text{ nm} \times 256 \text{ nm}$; bias voltage $U_b = -41 \text{ mV}$; tunneling current $I_t = 10 \text{ nA}$; electrode potential $E = -210 \text{ mV}_{\text{RHE}}$, positive potential sweep. 35

18. Figure 2.10: [60] (a)–(e) Series of STM images illustrating the process of sulfate-induced Moiré formation. The tunneling parameters for all images are as follows: size $101 \text{ nm} \times 101 \text{ nm}$; bias voltage $U_b = 169 \text{ mV}$, tunneling current $I_t = 1 \text{ nA}$ and electrode potential ($E = -70 \text{ mV}$) versus RHE. The entire series was captured over a duration of 10 minutes. Notably, a Moiré-covered island begins to form in the upper left corner of images (d) and (e). Panel (f) presents a height profile along the white line in (b), revealing the onset of Moiré formation at the upper edge of a step..... 36

19. Figure 2.11: [55] Series of STM images showing the decay of the Moiré adlayer; total recording time 15 minutes. Notice the persistence of small Moiré patches at the upper step edges, even when the sulfate coverage is reduced to

- very low levels (panel h). Tunnelling parameters for all images: size 84 nm × 84 nm; bias voltage $U_b = 40$ mV, tunneling current $I_t = 1$ nA; electrode potential $E = 210$ mV vs RHE.....39
20. Figure 2.12: [55] Cu(111) in 5 mM H₂SO₄, step orientation of a sulfate covered copper surface: (a) 102 nm × 102 nm; $I_t = 1$ nA, $U_b = 166$ mV, $E = -465$ mV; (b) 43 nm × 43 nm; $I_t = 1$ nA, $U_b = 166$ mV, $E = -465$ mV; (c) 29 nm × 29 nm; $I_t = 1$ nA; $U_b = 166$ mV, $E = -465$ mV. E was measured vs (Hg|Hg₂SO₄)/V..40
21. Figure 2.13: [60] The image depicts a sulfate-stabilized copper step on a Cu(111) electrode in a 5 mM H₂SO₄ solution. Observe that only the upper terrace is covered by the Moiré structure, while the lower terrace remains uncovered. Additionally, the step aligns with the rows of Moiré-units rather than with the sulfate rows. One Moiré-unit is indicated in the image. Imaging parameters are as follows: size 13 nm × 13 nm; bias voltage $U_b = -70$ mV, tunneling current $I_t = 1$ nA, electrode potential $E = -80$ mV_{RHE}, during a positive potential sweep.41
22. Figure 2.14: [55] Cu(111) in 5 mM H₂SO₄, STM series showing the formation of the Moiré structure: (a–h) 92 nm × 92 nm. (a) $I_t = 1$ nA; $U_b = 86$ mV, $E = -850$ mV. (b) $I_t = 1$ nA; $U_b = 86$ mV, $E = -800$ mV. (c–h) $I_t = 1$ nA; $U_b = 66$ mV, $E = -750$ mV; the time interval between successive images is 70 s; the white dots in panel (c) represent the outline of the copper step shown in panel (b), illustrating how the copper terrace stretches during the Moiré formation. E was measured vs (Hg|Hg₂SO₄)/V.42
23. Figure 2.15: [60] Dependence of the sulfate-induced structure on Cu(111) as a function of tunneling conditions. The tunneling parameters of the STM images are: (a) image size 13.7 nm × 13.7 nm; bias voltage $U_b = -2$ mV; tunneling current $I_t = 10$ nA. (b) 13.7 nm × 13.7 nm; $U_b = -2$ mV; $I_t = 2$ nA. (c) 5.9 nm × 5.9 nm; $U_b = -2$ mV; $I_t = 10$ nA. (d) 5.9 nm × 5.9 nm; $U_b = -2$ mV; $I_t = 2$ nA. In all cases the electrode potential is $E = 100$ mV_{RHE}, negative potential sweep.45

24. Figure 3.1: [70] a) The Helmholtz model and b) the Stern model of the electric double-layer and electric potential as function of the distance from the metallic electrode. In the picture, Φ_E is the surface potential and Φ_s is the potential at the Stern layer. The Stern model combines the Helmholtz theory (potential linear behavior) with the Gouy-Chapman theory (potential exponential decreasing behavior). In both models, the Helmholtz double-layer can be schematized in terms of capacitance C_H , with the two plates represented respectively by the charges in the metal (the left one) and by the ions in the electrolyte (the right one)..... 51
25. Figure 3.2: [82] STM feedback loop and tunneling effect scheme. When electrons move through the tip and the sample, the feedback loop regularly tracks the resulting tunneling current, to translate this useful information for STM imaging. For rough surfaces, the feedback loop constantly makes adjustments to the tip to maintain a constant current; for flat surfaces, the feedback loop can be switched off to have a constant height image, while varying the tunneling current. 55
26. Figure 3.3: a) Metal-Isolator-Metal schematic representation of the system in equilibrium. b) Metal-Isolator-Metal schematic representation of the system with an arbitrary shape potential barrier; positive potential is applied to the right metal. 56
27. Figure 3.4: [81] Tip geometry scheme: it is assumed locally of spherical shape, in the point of nearest approach to the surface (at a distance d). \vec{r}_o is the center of curvature of the tip. R is the local radius of curvature about the center located at \vec{r}_o 59
28. Figure 3.5: Atomic Force Microscopy basic working principle block. Reproduced from <https://www.bruker.com/en/products-and-solutions/microscopes/materials-afm/faq.html>. 63

29. Figure 3.6: The LJ potential describes both the attraction and repulsion between non-ionic particles. The first part of the equation, $\left(\frac{\sigma}{r}\right)^{12}$ describes the repulsive forces between particles while the latter part of the equation, $\left(\frac{\sigma}{r}\right)^6$, refers to the attractive forces.68
30. Figure 3.7: [111] (a) Scheme of the solid-liquid interface in equilibrium in a tunneling electrochemical reaction. The metal is in equilibrium with the liquid that contains reactant species, the blue ones are oxidized (i.e., once oxidized, they “receive” an electron from the electrode and are therefore reduced) and the red ones are reduced (i.e., once reduced, they “donate” an electron to the electrode and are therefore oxidized), and supporting electrolyte ions. (b) Scheme of the solid-liquid interface when a bias V is applied in a tunneling electrochemical reaction. As a consequence of the applied bias, a non-equilibrium potential drop Φ develops at the solid-liquid interface: this creates a capacitive-like junction between the charges on the metal and the counter charges of the supporting electrolyte ions. Positive current flow (J) occurs when there is a greater transfer of electrons from the working electrode (WE) on the left to the oxidized species in the solution; than J occurs from the reduced species in the solution back to the WE. Under equilibrium conditions, as in (a) case, these two transfer processes are balanced.71
31. Figure 3.8: Schematic representation of a vicinal surface. The figure highlights the miscut angle θ , the step height a , and the terrace width L77
32. Figure 4.1: SPM scheme of the tip-sample interaction [120].79
33. Figure 4.2: Major components of the Keysight Technologies 5500 SPM. [120].80
34. Figure 4.3: (a) STM scanner and (b) AFM scanner [120]. The probe is attached to the piezoelectric scanner (indifferently, (a) or (b)), in which piezoelectric materials are incorporated. Piezoelectric materials have a permanent dipole

moment across unit cell, being able to change their length in an applied field if the dipoles are oriented. If a negative voltage is applied, the piezoelectric material retracts; conversely, if a positive voltage is applied, the scanner will extend. Most SPM use a piezoelectric scan tube technology, which combines (and that's the case) independent piezos to control the three directions x, y and z. By this way, it is possible to have a z motion, if all the three directions are involved, or a x-y scanning (raster) motion. 81

35. Figure 4.4: Keysight's sample plates. The sample plate in the left part is used in the air: the sample can be fixed by the two clamps to get stability and ease of use. The sample plate in the right part of the picture serves the purpose for the electrochemical measurements: the sample is mounted in the Teflon EC-cell and a Viton O-ring is used to seal and to avoid any leakage of liquid. The WE, RE and CE are inserted in the three outlets in the white holder. By using magnetic suspension, loading becomes more convenient and mechanical drift is eliminated [120]. 82

36. Figure 4.5: Tips electrochemical etching procedure scheme. The W wire is moved through a droplet of NaOH solution, suspended in a gold ring at an applied potential of 2 V: at that position, the wire is consumed, and a sharp tip is produced. 84

37. Figure 4.6: Structural Formula of Sulfuric Acid. 86

38. Figure 4.7: [122] a) Sketch of the custom EC cell used for the experiments. b) Image of the STM head immersed in the electrolyte. c) Being more massive, the AFM head requires a wide cell in view of properly purging the tip inside the electrolyte. In particular, our cell can be filled with about 2 ml of electrolyte. Only the working electrode [Cu(111)] is indicated in panels b) and c). 90

39. Figure 4.8: AFM topographic image of HOPG, $2 \times 2 \mu\text{m}^2$. The white line indicates an extrapolated profile (see below) [121]. 93

40. Figure 4.9: Step profile of Figure 4.8 [121].94
41. Figure 5.1: The voltammogram for the reduction of the air-formed oxide film on Cu(111) in 5 mM H₂SO₄ presents distinct features across the two sweeps. The potential was swept initially (a) from ≈ -0.3 to ≈ -0.6 V and then back up to -0.3 V again. The scan rate is 20 mV/s. The potential values are reported with respect to SHE. In the b curve, after repeating the cycle, the oxide has been fully reduced: the reduction peak is now diminished or shifted, as most of the oxide was removed during the first sweep. The process can be performed again until no significant reduction peak is visible anymore, suggesting that the oxide film is entirely reduced. The current response is now stable, confirming the surface has been cleaned of air-formed oxides.....96
42. Figure 5.2: CV of Cu(111) immersed in sulfuric acid electrolyte (pH = 2). A: anodic corrosion; B: copper re-deposition; C: sulfate desorption; D–H: hydrogen evolution; E: sulfate adsorption regime. Scan rate is 20 mV/s. Note, in the upper part of the image, the indication of the area that is analyzed by STM, and of the less stable anodic region that can be explored by AFM.....98
43. Figure 5.3: EC-STM image of the filled states ($I_{\text{tunnel}} = 1.5$ nA; $V_{\text{bias}} = +1.1$ V) of the clean Cu(111) surface acquired at -0.3 V; below the image, profiles related to the I and II lines are shown..... 101
44. Figure 5.4: EC-STM image of the filled states ($I_{\text{tunnel}} = 1.5$ nA; $V_{\text{bias}} = +1.1$ V) of the clean Cu(111) surface acquired at -0.3 V; below the image, profiles related to the I and II lines are shown..... 102
45. Figure 5.5 EC-STM image of the filled states ($I_{\text{tunnel}} = 1.53$ nA; $V_{\text{bias}} = +1.1$ V) of the clean Cu(111) surface acquired at -0.3 V; below the image, profiles related to the I, II and III lines are shown..... 103
46. Figure 5.6: a) The cubic cell of the FCC Cu crystal, with a lattice constant parameter of $a_{\text{Cu}} = 3.61$ Å; the (111) plane is highlighted in blue. b) The two-

- dimensional Cu(111) lattice and its unit cell with a side length of $a_{\text{Cu}} = 2.55 \text{ \AA}$.
 104
47. Figure 5.7: Formation of the ordered adsorption phase acquired at +0.1 V ($I_{\text{tunnel}} = 1.3 \text{ nA}$; $V_{\text{bias}} = +0.7 \text{ V}$). In the picture, it is possible to distinguish the different phases of the adsorption mechanism: the disordered sulfates adsorption (i.e., the fuzzy areas) and the regions where the ordered Moiré-superstructure coexists with the ordered sulfate structure (like those regions marked by the white arrows). 105
48. Figure 5.8: Formation of the Moiré-superstructure acquired at +0.1 V ($I_{\text{tunnel}} = 1.5 \text{ nA}$; $V_{\text{bias}} = +0.7 \text{ V}$). The image displays distinct phases of the adsorption anions, highlighting the nebulous regions dominated by disordered sulfate adsorption alongside areas where the ordered Moiré-superstructure and a well-defined sulfate anion arrangement are visible. 106
49. Figure 5.9: Upper part of the image: ordered adsorption phase acquired at +0.1 V ($I_{\text{tunnel}} = 1.5 \text{ nA}$; $V_{\text{bias}} = +0.7 \text{ V}$); in-situ and in real time starting of the cyclic voltammetry towards the sulfate ions desorption regime and consequent disappearance of the Moiré-superstructure at the white dashed line. The scanned area is the same as in Figure 5.8. The black arrow indicates the image's acquisition direction..... 107
50. Figure 5.10: Alternation of adsorption and desorption cycles, starting from the upper part of the image in which a bare Cu(111) surface is clearly visible, with consequent appearance and disappearance of the Moiré pattern. The black arrow indicates the image's acquisition direction..... 108
51. Figure 5.11: [127] a) At a potential of $E = +0.1 \text{ V}$ ($I_t = 1.5 \text{ nA}$, $U_b = +0.7 \text{ V}$), the sulfate-covered Cu(111) surface exhibits an elongated hexagonal mesh characteristic of the Moiré-superstructure. b) A highly resolved image reveals the detailed arrangement of the sulfate anions, including both the $(\sqrt{3} \times \sqrt{7})R30^\circ$ structure and the superimposed Moiré pattern, $E = +0.1 \text{ V}$, I_t

= 1.5 nA, $U_b = +0.7$ V. c) Within the Moiré-superstructure, a "Moiré-unit" (represented by an inner hexagon of brighter intensity) is nested inside the "Moiré-mesh" (the outer hexagon of darker spots), with axes labeled as a, b, and c, providing a precise depiction of the periodic modulation at the surface.109

52. Figure 5.12: [48] [57] [62] a) EC-STM image of the Cu(111) electrode covered with the sulfate-induced Moiré-superstructure, which highlights the three rotational domains, labeled A, B, and C. Each domain is rotated by 120° relative to the others. The image covers a scan area of $101 \text{ nm} \times 101 \text{ nm}$, $U_b = 169 \text{ mV}$, $I_t = 1 \text{ nA}$. The fuzzy regions in the image indicate areas covered by sulfate SO_4^{2-} anions in a disordered phase, meaning the anions are not yet arranged in the ordered Moiré pattern. A white arrow points to a copper island that is covered by the Moiré pattern. In panels b) and c), quasi-STs imaging is used to provide direct evidence of sulfate-induced expansion of the first copper layer. Panel b) shows the $(\sqrt{3} \times \sqrt{7})R30^\circ SO_4^{2-}$ structure at high resolution over a $5.9 \text{ nm} \times 5.9 \text{ nm}$ area, $I_t = 10 \text{ nA}$, $U_b = -2 \text{ mV}$. Panel c) shows the underlying copper layer (see the smaller rhombic unit cell), again over a $5.9 \text{ nm} \times 5.9 \text{ nm}$ area, but with a lower tunneling current of $I_t = 2 \text{ nA}$ and the same bias voltage. The superimposed $(\sqrt{3} \times \sqrt{7})R30^\circ$ sulfate unit cell from panel b) emphasizes the expansion of the first copper layer induced by sulfate adsorption. This expansion is a key factor in the development of the Moiré pattern [128].111

53. Figure 5.13: [60] Sequence of EC-STM images showing the gradual development of the sulfate-induced Moiré-superstructure on a Cu(111) electrode. The images capture key stages of this process. Panels a) to c) depict the successive growth of the Moiré-superstructure across a $101 \text{ nm} \times 101 \text{ nm}$ area under the conditions of $U_b = 169 \text{ mV}$ and $I_t = 1 \text{ nA}$. Figure 5.12a is part of this sequence, situated between panels b) and c). Panel d) emphasizes the quantized nature of the sulfate-induced copper island formation.....112

54. Figure 5.14: Transition from a mobile sulfate phase at negative potentials to a more structured, Moiré-superstructure phase at positive potentials, where sulfate anions enforce surface reconstruction on the copper substrate. a): at negative potentials, the Cu(111) surface remains unreconstructed, with copper (red) atoms in their original positions, and mobile sulfate anions (grey molecules) are loosely adsorbed on the Cu(111) surface, not yet in a highly ordered or structured phase. b) at positive potentials, Cu(111) surface undergoes reconstruction, resulting in a modified arrangement of copper atoms (represented as orange atoms); Cu islands form on the surface. Some regions, where the Cu(111) surface is not fully reconstructed, still show remnants of mobile sulfate anions, reflecting minor areas of the unreconstructed (111) surface. 113
55. Figure 5.15: a) The FCC structure of the copper lattice, highlighting the orientation of the (111) and (221) planes. The inclination direction $[11\bar{2}]$ and the step edges direction $[1\bar{1}0]$ are depicted, with the vicinal angle of 16° indicated. b) An ideal cross-section diagram for the flat Cu(111) surface for comparison; the Cu(21 21 16) surface, characterized by a vicinal angle of approximately 7° and terrace widths of 1.7 nm; the Cu(221) surface, featuring a vicinal angle of about 16° , with terrace widths of 0.73 nm; the orientation and height of the steps are clearly illustrated. 115
56. Figure 5.16: Effect of potential changes on the Cu(21 21 16) surface as observed through STM imaging. The image shows the transition [at the potential change from -0.3 V to +0.1 V] from a sulfate-free Cu(21 21 16) surface to one covered by the sulfate-induced Moiré-superstructure, highlighting the formation of islands of varying sizes corresponding to multiples of Moiré units, indicated by the white circles. Tunneling parameters are: $E = -0.3$ V ($I_t = 1.3$ nA; $U_b = +1$ V) for the bare Cu(21 21 16) surface and $E = +0.1$ V ($I_t = 1.5$ nA; $U_b = +0.7$ V) for the Moiré covered surface. Circles denoted with dotted lines enclose islands containing one Moiré unit, $r_1^* = 4.4$ nm; circles denoted with dashed lines - - - - enclose islands containing two

Moiré units, $r_2^* = 6.2$ nm; circles denoted with solid lines — enclose islands containing three Moiré units, $r_3^* = 7.5$ nm..... 117

57. Figure 5.17: a) STM observation of the Cu(221) surface after sulfate adsorption at $E = -0.3$ V, $I_t = 1$ nA, $U_b = +0.7$ V; b) A zoomed-in view of the white rectangle in the first image shows three distinct widths between the bright stripes. These widths are: width (1) ≈ 1.5 nm, width (2) ≈ 2.6 nm, width (3) ≈ 4 nm. The terraces' widths after sulfate adsorption are significantly larger than the original terrace width of the bare Cu(221) surface, which is only 0.73 nm..... 119

58. Figure 5.18: a) STM image of the growth of a Moiré-covered island [60], highlighted by the white arrow (image dimensions: 101 nm x 101 nm, bias voltage $U_b = 169$ mV, tunneling current $I_t = 1$ nA). b) and c) present zoomed-in views of the step edges contained within the white rectangles from panel a), illustrating the different orientations (A or B, C) of the Moiré-meshes..... 121

59. Figure 5.19: Scheme of the regular hexagonal Moiré-superstructure area, divided in 36 triangles X, and of the Moiré-unit area. 123

60. Figure 5.20: Scheme of the regular hexagonal Moiré-superstructure compared to the real elongated Moiré-superstructure..... 126

61. Figure 5.21: Scheme of the real elongated Moiré-superstructure area and of the real elongated Moiré-unit area inside. 126

62. Figure 5.22: [122] EC-AFM of the clean Cu(111) surface immersed in sulfuric acid at -0.3 V. Panel I shows flat lamellar terraces, typical of the Cu(111) surface, which are partially affected by globular structures. A dark star marks a prominent globular structure used as a reference feature for subsequent acquisitions, ensuring consistency between successive images. Profiles a and b are plotted on the right side of the image. Panels I.II - I.IV: blow-ups of specific regions of the surface, highlighted by the dashed squares in panel I. 132

63. Figure 5.23: [122] EC-AFM images tracking the surface morphology of Cu(111) during the copper anodic corrosion and re-deposition processes [$(2 \times 2) \mu\text{m}^2$]. Panel a): the white solid line marks the moment when the EC potential reaches 0.2 V, i.e., the onset of copper corrosion, and is held constant during the image acquisition (see scan direction). Profiles acquired along the white dashed lines at the bottom of the panel indicate the formation of depressions, suggesting intense surface disintegration during corrosion. Panel b): copper re-deposition process. The EC potential is linearly reduced from 0.2 V to -0.3 V and then held fixed to facilitate the copper re-deposition; the white solid line indicates when the re-deposition peak is reached. Panel c): full image post re-deposition, captured at -0.3 V. The white dashed lines mark the profiles reported at the bottom of the panels, which illustrate the new surface height and the reduced size of terraces. The white squares in panels b) and c) are highlighted to compare specific regions of the scanned area with Figure 5.24, emphasizing consistent reference points for surface analysis. 133
64. Figure 5.24: [122] [$(4 \times 4) \mu\text{m}^2$] EC-AFM image showing the Cu(111) surface after the copper re-deposition process at ≈ 15 V. The white dotted lines outline the specific area where the images from Figure 5.23 were taken. In addition, the large, dashed square contains three rectangular regions, which are used to correlate and compare with the same regions highlighted in Figure 5.23. The profiles on the right side were acquired along the white full lines. 134
65. Figure 5.25: [122] EC-STM image [$(300 \times 300) \text{nm}^2$] depicting the filled states of the clean Cu(111) surface, obtained with $I_t = 1$ nA, $V_b = +1.1$ V and acquired at -0.3 V (D point in the CV in Figure 5.2), following the re-deposition process. The profile shown at the bottom was measured along the solid white line. 135

Abstract

This thesis investigates the adsorption-induced surface reconstruction on vicinal Cu(111) surfaces interacting with sulfate anions in a dilute sulfuric acid solution, with the aim of investigating whether principles derived from vacuum studies are applicable to electrochemical systems. Specifically, the objective is to understand how solid-liquid interfacial interactions can modify the surface structure at the atomic level, with significant implications for nano-electrochemistry and corrosion analysis. Nano-electrochemistry, a field that has gained prominence due to the continuous miniaturization of devices and materials, forms the foundation of this work, exploring how electrochemical processes at the nanoscale affect low-dimensional materials. In this context, vicinal surfaces, that have a crucial role in surface confinement, profoundly impact on electrochemical processes at the atomic scale: the work aims to elucidate how surface step edges and atomic-scale defects influence electrochemical behavior, with direct implications for surface reactivity.

The experimental approach employed advanced surface-sensitive techniques (Electrochemical Scanning Probe Microscopy – EC-SPM), with a particular emphasis on Electrochemical Scanning Tunneling Microscopy (EC-STM). This technique allows for in-situ analysis of the structural changes that occur on copper surfaces when exposed to electrolytic environments. The Cu(111) surface was selected for its significance in nanoelectronics and its relatively wide electrochemical window, which permits investigation under both anodic and cathodic conditions. Cu(111) vicinal surfaces, characterized by regularly spaced step edges and kink sites, offer unique electrochemical properties compared to flat, atomically smooth surfaces like basal Cu(111). In fact, the lateral confinement induced by these surface features plays a critical role in altering the local electric fields and concentration gradients at the solid-liquid interface. These structural characteristics significantly enhance catalytic reactivity, particularly at defect sites, where the altered atomic coordination and electronic environment

lead to increased adsorption and reaction kinetics. The research focuses on Cu(221) and Cu(21 21 16) vicinal surfaces, both of which exhibit distinct step geometries, allowing for the systematic study of how surface confinement affects sulfate adsorption and surface reconstruction.

A key component of this research is the formation of the sulfate-induced Moiré-superstructure on Cu(111): EC-STM imaging reveals the long-range periodic pattern formed by sulfate adsorption at slightly anodic potentials, which is distinct from atomic-level structures and extends across the terraces of the copper surface. The interaction of sulfate anions with the copper surface leads to surface reconstruction, where the atomic density of the topmost copper layer decreases, as a consequence of the adsorbed sulfate-induced expansion of the first Cu layer on Cu(111). This process causes a mismatch between the first and second copper layers, leading to the visible formation of the Moiré pattern.

The formation of the sulfate-induced Moiré-superstructure on Cu(111), a hallmark of surface reconstruction, is also influenced by the step edges on vicinal surfaces. The lateral confinement provided by the step sites creates regions of enhanced surface reconstruction, resulting in more complex structures compared to the flat surface. The study reveals that these vicinal surfaces undergo more pronounced and sustained surface transformations under electrochemical conditions than their flat counterpart, largely due to the confinement effects that promote localized adsorption and reactivity. On the bare Cu(221) surface, the high density of steps and the narrow (111) terraces restrict but do not prevent the development of the Moiré-superstructure. This limitation results in terrace widening and a shift toward a configuration that accommodates only a single row of Moiré units. In contrast, on the wider terraces of the Cu(21 21 16) surface, the Moiré-superstructure evolves similarly to that on the flat Cu(111) surface, leading to the formation of additional islands. The findings suggest that both terrace widening on Cu(221) and the controlled growth of islands on Cu(21 21 16) are driven by the ordered adsorption of sulfate anions. These electrochemical processes, however, are governed by a step-induced confinement effect that is dependent on terrace width and step separation. The innovative aspect of this research lies in its

approach to address a key gap in the literature: while vicinal surfaces have been extensively studied under vacuum conditions, little attention has been paid to their behavior in electrochemical environments. The results of this research demonstrate that, under real electrochemical conditions, electrochemical forces, particularly those related to sulfate adsorption, prevail over the effects of physical confinement. This is evident from the formation of islands on vicinal surfaces such as Cu(21 21 16), which resemble those formed on flat Cu(111) surfaces. Despite the intrinsic physical constraints imposed by the steps, electrochemical processes facilitate a more extensive surface restructuring, effectively overriding the confinement effects known from vacuum studies.

In conclusion, this work enhances our understanding of the atomic-scale interactions at the solid-liquid interface and their implications for nano-electrochemical processes. The findings reopen the investigation into surface reactivity at step edges, not only on vicinal surfaces but also on low-index planes like Cu(111), suggesting a reinterpretation of their electrochemical behavior. By showing that electrochemical forces can be successful despite the physical confinement, this thesis contributes new insights into how surface morphology and electrochemical behavior are interlinked. By investigating the structural transformations of copper surfaces in sulfate-containing environments, the thesis provides valuable insights into surface reactivity, corrosion processes, and the design of electrochemical systems at the nanoscale. These findings are not only relevant to the field of corrosion science but also to the broader realm of nanotechnology, where control over surface structure and electrochemical behavior is critical for the development of next-generation materials and devices.

Sinopsi

Quest'elaborato esplora la ricostruzione superficiale indotta dall'adsorbimento su superfici vicinali di Cu(111) interagenti con anioni solfato in una soluzione diluita di acido solforico, al fine di indagare se i principi derivati dagli studi in vuoto siano applicabili ai sistemi elettrochimici. In particolare, l'obiettivo è comprendere come le interazioni all'interfaccia solido-liquido possano modificare la struttura superficiale a livello atomico, con rilevanti implicazioni per la nano-elettrochimica e l'analisi della corrosione. La nano-elettrochimica, un campo in costante evoluzione grazie alla miniaturizzazione di dispositivi e materiali, rappresenta il cuore di questa ricerca. Viene esaminato come i processi elettrochimici su scala nanometrica influenzino materiali a bassa dimensionalità, offrendo una prospettiva unica sulle dinamiche che si sviluppano a livello atomico. In questo contesto, le superfici vicinali, che giocano un ruolo chiave nel confinamento superficiale, diventano essenziali per comprendere i processi elettrochimici su scala atomica: l'obiettivo è svelare come i bordi dei gradini e i difetti atomici condizionino la reattività elettrochimica, con impatti diretti sulla reattività superficiale.

L'approccio sperimentale si avvale di tecniche d'avanguardia sensibili alla superficie (Microscopia a Sonda Elettrochimica – EC-SPM), con un particolare focus sulla Microscopia a Scansione di Tunneling Elettrochimica (EC-STM). Questa tecnologia consente di monitorare *in-situ* le trasformazioni strutturali delle superfici di rame esposte ad ambienti elettrolitici: la superficie di Cu(111) è stata selezionata per la sua rilevanza in nanoelettronica e la sua ampia finestra elettrochimica, che permette di esplorare condizioni sia anodiche che catodiche. Le superfici vicinali di Cu(111), con i loro bordi di gradino regolarmente disposti e i siti di kink, esibiscono proprietà elettrochimiche uniche rispetto alle superfici piatte e atomisticamente lisce, come Cu(111) basale. Il confinamento laterale, indotto da queste caratteristiche, gioca un ruolo cruciale nel modulare i campi elettrici locali e i gradienti di concentrazione all'interfaccia solido-liquido. Queste

peculiarità strutturali amplificano significativamente la reattività catalitica, specialmente nei siti di difetti, dove la coordinazione atomica alterata e l'ambiente elettronico potenziano l'adsorbimento e la cinetica di reazione. La ricerca si focalizza sulle superfici vicinali di Cu(221) e Cu(21 21 16), caratterizzate da geometrie di gradino uniche, permettendo uno studio sistematico sull'influenza del confinamento superficiale sull'adsorbimento di solfato e sulla ricostruzione atomica.

Un aspetto centrale di questa ricerca è la formazione della superstruttura Moiré indotta da solfato su Cu(111): le immagini EC-STM rivelano un pattern periodico a lungo raggio, prodotto dall'adsorbimento di solfato a potenziali leggermente anodici, che si distingue dalle strutture atomiche locali ed è distribuito sulle terrazze della superficie di rame. L'interazione degli anioni solfato con la superficie del rame causa una ricostruzione che riduce la densità atomica dello strato più esterno di rame, a seguito di un'espansione del primo strato superficiale di rame indotta dall'adsorbimento di solfato; quest'interazione provoca uno sfasamento tra il primo e il secondo piano di Cu(111), portando alla formazione del pattern Moiré.

La formazione della superstruttura Moiré indotta da solfato, emblema della ricostruzione superficiale, è ulteriormente influenzata dai bordi dei gradini nelle superfici vicinali. Il confinamento laterale prodotto da questi siti favorisce aree di ricostruzione amplificata, generando strutture più complesse rispetto alla superficie piana. Lo studio evidenzia che queste superfici vicinali subiscono trasformazioni superficiali più accentuate e durature in condizioni elettrochimiche rispetto alla loro controparte piatta di Cu(111), principalmente a causa degli effetti di confinamento che promuovono l'adsorbimento localizzato e una maggiore reattività. Sulla superficie di Cu(221), già a dei potenziali per i quali la si aspetterebbe priva di adsorbato, l'alta densità di gradini e le strette terrazze (111) rilevano e limitano lo sviluppo della superstruttura Moiré, portando a un allargamento delle terrazze che ospita solo una singola fila di unità Moiré. Al contrario, sulle terrazze più ampie di Cu(21 21 16), la superstruttura Moiré evolve in maniera simile a quella su Cu(111), con l'ulteriore formazione di isole. Questi

risultati suggeriscono che sia l'espansione delle terrazze su Cu(221) che la crescita controllata delle isole su Cu(21 21 16) siano determinati dall'adsorbimento ordinato degli anioni solfato. Tuttavia, tali processi elettrochimici sono governati da un effetto di confinamento indotto dai gradini, che dipende dalla larghezza delle terrazze e dalla separazione tra i gradini. L'aspetto innovativo di questa ricerca risiede nel suo approccio volto a colmare una lacuna chiave nella letteratura: mentre le superfici vicinali sono state ampiamente studiate in condizioni di vuoto, è stata prestata poca attenzione al loro comportamento in ambienti elettrochimici. I risultati di questa ricerca dimostrano che, in condizioni elettrochimiche reali, le forze elettrochimiche, in particolare quelle legate all'adsorbimento del solfato, prevalgono sugli effetti del confinamento fisico. Questo è evidente dalla formazione di isole su superfici vicinali come Cu(21 21 16), un comportamento che richiama quello osservato su superfici planari come Cu(111). Nonostante i vincoli fisici intrinseci imposti dai gradini, i processi elettrochimici facilitano una ristrutturazione più estesa della superficie, superando gli effetti di confinamento noti negli studi condotti in vuoto.

In conclusione, questo lavoro rappresenta un significativo passo avanti nella comprensione delle interazioni atomiche all'interfaccia solido-liquido e delle loro implicazioni nei processi nano-elettrochimici. La ricerca riapre l'indagine sulla reattività superficiale ai bordi dei gradini, non solo sulle superfici vicinali ma anche su piani a basso indice come Cu(111), suggerendo una reinterpretazione del loro comportamento elettrochimico. Dimostrando che le forze elettrochimiche possono essere efficaci nonostante il confinamento fisico, questa tesi fornisce nuove intuizioni su come la morfologia superficiale e il comportamento elettrochimico siano interconnessi. Esaminando le trasformazioni strutturali delle superfici di rame in ambienti contenenti solfato, la tesi fornisce contributi fondamentali alla comprensione della reattività superficiale, dei processi di corrosione e della progettazione di sistemi elettrochimici su scala nanometrica. Queste scoperte sono di estrema rilevanza non solo per il campo della scienza della corrosione, ma anche per il più ampio ambito della nanotecnologia, dove il

Sinopsi

controllo della struttura superficiale e del comportamento elettrochimico è cruciale per lo sviluppo di materiali e dispositivi di nuova generazione.

1.

Introduction

1.1 The Emphasis on the Solid-Liquid Interface

Solid-liquid interfaces are in the heart of a heterogeneity of natural, chemical and biological phenomena, widely found in our daily life [1]. Its investigation requires experimental techniques with high surface sensitivity, like Scanning Probe Microscopy (SPM) [2]. For example, solid-liquid interfaces are crucial in many de-watering mineral processing operations, such as the recovery and separation of minerals from waste host rocks, as well as corrosion phenomena. Nowadays, investigation of properties and processes at the solid-liquid interface is even an essential issue for a lot of technological applications, namely the surface functionalization, electrocatalysis and electrodeposition techniques [3]. Various nanoscale materials, such as nanoparticles or nanowires, synthesized by electrodeposition techniques are widely used in the fields of energy, environmental and medical technologies as well as to fabricate sensors and electronic devices [4] [5]. And, again, the overuse of fossil fuels has led to a worsening energy crisis. The development of renewable energy conversion devices to address these global issues has thus become a major focus in scientific research: on this basis, electrocatalytic energy conversion is emerging as a strong contender among various clean energy technologies because it can transform

molecules into higher-value products in the atmosphere [6]. By way of illustration, it is known that the hydrogen evolution reaction (HER) is essential for overall water splitting in electrocatalysis [7] [8] and the oxygen evolution reaction (OER) and oxygen reduction reaction (ORR) are critical half-reactions for rechargeable metal-air batteries [9] [10]. Therefore, designing electrocatalysts with optimized physical and chemical properties to enhance adsorption and desorption processes (that is, electrochemical reactions, which typically take place on the interface of catalysts) is crucial for achieving superior performance under specific catalytic conditions [11].

Electrochemical Scanning Tunneling Microscopy (EC-STM) research in corrosion has largely concentrated on elucidating the mechanisms of corrosion initiation and inhibition processes, *i.e.*, the inhibitors effect, the pitting initiation stage, surface dissolution and passive film formation. Corrosion is defined as a surface damage process in a liquid environment. EC-STM has been used to investigate various materials, such as copper (Cu), nickel (Ni) and iron (Fe), across numerous corrosion environments [12]. Particularly for metals, corrosion is a chemical/electrochemical process involving the oxidation of the metal, which transfers electrons to the electrolytic environment and undergoes a change in valence from zero to a positive value: as a consequence of this initial process, secondary corrosion products are formed resulting in the material (surface) dissolution. Metal corrosion processes can be classified into two main forms: general corrosion and localized corrosion. General corrosion involves the entire surface area of the material, while localized corrosion occurs at specific sites on the material surface. A surface passive film can prevent further oxidation of the metallic substrate, passivating the surface. However, under certain conditions, the passive state of a metal can become unstable leading to localized corrosion, through the (local) dissolution of the passive layer: this process is known as pitting corrosion [13]. Active pits often develop at defective sites on the passive film surface, sharp edges, or areas where the oxide film is thinner. The pitting process is inherently anodic (metal dissolution) compared to the passivated cathodic region surrounding it, allowing a continuous flow of electrons.

In 1990s, the EC-STM was first proposed to observe single molecule charge transport. The initial EC-STM experiments were conducted on iron porphyrin molecules adsorbed on highly ordered pyrolytic graphite (HOPG) surfaces: since these pioneering experiments, EC-STM has evolved into a powerful tool for studying, in an electrochemical environment, interfacial electron transfer and molecular conductance of electroactive species at the single molecule level [14]. In every respect, following the general interest in the device's miniaturization processes, nano-electrochemistry has recently emerged as a new essential research area focusing on *atomic-scale comprehension of the interfacial structure* and on its effect on the fabrication of low-dimensional materials.

1.2 The Emergence of Nano-Electrochemistry in Miniaturization and Low-Dimensional Materials

Recently, the unceasing drive for miniaturization in numerous technological fields has highlighted the vital significance of nano-electrochemistry. This emergent field focuses on understanding and manipulating electrochemical processes at the nanoscale, which is pivotal for advancing the fabrication and application of low-dimensional materials [15]. The trend towards miniaturization is a hallmark of modern technological advancement, driven by the demand for more efficient, high-performance devices. This trend extends across various domains, including semiconductor technology, energy storage systems, and biomedical devices. As device dimensions approach the nanometer scale, classical electrochemical models become insufficient to describe and predict the behavior of these systems [16] [17]. Nano-electrochemistry addresses this gap by providing a framework to understand phenomena at the atomic scale.

Nano-electrochemistry involves studying electrochemical processes where the size of the system approaches the scale of individual atoms or molecules. At this scale, the electrochemical interface exhibits unique properties due to increased

surface-to-volume ratios and quantum effects [18]. For example, the modification of electronic structure and reactivity at nanoscale interfaces can significantly alter the electrochemical behavior of materials. This necessitates a detailed understanding of atomic-scale interactions to control and optimize electrochemical processes in nanoscale devices. A core aspect of nano-electrochemistry is the examination of interfacial structures at the atomic level. This includes the study of how atomic-scale defects, surface reconstructions, and interactions between nanoscale entities influence electrochemical reactions [19]. Techniques such as scanning tunneling microscopy and Atomic Force Microscopy (AFM) are employed to probe these interfaces with high spatial resolution. Understanding these interactions is crucial for tailoring the electrochemical properties of materials and for developing novel nanoscale devices with enhanced performance characteristics [20]. Low-dimensional materials, including two-dimensional (2D) materials like graphene and transition metal dichalcogenides (TMDs), as well as one-dimensional (1D) materials like carbon nanotubes, exhibit extraordinary electronic, optical, and mechanical properties that are often distinct from their bulk counterparts [21]. The synthesis and application of these materials require precise control over their atomic-scale properties. Nano-electrochemistry provides insights into how electrochemical processes can be used to manipulate these properties, thereby influencing the performance of low-dimensional materials in practical applications. For instance, understanding the interfacial interactions can lead to improved methods for doping, functionalization, and integration of these materials into devices. The insights gained from nano-electrochemistry are instrumental in advancing technologies such as nanoscale sensors, energy storage devices, and catalysis. For example, in energy storage, the development of high-capacity, high-efficiency batteries and supercapacitors relies on optimizing the electrochemical behavior of materials at the nanoscale. Similarly, in catalysis, understanding the atomic-scale interactions at catalytic interfaces can lead to the development of more efficient catalytic processes. Future research in nano-electrochemistry is likely to focus on integrating these findings

into practical applications and exploring new materials with tailored electrochemical properties [22] [23] [24] [25].

In summary, nano-electrochemistry represents a critical area of research that bridges the gap between fundamental science and applied technology. Its focus on atomic-scale processes provides essential insights for the continued advancement of miniaturized devices and low-dimensional materials. As the field evolves, it will play a pivotal role in addressing the challenges associated with the next generation of high-performance, nanoscale technologies.

The use of single-crystal electrodes in electrochemical studies began with coinage metals such as gold, silver, and copper. However, it wasn't until the 1980s, following the publication of the flame-annealing technique for platinum, that these preparation methods became widely accessible to laboratories around the world [26]. Initially, much of the research focused on basal plane electrodes, which are characterized by broad, flat terraces containing a single type of atomic site and were considered ideal for obtaining representative electrochemical responses under controlled conditions. The challenge of preparing bi-dimensionally ordered surfaces sparked considerable debate, particularly regarding the nature of the species responsible for charge transfer. Imaging techniques played a crucial role in determining the conditions under which experimental electrode surfaces in contact with electrolytes matched the expected outcomes based on their Miller indices. Today, these techniques have become refined, allowing for the achievement of these goals in most cases, although certain questions remain still open.

The significance of studying well-defined basal plane electrodes, especially (111) oriented surface, lies in their ability to characterize the interaction between solution species and a uniform atomic site. This research yields fundamental data that serve as benchmarks for theoretical modeling. Despite advancements in computational power, there is still no definitive method for predicting the behavior of electrochemical systems, making experimental comparison essential. Furthermore, successful modeling of electrode activity is likely to generate new questions regarding reactivity, prompting further specific experiments with

single-crystal electrode surfaces, fostering a continuous feedback loop between theory and experiment. Applied research has also benefited from single-crystal studies, particularly in identifying the most active surface configurations for specific reactions. However, basal plane electrodes have a conceptual limitation: practical electrodes rarely feature bidimensional domains larger than a modest number of atoms. To better simulate the behavior of real-world nanoparticle electrodes, researchers have turned to well-defined *stepped surfaces* as an experimental strategy. These studies, which fall under the umbrella of fundamental electrocatalysis, address two key points:

- Firstly, it is widely believed that defect sites are often the most reactive for certain reactions. By preparing surfaces with terraces of specific symmetry separated by steps containing a single type of atomic site, researchers can quantify the difference in reactivity between these sites. Since this arrangement can be constructed at the atomic level, it allows for the systematic study of reactivity as a function of defect density, a parameter that can be precisely controlled.
- Secondly, for many stepped surfaces, the overall reactivity of the electrode tends to follow simple trends that can be understood as a linear combination of contributions from both terraces and steps. This relationship can be extrapolated in two directions: towards surfaces with a high concentration of closely spaced steps, or towards defect-free surfaces. In the first case, comparing the experimental response of a highly stepped surface with theoretical models can reveal the impact of additional factors that become significant at short distances. In the second case, extrapolating to an ideal defect-free surface provides an estimate of the reactivity of perfectly flat, two-dimensional surfaces, which can then be compared with basal plane electrodes to emphasize long-range effects.

1.2.1 The Role of Vicinal Surfaces: Bridging the Gap Between UHV and Electrochemical Systems

In the context of electrochemical studies involving nano-structured surfaces, the vicinal surfaces - those with periodic step and kink sites - play a critical role in influencing surface nano-confinement effects and nano-electrochemical behavior [27]. The majority of early investigations into vicinal surfaces were conducted in ultra-high vacuum (UHV) environments, using techniques such as STM to achieve atomic-scale imaging of surface structure. These studies have provided a wealth of knowledge about the atomic arrangement, electronic properties and surface dynamics of vicinal surfaces. However, the transition from UHV studies to nano-electrochemical systems, particularly in the field of EC-STM, marks a significant step in extending the applicability of these surfaces beyond idealized conditions, into real-world catalytic and electrochemical processes.

Vicinal surfaces have been widely studied in UHV conditions because such environments allow researchers to control surface cleanliness, eliminate contaminating species, and precisely control temperature and pressure. These conditions are ideal for studying fundamental surface phenomena without the interference of external factors [28]. A typical STM study in UHV focused on the Au(111) vicinal surfaces. In this study, STM images revealed that these surfaces are ideal candidates for use as templates in the organized growth of clusters: the behavior of the Au(111) surface reconstruction near steps is highly dependent on the microstructure of the steps, which is a crucial factor in understanding the various periodic morphologies that form on Au(111) vicinal surfaces [29]. Yet, different researches on Cu(111) vicinal surfaces were widely explored in UHV environment, such as the study on the surface structure of Cu(111) vicinal surfaces with (111)- and (100)-oriented steps, using STM and Scanning Electron Microscopy (SEM). In this study, the vicinal surface with (100)-steps exhibited the expected regular step arrays following

UHV preparation. However, the surface with (111)-steps developed macroscopic roughness: the authors proposed that these observed structures represent local energy minima, which are more easily reached under the kinetic constraints of a large Schwoebel–Ehrlich barrier, rather than the true equilibrium surface structure [30].

While research on vicinal surfaces in vacuum settings has yielded significant findings, there is a pressing need to extend these investigations to the field of nano-electrochemistry. UHV environments are highly idealized, and they do not accurately reflect the complex conditions found in real-world catalytic and electrochemical systems, such as electrolyte interactions, applied potentials, and surface restructuring under reaction conditions. The transition from UHV to electrochemical environments is critical for several reasons [27]:

- 1) **Electrolyte Interactions:** In electrochemical systems, vicinal surfaces are exposed to electrolytes, which introduce additional layers of complexity. Adsorption of electrolyte ions, surface charge, and the presence of electric double layers significantly influence the behavior of surface atoms and reaction intermediates. These phenomena cannot be captured in UHV studies but are crucial for understanding real catalytic and electrochemical processes.
- 2) **Potential-Driven Surface Restructuring:** In UHV studies, surfaces are typically imaged under equilibrium conditions, without the influence of external electric fields. However, in electrochemical environments, the application of potential can induce significant restructuring of vicinal surfaces. This dynamic restructuring alters the availability and reactivity of step and kink sites, which is important for reactions such as CO₂ reduction and oxygen evolution.
- 3) **Reaction Conditions:** UHV studies cannot simulate the actual conditions under which electrochemical reactions take place. In real systems, reaction

conditions such as temperature, pressure, and pH, as well as the presence of reactants like CO₂ or O₂, can have a profound effect on surface behavior. Expanding vicinal surface studies into nano-electrochemistry allows researchers to investigate how these surfaces behave under working conditions, providing more relevant insights for applications like fuel cells, batteries, and CO₂ reduction.

To bridge the gap between UHV studies and real-world applications, EC-STM has emerged as a powerful tool. EC-STM offers a powerful platform for studying electrochemical reactions at the nanoscale with superior spatial resolution and chemical sensitivity compared to traditional STM techniques. EC-STM not only captures atomic-scale changes in surface morphology under electrochemical conditions but also provides a window into the reaction mechanisms that occur at step and kink sites. The insights gained from EC-STM studies are indispensable for the rational design of nano-structured electrodes. For example, controlling the density of steps and kinks on vicinal surfaces can be used to enhance selectivity towards specific reaction products. Furthermore, by understanding how surfaces restructure in response to applied potentials and reactants, researchers can develop strategies to stabilize the most catalytically active surface features. One of the EC-STM studies involved imaging vicinal Cu surfaces during the electrochemical reduction of CO₂ [31]. Under applied potentials, the study revealed that Cu step edges were highly dynamic, undergoing continuous restructuring as CO₂ was reduced to hydrocarbons like ethylene. This dynamic behavior was not observed in UHV studies, highlighting the importance of studying surfaces under actual reaction conditions. The ability of EC-STM to capture real-time surface changes provided crucial insights into how vicinal Cu surfaces could be engineered to optimize product selectivity.

Thus, the study of vicinal surfaces in UHV environment using STM has provided a solid foundation for understanding the atomic-scale properties of these surfaces. However, expanding this research into electrochemical

environments using EC-STM is essential for gaining insights into how vicinal surfaces behave under real-world reaction conditions. Vicinal surfaces, characterized by their regular step edges and kink sites, exhibit distinct electrochemical properties compared to their atomically flat counterparts. The step edges on such surfaces provide unique sites for enhanced catalytic reactivity due to their altered electronic environment and geometric configuration, which can influence the adsorption and reaction kinetics of electrochemical processes [26]. For instance, in acidic solutions, the presence of step and kink sites on Cu(111) vicinal surfaces significantly affects the electrochemical behavior, such as the onset potential and the overall rate of reactions like the oxygen evolution reaction (OER). The lateral confinement imposed by these vicinal structures can lead to changes in the local electric field and concentration gradients, thereby modifying the kinetics of electrochemical processes. Moreover, the stability of these vicinal surfaces under operational conditions is a critical concern, as electrochemical processes are known to induce large-scale surface restructuring and faceting. By bridging the gap between UHV and electrochemical studies, researchers can unlock new possibilities for optimizing catalysts and electrode materials, paving the way for more efficient and sustainable electrochemical processes.

In exploring the diverse range of vicinal surfaces, we have strategically chosen to focus on **Cu(111) vicinal surfaces**: this decision is driven by the unique properties and research opportunities offered by the flat surface. Cu(111) vicinal surfaces, characterized by their well-defined step structures and atomically smooth terraces, provide an exceptional platform for investigating surface phenomena and electrochemical behaviors. Their intricate atomic arrangements and the resulting interactions with adsorbates, such as sulfate ions, present a rich field for in-depth study. It is therefore essential to investigate the interplay between these structural features and the electrochemical performance of Cu(111) and its vicinal surfaces, particularly through a combination of Cyclic Voltammetry (CV), spectro-electrochemical measurements, and Scanning Probe techniques [32] [33]. Understanding how

these surfaces maintain their structural integrity during electrochemical processes and how lateral confinement can influence reaction's dynamics is pivotal for advancing nano-electrochemistry and optimizing catalytic performance in practical applications [34] [35].

The upcoming chapters will delve into the rationale behind this focus, detailing how the specific characteristics of Cu(111) vicinal surfaces offer significant advantages for our research objectives. We will explore how these surfaces facilitate the observation of fundamental surface processes, enhance the understanding of surface reactivity, and contribute to the development of refined models in nano-electrochemistry. Through a comprehensive analysis, we aim to elucidate the reasons that make Cu(111) vicinal surfaces particularly valuable for advancing our knowledge in this domain.

1.3 EC-STM in Corrosion Analysis: The Case-Study of the Copper System

EC-STM plays a crucial role in studying the initial phases of corrosion, including passivation and the onset of pitting. This technique is particularly useful for monitoring electrochemical reactivity in real-time, especially when it results in alterations to surface structures, such as during deposition, adsorption, or dissolution events. The application of *in-situ* STM in corrosion research is extremely valuable for examining the structural dynamics of electrochemical redox reactions at metal-electrolyte interfaces. This advanced technique provides detailed insights, down to the atomic scale, into the connections between electrode surface structure and reactivity in the presence of adsorbed chemical species and solvent molecules under controlled potential conditions [36]. Additionally, it allows researchers to link the structure of surface adlayers and oxides with the underlying substrate lattice, providing high-resolution imaging of electrode

surface topography and enabling the study of phenomena like surface reconstruction, growth, and lattice mismatch [37].

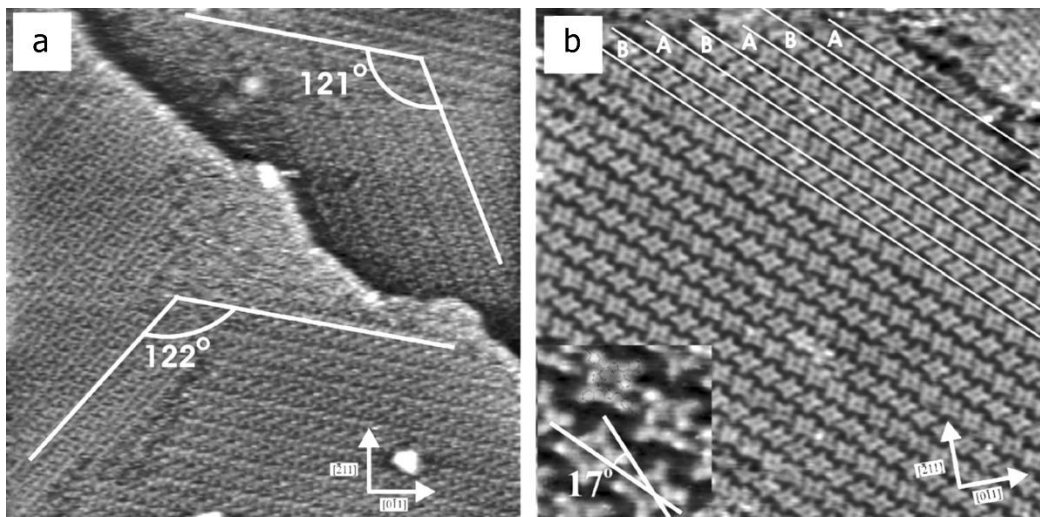


Figure 1.1: [37] STM images of an H₂TMPyP layer on iodide modified Cu(111) (phase I). (a) Monolayer with three rotational domains; image parameters: 41.10 nm × 41.00 nm; $I_t = 0.1$ nA, $U_b = 416$ mV, $E = -350$ mV vs Ag/AgI. (b) Molecular arrangement; image parameters: 27.77 nm × 27.70 nm; $I_t = 0.1$ nA, $U_b = 135$ mV, $E = -350$ mV vs Ag/AgI; inset: molecular rotation by 17° vs direction of rows. The small arrows indicate crystallographic directions $(\bar{2}11)$ and $(1\bar{1}0)$ of the Cu(111) substrate.

Namely, the self-assembly of atoms and molecules like porphyrins on precisely defined surfaces is gaining significant attention. This approach is promising for creating nanoscale surface patterns with specific functionalities, such as electronic, sensory, or catalytic properties. Porphyrins are particularly notable due to their essential roles in both biology and technology, owing to their distinctive electronic and reactive features. These compounds are key players in natural processes like oxygen transport and storage via heme in blood, and photosynthesis in green plants through chlorophyll [38]. Additionally, porphyrins have a wide range of applications, including in photodynamic therapy as drug agents, as electrocatalysts for the reduction of organic and inorganic nitro compounds, and in chemical sensing through various assemblies [39]. For instance, the self-assembly of meso-tetra (N-methyl-4-pyridyl) porphyrine tetratosylat (H₂TMPyP)

molecules on an iodide modified Cu(111) surface from solution has been thoroughly analyzed [37] (*see* Figure 1.1).

While it is truth that controlling the self-organization of molecular layers on both conductive and dielectric substrates is considered a crucial element in the successful design, characterization, and fabrication of nanoscale molecular devices, the optimal control of surface structure is clearly achieved by employing well-defined single crystalline electrodes [40]. The choice of the substrate (composition and structure) is of particular importance under electrochemical control affecting the adsorption, the ordering, the phase transitions and the structural formation of molecules or adsorbates at the solid-liquid, *i.e.*, metal-electrolyte, interface. The electrode potential plays a dual role: it governs the surface coverage of the species involved based on their charge states and can also trigger electron transfer processes between the surface and the adsorbates, such as redox reactions [41]. These redox reactions alter the charge state of the adsorbed species, which in turn affects the electrostatic interactions within the adsorbed layer and between the adsorbate and the electrode. Given that electrostatic forces are crucial for the arrangement, stabilization, and ordering of the adsorbed species on the electrode surface under electrochemical conditions in aqueous electrolytes, redox processes are likely to induce structural changes in the adlayer [42]. In addition, since achieving atomic resolution with STM necessitates a well-defined, atomically flat electrode surface, the selection of the substrate and its meticulous preparation are critical considerations. The necessity for conducting substrates in STM imaging excludes experiments on metals that develop thick, electrically insulating oxide films, where *in-situ* AFM is a more suitable alternative. However, obtaining atomically resolved images with AFM is considerably more challenging. In the history of STM, various substrates, such as noble metals, base metals, semiconductors, and certain metal oxides, have been studied as suitable electrodes. However, it remains valid that, to understand surface structure–reactivity relationships at the atomic scale, single crystalline surfaces with controlled orientations are essential. Specifically, metallic platinum (Pt), gold (Au) or iridium (Ir) single crystals can be prepared using the flame-annealing and

quenching methods [43] [44] [45] . Base metals such as nickel (Ni), cobalt (Co), iron (Fe) and copper (Cu) are conversely susceptible to oxidation when subjected to these techniques. In these cases, atomically flat terrace-step structures can be achieved through chemical or electrochemical etching followed by high-temperature annealing in a hydrogen atmosphere.

In our model study, we utilized a Cu(111) single crystal electrode. Copper was selected not only for its importance as the "metal of the 21st century" in the fabrication of nanoscale circuitry, particularly in the damascene electroplating process and on-chip wiring, but also due to its wider potential window, which extends to more negative values compared to other common metallic electrodes like gold and platinum [45] [46]. This allows for the exploration of phenomena occurring under more reactive or reductive conditions. For example, the adsorption of chloride, bromide, and iodide on Cu(111), Cu(100) and Cu(110) surfaces in aqueous solutions containing the respective halide anions have been extensively investigated, revealing well-defined surface structures and notable changes in surface morphology [47] [48] [49] [50].

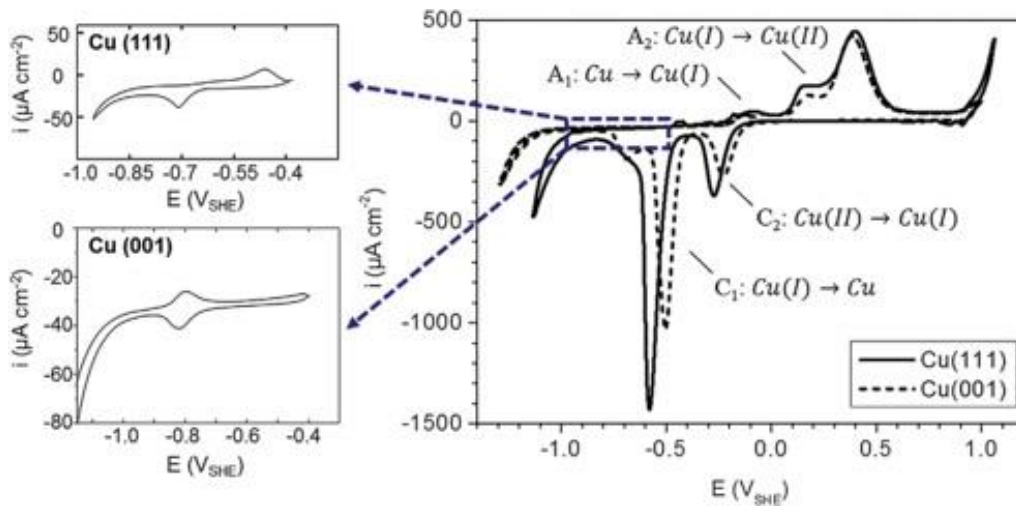


Figure 1.2: [50] Electrochemistry of the systems Cu(111) (solid line) (modified from ref. [51]) and Cu(001) (dashed line) (modified from ref. [52]) in 0.1 M NaOH; left: OH adsorption is visible in the underpotential range of oxidation for Cu(111) (modified from ref. [53]) and Cu(001) (modified from ref. [52]).

Electrochemical scanning tunneling microscopic studies of copper oxide formation were conducted on Cu(111) in 0.1 M NaOH solution. Figure 1.2 highlights the characteristic potentials associated with the formation of anodic Cu(I) and Cu(II), as well as their corresponding cathodic reduction peaks are clearly visible and labeled accordingly in the image [50]. Upon applying a potential step to 0.60 V on the Cu(111) surface, OH adsorption triggers an adsorbate-induced reconstruction process, as illustrated in Figure 1.3 [50]. This process is evident from the increasing coverage of the initially metallic terraces, *i.e.*, bare terraces, (marked "M" in Figure 1.3), by darker 2D islands (marked "ad" in Figure 1.3). These islands expand laterally over time, eventually merging to cover the terraces completely. This reconstruction is also accompanied by the lateral expansion of the terraces. The initial growth of the adsorbate layer predominantly begins at the step edges, highlighting their increased reactivity: a common observation in surface science and interfacial electrochemistry at both solid/gas and solid/liquid interfaces. This lateral expansion is interpreted through a structural model for the adsorbed phase, wherein the uppermost copper layer of the Cu(111) surface rearranges from the close-packed (111) metallic copper structure into the hexagonal configuration characteristic of the Cu planes in (111)-oriented Cu₂O. This transformation results in a 30% reduction in atomic density within the topmost copper layer. The excess copper atoms migrate to the terrace step edges, facilitating lateral terrace growth. Once the reconstruction is complete and the surface is fully covered by OH, the process concludes with the formation of protruding ad-islands made up of copper metal aggregates. At low adsorption overpotentials, OH adsorbates tend to nucleate preferentially at the edges of terrace steps. This behavior is not observed at higher overpotentials because the increased density of nucleation centers leads to more uniform nucleation across the surface [50] [53].

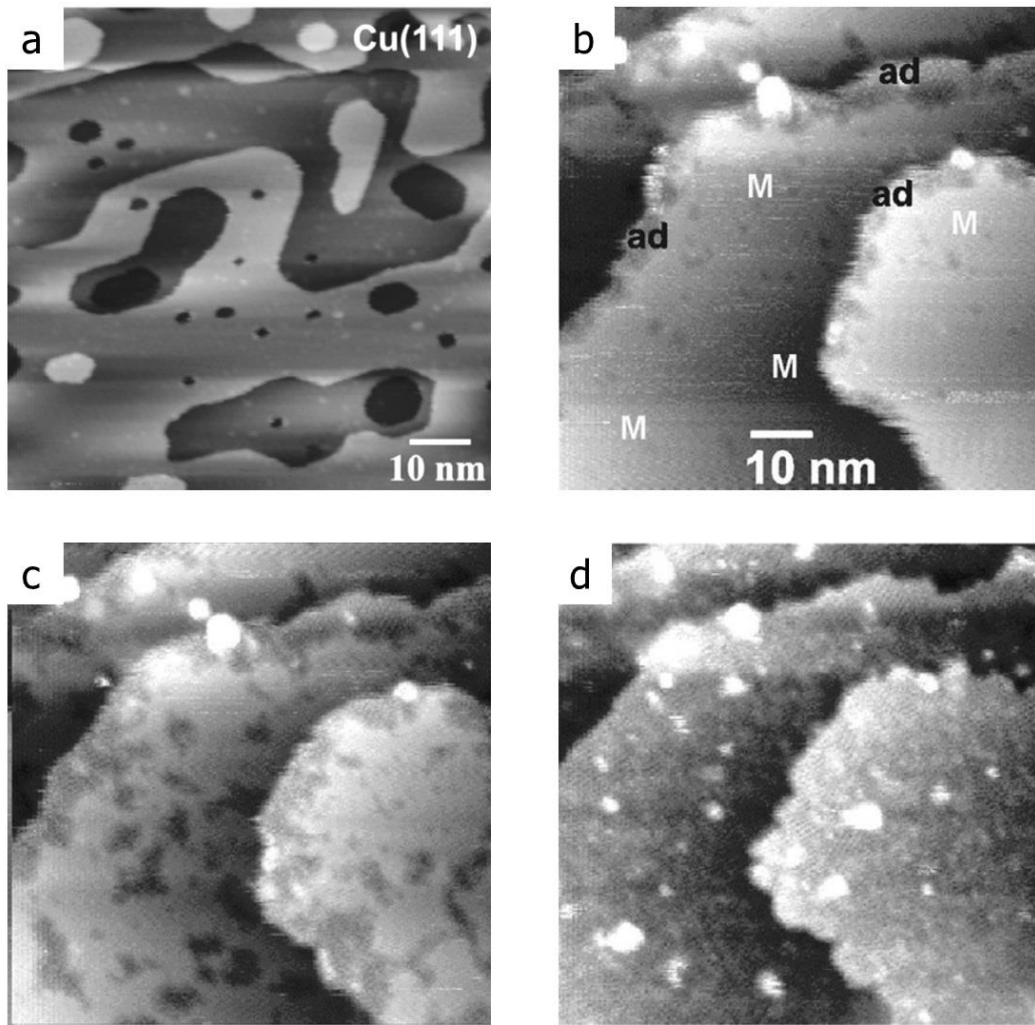


Figure 1.3: [50] (a) EC-STM image of metallic Cu(111) (modified from ref. [52]) in 0.1 M NaOH at $-0.80 V_{SHE}$ after reduction of the native oxide. (b-d) Series of EC-STM images showing the growth of the OH adsorbate (ads) layer on Cu(111) in 0.1 M NaOH at $-0.6 V_{SHE}$; adlayer islands and bare substrate are marked ad and M, respectively (modified from ref. [53]).

The situation is entirely different if, in this configuration, the influence of chloride ions is taken into account. Some nanostructures, not observed in Cl^- free NaOH, result from the interaction of the chlorides with mobile copper atoms at the solid/liquid interface in a solution of 0.1 NaOH / 0.01 NaCl, modifying the adsorption process and the growth of anodic oxide layers on Cu(111). The reaction with hydroxides primarily drives the surface reactivity when the $[Cl^-]/[OH^-]$

concentration ratios are between 0.01 and 10 in alkaline electrolytes ($\text{pH} > 11$). When OH adsorption is examined with small amounts of chlorides added to the electrolyte ($[\text{Cl}^-]/[\text{OH}^-] = 0.1$, $\text{pH} 13$), the excess copper atoms migrating to the step edges become visible as threadlike nanostructures (*see* Figure 1.4 *below*).

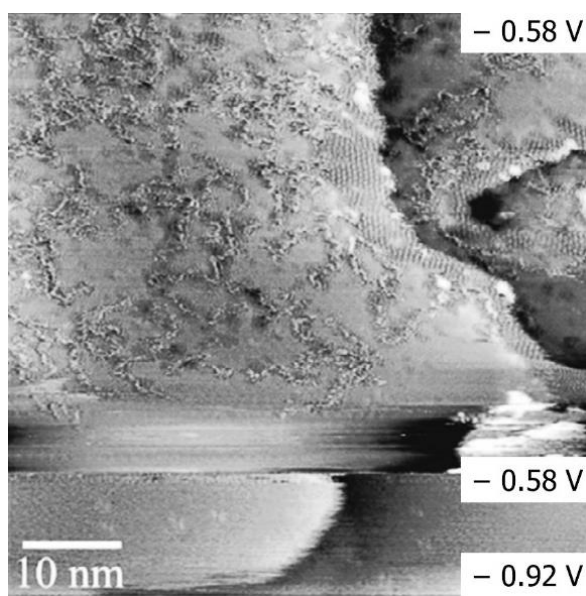


Figure 1.4: [50] EC-STM image of OH adsorbate structure formation on Cu(111) in the potential range before oxidation, in 0.1 NaOH / 0.01 NaCl after a potential step to $-0.58 V_{\text{SHE}}$ (from ref. [49]).

During the early stages of adsorption, OH^- and Cl^- ions compete for available sites at the step edges, where the presence of irregular steps suggests significant copper atom mobility on the surface. This combined and competitive ions' adsorption leads to the formation of the threadlike structures, no longer visible once OH adsorption is complete, as their mobility becomes sufficiently low to be observed by STM. This contrasts with the situation in the absence of chloride ions, where the copper atoms displaced by the Cu(111) reconstruction are not detectable with STM [50].

Interaction between Cu(111) surface and aqueous perchloric acid HClO_4 0.1 M was fully investigated by cyclic voltammetry and *in-situ* EC-STM, revealing a complex potential dependent phase behavior [54]. In STM images of Cu(111)

immersed in a 0.1 M HClO_4 solution, a prominent long-range hexagonal superstructure is observed across the entire Cu(111) surface within the potential range of -350 mV to -150 mV, just before significant hydrogen evolution occurs (see cyclic voltammetry in Figure 1.5).

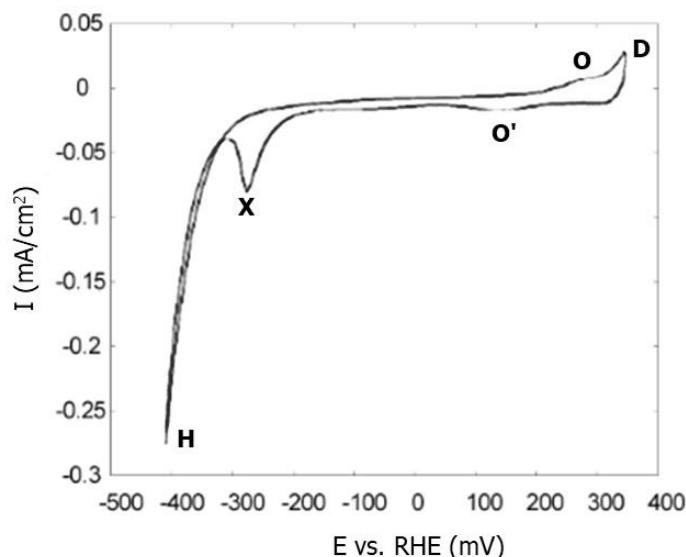


Figure 1.5: [54] Cyclic voltammogram of Cu(111) in 0.1 M HClO_4 ; scan rate $dE/dt = v_{scan} = 10$ mV/s; H: hydrogen evolution; O/O': oxygen-containing species ad-/desorption; D: anodic copper dissolution; X, unknown.

This superstructure can be described by a (4×4) unit cell, which remains aligned with the unit cell of the bare Cu(111) substrate. One of the key characteristics of this (4×4) structure is its strong dependence on the tunneling current (I_t) and bias voltage (U_b) for its imaging properties. By meticulously adjusting these tunneling parameters, various substructural features of the (4×4) structure in pure HClO_4 solution could be visualized, each revealing different electronic states contributing to the tunneling process (Figure 1.6).

Interestingly, this identical (4×4) structure has been observed on Cu(111) in less acidic, neutral electrolytes, and even in the presence of a variety of anions and cations, including dilute sulfuric acid (H_2SO_4), hydrobromic acid (HBr), hydroiodic acid (HI), and potassium sulfate (K_2SO_4). This widespread occurrence

suggests that the superstructure is likely associated with a solvent species such as H_3O^+ and OH^- or with related hydroxyl species. The possibility of a pure water adlayer is discounted due to structural considerations and the weak interaction of water molecules with metal surfaces.

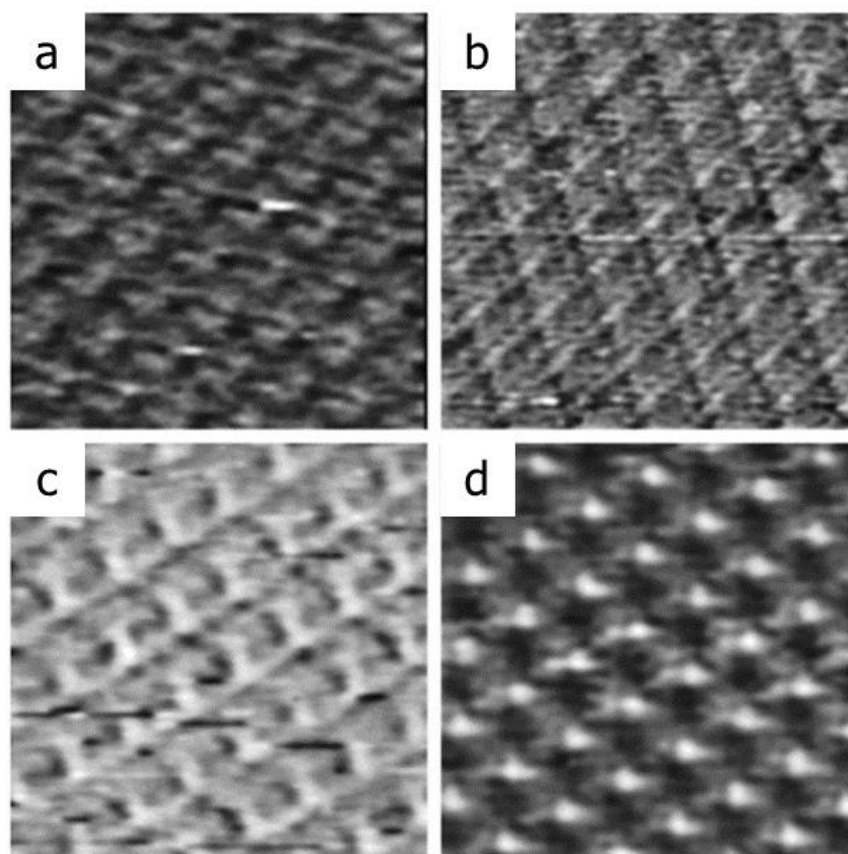


Figure 1.6: [54] STM images of the (4×4) structure in pure 0.1 M HClO_4 at different tunneling parameters, $6.2 \text{ nm} \times 6.2 \text{ nm}$. (a) $E = -150 \text{ mV}$, $U_b = 50 \text{ mV}$, $I_t = 20 \text{ nA}$; (b) $E = -325 \text{ mV}$, $U_b = 5 \text{ mV}$, $I_t = 50 \text{ nA}$; (c) $E = -250 \text{ mV}$, $U_b = 100 \text{ mV}$, $I_t = 10 \text{ nA}$; (d) $E = -250 \text{ mV}$, $U_b = 40 \text{ mV}$, $I_t = 40 \text{ nA}$.

At potentials between -150 mV and $+50 \text{ mV}$, however, the adsorbate-free (1×1) $\text{Cu}(111)$ structure can be imaged with atomic precision in HClO_4 solution (Figure 1.7a). At potentials beyond this range, the surface topography becomes increasingly complex, leading to the formation of furrows (Figure 1.7b), which results in a loss of atomic resolution. Instead of a well-ordered structure, a

disordered layer forms, which is attributed to the adsorption of an oxygen species, most likely hydroxide. When the electrode potential reaches +250 mV, the onset of anodic copper dissolution makes STM imaging challenging as the tungsten tip begins to degrade [54].

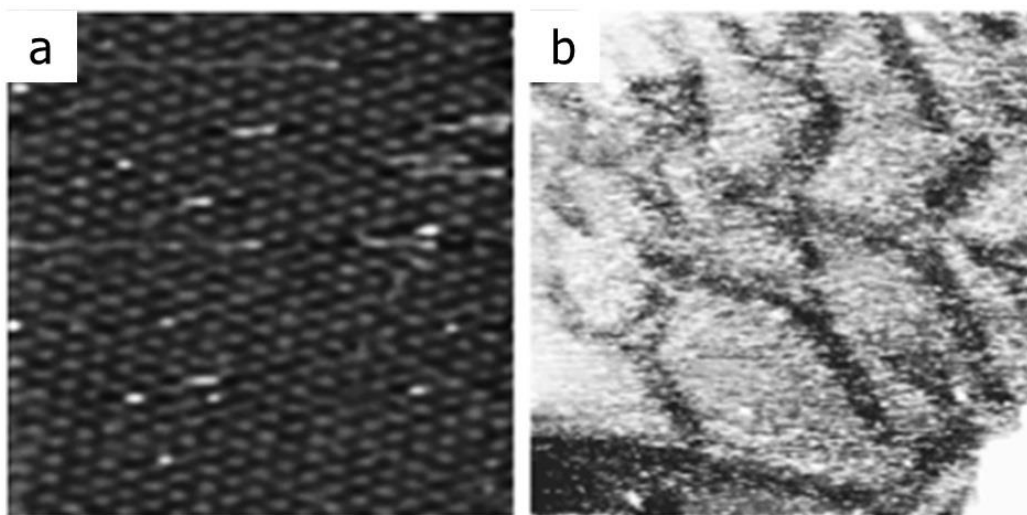


Figure 1.7: [54] (a) STM image of the (1×1) Cu(111) structure under pure 0.1 M HClO₄, $4.3 \text{ nm} \times 4.3 \text{ nm}$; $E = -160 \text{ mV}$, $U_b = 4 \text{ mV}$, $I_t = 50 \text{ nA}$. (b) Surface topography at more positive potentials, $40.6 \text{ nm} \times 40.6 \text{ nm}$; $E = +50 \text{ mV}$, $U_b = 100 \text{ mV}$, $I_t = 1 \text{ nA}$.

If the electrolyte is replaced with a mixture of 0.1 M HClO₄ and 0.01 mM cinchonidine, the same surface phases are observed across the entire potential range from -350 mV to $+250 \text{ mV}$ as in the absence of cinchonidine. No evidence was found to indicate the formation of an ordered cinchonidine adlayer. The only discernible structure at potentials lower than -150 mV was the (4×4) superstructure, which had already been observed in the pure 0.1 M HClO₄ solution, as illustrated in Figure 1.8 [54].

The complex behavior of Cu(111) in pure 0.1 M HClO₄ is just one of the cases of interaction between this electrode and dilute acidic aqueous solutions. The whole range of processes occurring at a single crystal Cu(111) electrode in a sulfuric acid electrolyte (5mM H₂SO₄) between hydrogen evolution and copper dissolution has been studied using a combination of cyclic voltammetry and *in-situ* scanning

tunneling microscopy [55]. The advent of modern spectroscopic and microscopic methods has made it possible to investigate these solid–liquid interfaces *in-situ* with the same level of resolution and accuracy that is standard in surface science studies conducted under UHV conditions, unlike traditional electrochemical techniques, which measure quantities like charge, current, and capacitance and provide only averaged information over the entire electrode surface or sometimes unknown portions of it.

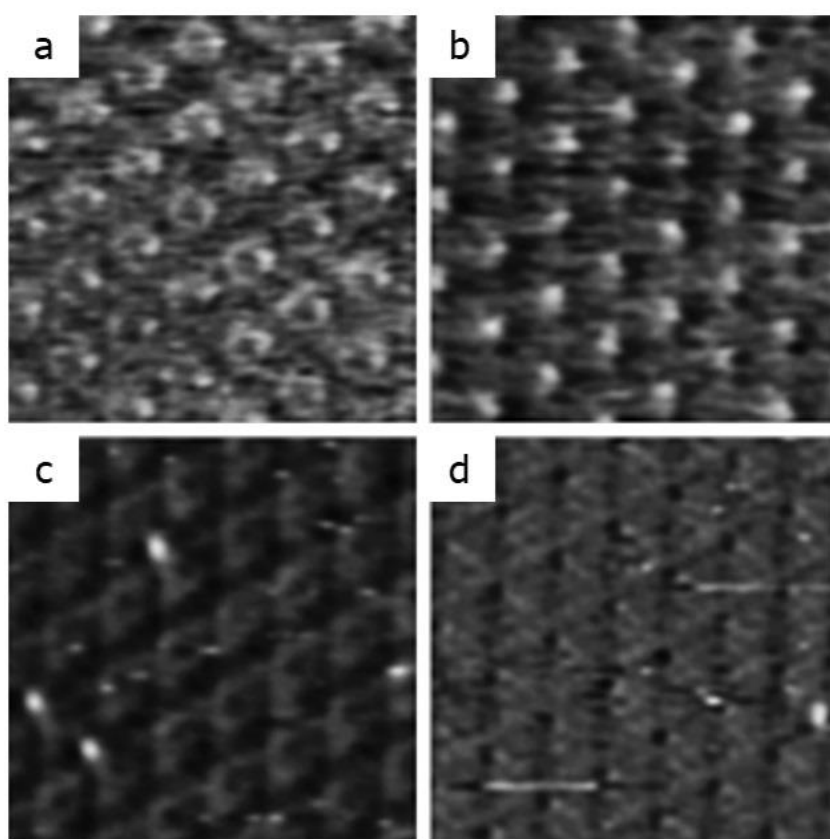


Figure 1.8: [54] STM images of the (4×4) structure in the presence of cinchonidine at different tunneling parameters, $6.2 \text{ nm} \times 6.2 \text{ nm}$. (a) $E = -300 \text{ mV}$, $U_b = 80 \text{ mV}$, $I_t = 20 \text{ nA}$; (b) $E = -300 \text{ mV}$, $U_b = 60 \text{ mV}$, $I_t = 20 \text{ nA}$; (c) $E = -300 \text{ mV}$, $U_b = 40 \text{ mV}$, $I_t = 50 \text{ nA}$; (d) $E = -350 \text{ mV}$, $U_b = 9 \text{ mV}$, $I_t = 50 \text{ nA}$.

In the context of studying in this research surface interactions and structural phenomena, sulfate adsorption on Cu(111) in a 5 mM $\text{H}_2\text{SO}_4(\text{aq.})$ solution was

selected as a *reference system* for its clear and instructive behavior at potentials below the oxidation threshold. This choice is underpinned by the ability of sulfate ions to adsorb onto the Cu(111) surface, leading to the formation of a well-defined adlayer with a distinctive superstructure, commonly referred to as the Moiré-superstructure. The Moiré pattern, which emerges from the interaction between the adsorbed sulfate and the underlying copper surface, provides a unique opportunity to investigate surface phenomena at the nanoscale. This superstructure is not only a hallmark of the adsorption process but also a valuable feature for detailed structural analysis: EC–STM is particularly well-suited for this purpose, as it enables the precise observation and characterization of the Moiré pattern with atomic resolution [56] [57] [58].

2.

Cu(111) in H₂SO₄ 5 mM

2.1 The Interaction Between Cu(111) Surface and SO₄²⁻ Anions

The Pourbaix diagram for copper in diluted solution of H₂SO₄ 5 mM is illustrated in Figure 2.1. A Pourbaix diagram is a graphical representation that plots the equilibrium potential of electrochemical reactions against pH levels. It provides valuable insights into how corrosion mechanisms can be analyzed based on various factors, including pH, temperature, and the concentrations of the reacting species. These diagrams are essential tools in predicting the stability of different phases (such as metals, oxides, and ions) and in understanding the conditions under which a material might corrode, passivate, or remain immune to corrosion. Understanding aqueous corrosion is crucial across various industries. The longevity and safety of chemical plants, offshore platforms, ships, and other infrastructure heavily rely on the ability to control and predict corrosion rates and the resulting corrosion products. Effective corrosion management ensures the structural integrity and operational safety of these critical systems. Corrosion refers to the degradation of materials through chemical interactions with their environment. Unlike erosion or wear, which are mechanical processes, corrosion specifically involves chemical reactions. Aqueous corrosion, in particular, is the oxidation of a metal through electrochemical reactions that occur in water and its

dissolved substances. Therefore, this type of corrosion requires the presence of water, which functions as an ion-conducting electrolyte.

Copper demonstrates relative stability in aqueous solutions, though it oxidizes when exposed to air.

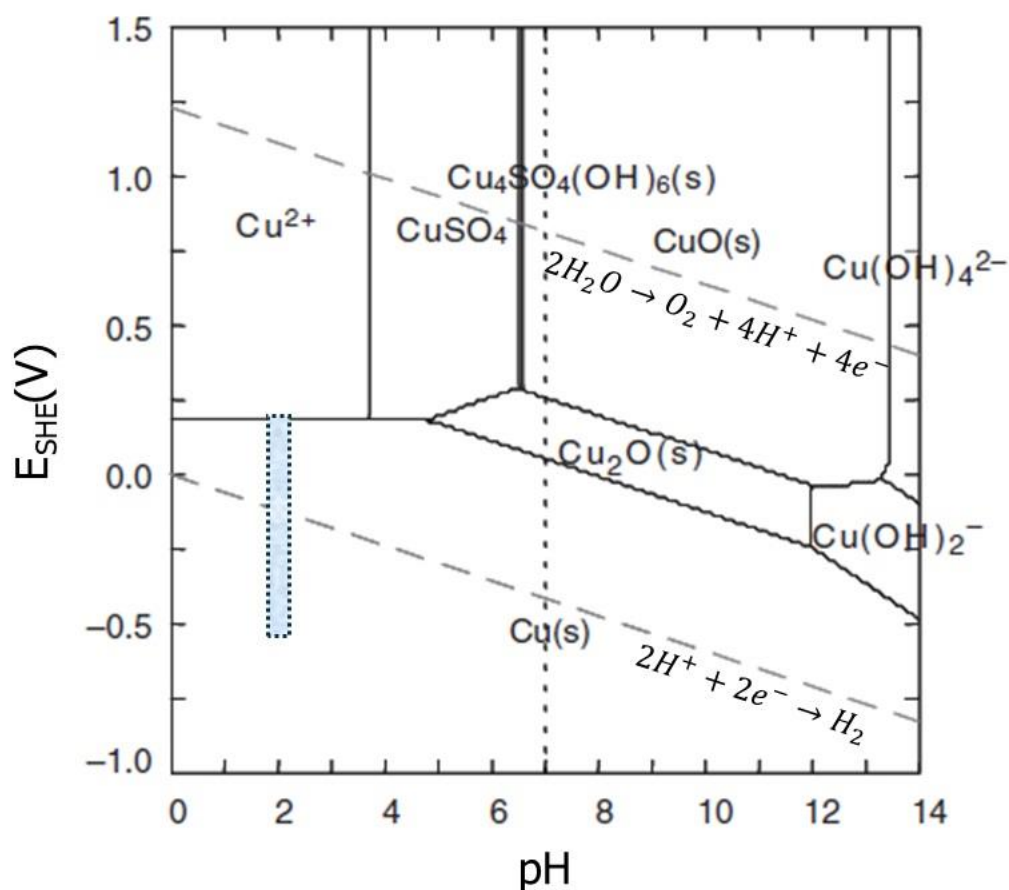


Figure 2.1: [45] Pourbaix diagram calculated at $[Cu^{2+}] = 10\mu M$ and $[SO_4^{2-}] = 5mM$ at $25^\circ C$. The area highlighted in light blue, that corresponds to $pH = 2$, is the region of our interest, for a diluted solution of H_2SO_4 5 mM.

According to the Pourbaix diagram (Figure 2.1), copper remains immune across the entire pH range when subjected to slightly cathodic potentials. Under anodic conditions, copper exhibits amphoteric behavior: it dissolves as Cu^{2+} in acidic environments, forms crystalline Cu_2O and CuO in neutral to mildly alkaline conditions, and dissolves to form soluble hydroxide complexes at high pH levels.

In slightly acidic solutions, Cu²⁺ ions form soluble complexes with sulfate ions, which precipitate as copper hydroxy sulfates near neutral pH: the growth's stability and the thickness of anodic oxides on copper are influenced by the applied potential [45] [59] [22].

A typical steady-state cyclic voltammogram illustrating sulfate adsorption and desorption on Cu(111) in a 5mM H₂SO₄ aqueous solution (pH = 2) is depicted below, in Figure 2.2.

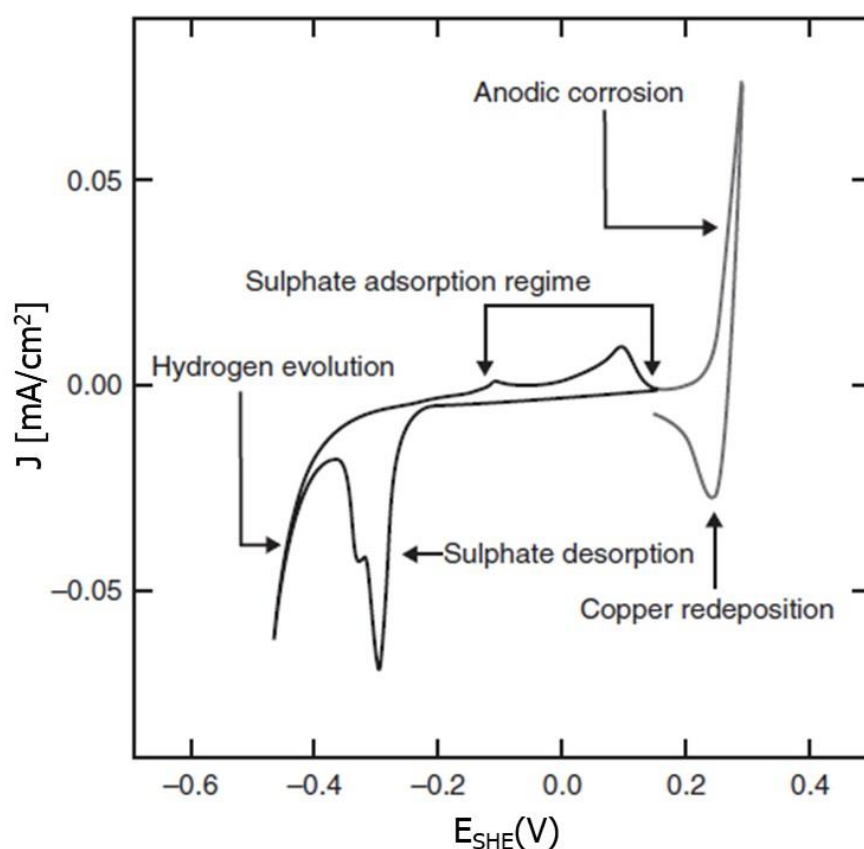


Figure 2.2: [45] Typical steady-state cyclic voltammogram of a Cu(111) electrode in 5mM H₂SO₄; scan rate $dE/dt = v_{scan} = 10mV/s$.

In sulfuric acid solutions, at potentials lower than the oxidation potential of copper (see Figure 2.2), sulfate ions adsorb onto the copper surface. As mentioned above, sulfate adsorption on Cu(111) at these potentials serves as an excellent model system for learning EC–STM, as the sulfate forms an adlayer with a distinct

superstructure. This superstructure creates a Moiré pattern characterized by a regular arrangement of local minima and maxima that extend across the atomically flat terraces of the copper surface. In the SO_4^{2-} induced structure, the distance between the minima and maxima is significantly larger than the atomic spacing of the adsorbed sulfate ions. Consequently, the resulting structure is not at atomic structure but rather a long-range height modulation (z-corrugation), which is defined as a Moiré structure. Despite the underlying substrate lattice that has an ideal hexagonal symmetry, the Moiré pattern appears to be an anisotropic structure, with the periodicity varying across the three directions. As a direct result of the observed anisotropy in the Moiré structure, different domains of the structure can be identified on the surface, each rotated by 120° relative to the others, as clearly visible in Figure 2.3.

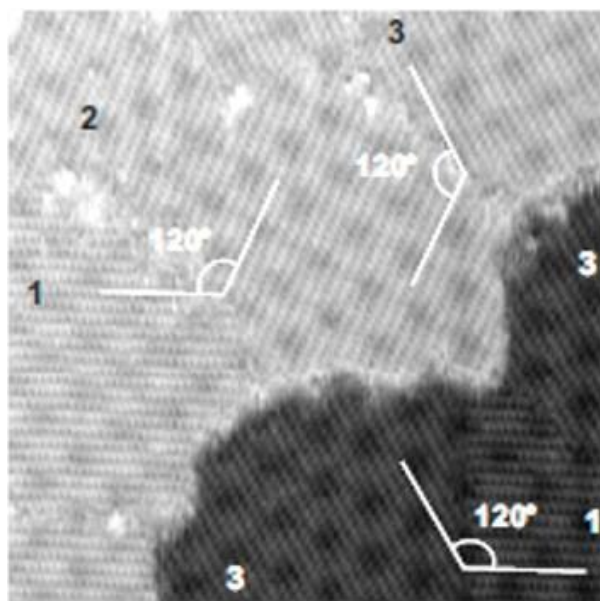


Figure 2.3: [60] 26 nm x 26 nm; rotational domains (1, 2, 3) of the sulfate-induced Moiré structure; bias voltage $U_b = 100$ mV; tunneling current $I_t = 1$ nA; electrode potential $E = 210$ mV.

A detailed examination of one such domain is shown in Figure 2.4b, revealing the atomic-scale structure. The brighter dots in the image represent the sulfate molecules, which are organized into rows. Within these rows, the sulfate

molecules have an intermolecular spacing of 0.47 nm, accompanied by a long-range height modulation that reaches a maximum of 0.04 nm [60]. Between these rows, it is suggested that either hydrogen ions, hydronium ions, or water molecules co-adsorb on the surface, forming zigzag chains of spots with lower intensity, as highlighted in the upper right corner of Figure 2.4b. Therefore, the weaker but distinct dots, observed between the rows of sulfate molecules, are attributed to co-adsorbed water molecules that form characteristic zig-zag chains. Given the strong affinity of sulfate anions for water in aqueous solutions, it is reasonable to assume that these anions retain part of their solvation shell even after adsorption onto the electrode surface. This retained solvation likely plays a crucial role in stabilizing the sulfate adlayer through hydrogen-bridge bonds. These bonds not only contribute to the stability of the adsorbed layer but also explain the unusual anisotropic spacing observed between the negatively charged sulfate anions [55] [57] [61].

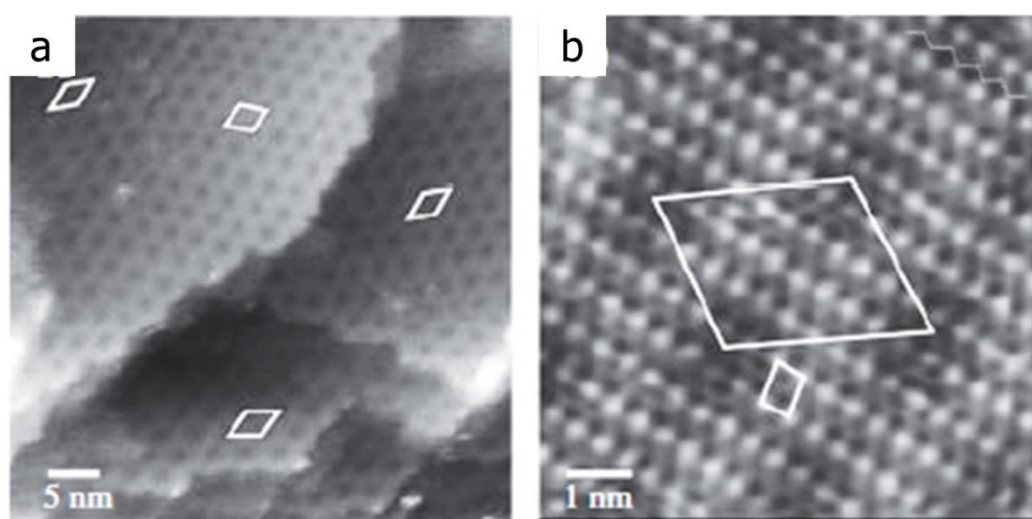


Figure 2.4: [45] Moiré pattern formed on Cu(111) in 5mM H₂SO₄ as reported by Maurice et al. [61]. The STM images are captured at $U_b = -0.1 V_{SHE}$, $E_{tip} = 0.15 V$, $I_t = 1 nA$. (a) The Moiré pattern at nanometric resolution, $50 nm \times 50 nm$, z range = 1.13 nm; (b) Atomic resolution showing the adsorbed sulfate ions and the co-adsorbed cations in a zigzag arrangement in between the sulfate rows, $7.9 nm \times 7.9 nm$, z range = 0.12 nm.

Moreover, the presence of these hydrogen-bridge bonds might clarify the debate regarding whether the adsorbed species are sulfate or bisulfate. Unlike sulfates, adsorbed halides such as chloride and bromide do not exhibit this water co-adsorption phenomenon. This difference can be attributed to the lower heats of solvation of halides, which reduces their interaction with water molecules on the electrode surface [55]. More to the point, the Moiré pattern observed on Cu(111) in 5mM H₂SO₄ exhibits depressions that are approximately 0.4 nm deep and unit cell parameters of 2.8 ± 0.2 nm, 3.2 ± 0.2 nm, and $57 \pm 5^\circ$, as marked in Figure 2.4a and b. For the adsorbed sulfate ions, the corresponding parameters are 0.46 ± 0.02 nm, 0.65 ± 0.02 nm, and $75 \pm 3^\circ$ [45] [62].

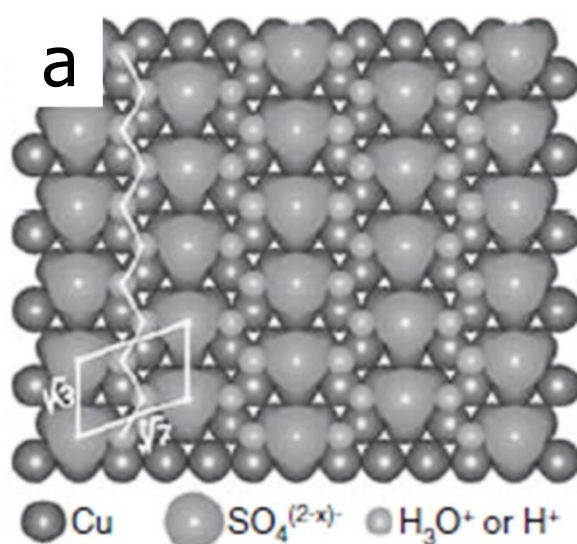


Figure 2.5: [45] (a) Model of the structure of the sulfate adlayer forming a $(\sqrt{3} \times \sqrt{7})$ structure on the Cu(111) surface.

A structural model for the sulfate adlayer and the co-adsorbed layer structure formed below the oxidation potential on the Cu(111) surface is shown in Figure 2.5a. This structure is very similar to those related to sulfate layers on other face-centered cubic (FCC) (111) transition metal electrodes, such as gold (Au), platinum (Pt), palladium (Pd), iridium (Ir) and rhodium (Rh) when immersed in

dilute sulfuric acid electrolytes. These adlayers typically exhibit a $\begin{pmatrix} 2 & 1 \\ 1 & 2 \end{pmatrix}$ unit cell configuration. Although this structure is often referred to in the literature as a $(\sqrt{3} \times \sqrt{7})R30^\circ$ structure, this designation is not entirely accurate. For simplicity, it can be also referred to as the $(\sqrt{3} \times \sqrt{7})$ structure [60]. The presence of water molecules within the unit cell likely plays a crucial role in maintaining the integrity of the adlayer and its characteristic structure on the copper electrode. Comparing the sulfate adlayer on Cu with those on other FCC(111) surfaces, a fundamental difference becomes evident. On other FCC(111) metals, such as Au, Pt, Pd, Ir, and Rh, the sulfate adlayers are typically commensurate with the underlying metal lattice. In contrast, on copper, the sulfate adlayer is characterized by an additional long-range Moiré-type modulation [56] [60]. According to Broekmann *et al.* [60], two strategies have been considered to explain the observed Moiré effect on Cu(111):

1. **Weak Interaction Scenario:** In this scenario, the interaction between sulfate molecules and the copper substrate is relatively weak. The adlayer, therefore, forms an incommensurate structure with varying adsorption sites for individual sulfate molecules. This explanation aligns with known Moiré structures from UHV adsorption systems, where weak interactions can lead to such incommensurate structures.
2. **Commensurate Structure with Distorted Lattice:** Alternatively, the sulfate structures on other FCC(111) surfaces (such as Au, Pt, Pd, Ir, and Rh) are fully commensurate with the substrate. For these metals, the lattice vector of the sulfate adlayer's unit cell adjusts to match the underlying metal lattice. As the interatomic distance shrinks across these metals, the sulfate layer's unit cell also contracts. For instance, on Rh(111), the lattice parameters are $a = 0.46$ nm and $b = 0.74$ nm. Given that the Cu–Cu distance is shorter (0.256 nm) compared to Rh(111) (0.268 nm), the sulfate lattice on Cu(111) would be expected to shrink further, potentially resulting in a =

0.443 nm to maintain commensurability between the sulfate overlayer and the Cu(111) substrate. However, the measured distance $a = 0.46$ nm is significantly larger, indicating that the sulfate overlayer does not achieve full commensurability with the Cu(111) substrate. This discrepancy suggests that the Moiré effect on Cu(111) arises (and not on the other FCC(111) surfaces) from the unique interplay between sulfate molecules and the copper surface. The strong interactions between the sulfate anions and the copper substrate leads to a significant reconstruction of the copper surface, causing the topmost layer to expand. This expansion is hypothesized to allow the sulfate adlayer to fit commensurately on the expanded copper surface. The Cu–Cu distances in this expanded top layer are thought to be similar to those found on Rh(111), where the sulfate adlayer achieves maximum density without further compression. The sequence of interatomic distances ($Au > Pt > Pd > Ir > Rh$) suggests that Rh(111) represents a limit in terms of how much the sulfate adlayer can compress. Hence, when transitioning from Rh to Cu, instead of further compressing the sulfate adlayer, the strong interaction with copper causes the topmost layer of copper atoms to expand. This expansion prevents the need for further compression of the sulfate adlayer, maintaining similar intermolecular distances to those seen on Rh(111). Therefore, the Moiré pattern observed on Cu(111) is unique and is explained by this model as a result of a misfit between the expanded topmost copper layer and the underlying, non-expanded copper layers. The top layer, having been stretched to accommodate the sulfate adlayer, no longer matches the lattice parameters of the underlying copper layers, leading to the distinctive long-range Moiré pattern. Although this scenario might seem unconventional, especially considering the idea of a substrate layer expanding rather than compressing, the evidence supports this model as the correct explanation for the Moiré structure seen on Cu(111) in the presence of sulfate. This strong substrate-anion interaction and subsequent surface reconstruction is

unique to copper and provides a compelling explanation for the observed phenomena.

The scheme of Figure 2.5a was obviously observed directly with *in-situ* STM by Arenz at all (reference [63]), as reported below, in Figure 2.6. The main spots in Figure 2.6 are attributed to adsorbed sulfate molecules whereas the smaller spots arranged in zigzag rows between the sulfate particles are assigned to co-adsorbed water molecules.

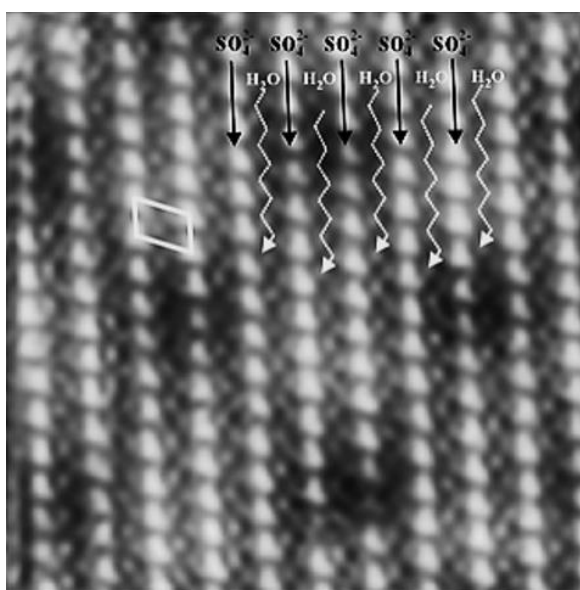


Figure 2.6: [63] Moiré structure, $7.6 \text{ nm} \times 7.6 \text{ nm}$, $I_t = 1 \text{ nA}$, $U_b = -120 \text{ mV}$, $E = -56 \text{ mV}_{RHE}$.

The bare copper surface was found to have parameters of $0.25 \pm 0.02 \text{ nm}$ and $62 \pm 3^\circ$ [45]. This suggests that the adsorbed sulfate species arrange themselves in the $(\sqrt{3} \times \sqrt{7})$ superstructure, with a surface coverage of approximately 0.2 sulfate ions per copper atom ($x = 1$). The charge transfer, estimated from the charge of the cathodic peak during sulfate desorption, matches this surface coverage, confirming the structural findings and corresponds to about 0.2 electrons per metal atom, according to the references [45] and [56].

After the sulfate adlayer has desorbed, the bare copper surface can be imaged with atomic resolution. Figure 2.7a provides an image displaying the typical hexagonal lattice structure of the Cu(111) surface, with the interatomic nearest neighbor separation corresponding to the interatomic Cu-Cu distance reported in literature of 0.256 nm (the ideal bare Cu parameters are in fact 0.256 nm and 60°).

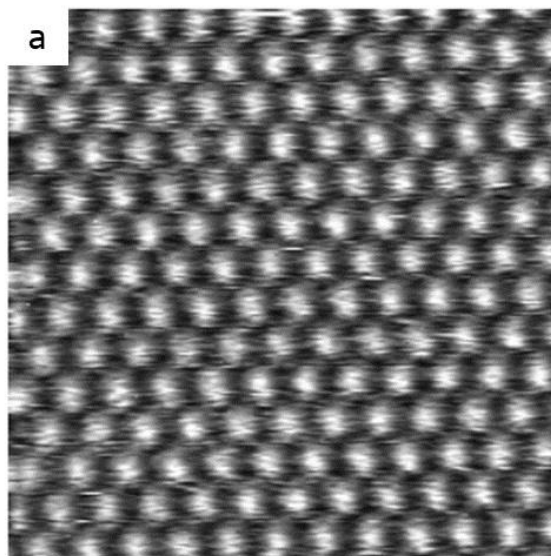


Figure 2.7: [60] (a) *In situ* STM image of the sulfate-free Cu(111) electrode measured potentiostatically in solution. Image size 3 nm × 3 nm; bias voltage $U_b = -10$ mV; tunneling current $I_t = 30$ nA; electrode potential $E = -215$ mV_{RHE}; positive potential sweep.

In addition, Maurice *et al.* [19] explored the impact of pH on sulfate adsorption on Cu(111) and found that as pH increases, water and hydroxide adsorption becomes more significant. In alkaline sulfate-containing solutions (5mM SO₄²⁻, pH 10.5), only hydroxide ions were observed to adsorb on the Cu(111) surface. In neutral sulfate solutions (5mM SO₄²⁻, pH 7), sulfate co-adsorbs with water, forming partially ordered structures; however, no Moiré pattern was detected. In neutral to alkaline sulfate solutions, it was noted that copper oxide forms on the surface at more anodic potentials (*see* the Pourbaix diagram reported in Figure 2.1 for greater clarity).

Note that in the cyclic voltammogram presented in Figure 2.2, the cathodic desorption peak is considerably larger than the corresponding anodic adsorption feature. This discrepancy arises due to an additional hydrogen evolution current from the sulfate-covered copper surface, which is attributed to the Frumkin effect [64]. This effect occurs because the adsorbed sulfate anions increase the concentration of hydronium ions (H_3O^+) near the electrode surface, thereby lowering the overpotential required for the hydrogen reduction reaction. As a result, during the cathodic sweep, an exponentially increasing hydrogen reduction current is first observed on the sulfate-covered electrode, leading to the first rise in the cathodic current feature. As the sulfate begins to desorb, this hydrogen evolution current decreases, creating the first (and largest) peak in the cathodic current. The continued desorption of sulfate ions then generates a second peak, after which the hydrogen evolution current from the now sulfate-free copper surface becomes dominant. This interpretation, which assigns only the second peak to the sulfate desorption process, can be confirmed through a simple experiment. If the potential is cycled only within the range of 150 mV to -300 mV, the exponential increase in cathodic current between -250 mV and -300 mV is observed, but no adsorption features appear in the reverse anodic sweep because the surface remains covered by sulfate ions. As the potential range is extended to more negative values, the true sulfate desorption peak emerges, and consequently, the re-adsorption peak in the anodic sweep grows. It follows that the cathodic double peak is a superposition of an initial hydrogen reduction current (on the sulfate-covered electrode) and the actual sulfate desorption process [60].

In line with the literature [65] [56] [55], the proposal of a sulfate-induced surface expansion on Cu(111) originally emerged from observations of significant mass transport during the formation of the Moiré structure. These phenomena provided indirect but consistent evidence for the proposed expansion of the topmost copper layer under the influence of adsorbed sulfate. The observations include [60]:

- **Mass transport Island Formation:** During the formation of the Moiré pattern on the sulfate-covered Cu(111) surface, small copper islands were

observed nucleating and growing on the terraces. This is a direct consequence of the atomic displacement from the expanding first copper layer. As sulfate adsorbs, it forces the copper atoms to rearrange, leading to the creation of these islands on the surface (Figure 2.8).

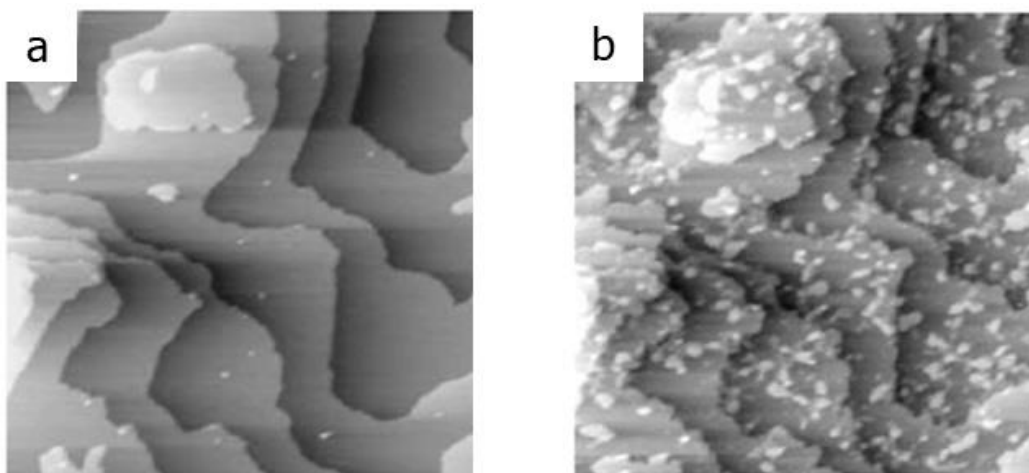


Figure 2.8: [60] Morphological changes induced by sulfate adsorption on Cu(111) in 5mM H₂SO₄ solution. (a) Before sulfate adsorption; image size 340 nm × 340 nm; bias voltage $U_b = -20$ mV; tunneling current $I_t = 1$ nA; electrode potential $E = -266$ mV_{RHE}, positive potential sweep. (b) After sulfate adsorption; 340 nm × 340 nm; $U_b = -20$ mV; $I_t = 1$ nA; $E = 155$ mV_{RHE}, positive potential sweep.

- **Vacancy Islands and Holes:** When the sulfate is rapidly desorbed, a high density of vacancy islands and holes remains on the Cu surface. This occurs because the previously expanded copper layer shrinks back to its normal structure, leaving behind voids where the displaced atoms had been. Over time, these vacancy islands and holes gradually heal as copper atoms diffuse to fill in the gaps, restoring the surface to a more uniform state (see the series of images in Figure 2.9(a-c)).
- **Strain Relief at Step Edges:** Following the literature, the expansion of the copper layer and the relaxation of the compressive strain are most easily

achieved at step edges, which is where the Moiré formation process typically begins. The Moiré structure initially forms at the upper edge of steps and then spreads onto the upper terrace, which can expand towards the lower terrace. This process is evident in STM images where the Moiré structure is observed on the upper terrace.

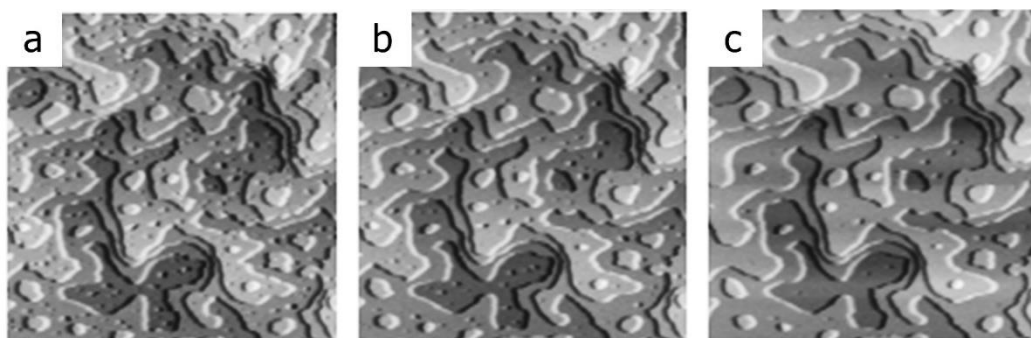


Figure 2.9: [60] (a-c) Morphology of the Cu(111) surface after desorption of the sulfate adlayer as a function of time; recording time for all three images 15 minutes. Tunneling parameters for all images: Size 256 nm \times 256 nm; bias voltage $U_b = -41$ mV; tunneling current $I_t = 10$ nA; electrode potential $E = -210$ mV_{RHE}, positive potential sweep.

- Blocking and Island Growth:** As the Moiré patches grow larger, they increasingly block the channels of strain relief. To continue expanding, copper atoms must be displaced out of the first copper layer and either incorporated into existing step edges or coalesce into new islands. This displacement and island growth are visible in the STM images, particularly where the Moiré pattern spreads, leading to the growth of bright islands.

2.1.1 Sulfate Adsorption and Moiré Structure Formation

The STM images in Figure 2.10 provide valuable insights into the slow and controlled formation of the Moiré structure on the Cu(111) surface during sulfate adsorption [60].

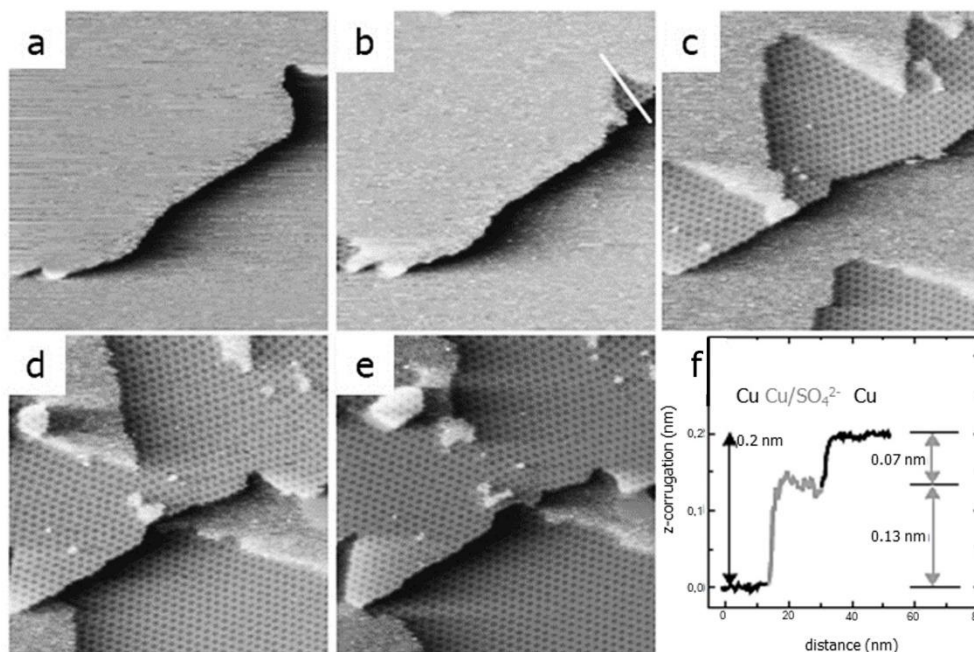


Figure 2.10: [60] (a)–(e) Series of STM images illustrating the process of sulfate-induced Moiré formation. The tunneling parameters for all images are as follows: size $101 \text{ nm} \times 101 \text{ nm}$; bias voltage $U_b = 169 \text{ mV}$, tunneling current $I_t = 1 \text{ nA}$ and electrode potential ($E = -70 \text{ mV}$) versus RHE. The entire series was captured over a duration of 10 minutes. Notably, a Moiré-covered island begins to form in the upper left corner of images (d) and (e). Panel (f) presents a height profile along the white line in (b), revealing the onset of Moiré formation at the upper edge of a step.

Here's a detailed explanation of the process and its implications:

- **Controlled Potential for Adsorption:** The experiment was designed to control the rate of Moiré structure formation by stepping the electrode potential to a constant value of -70 mV vs RHE after initially holding it at a more negative potential where no sulfate was present on the Cu(111) surface. This approach takes advantage of the clear separation between the potential ranges for sulfate adsorption and desorption, as indicated in the characteristic cyclic voltammetry.

- Initial Surface Observation (Figure 2.10a): the first STM image shows two flat terraces of Cu(111) with a monatomic step separating them. At this initial stage, no Moiré structure is visible, indicating that sulfate has not yet adsorbed in ordered form onto the surface.
- Emergence of the Moiré Structure (Figure 2.10b): with the potential held at -70 mV_{RHE}, small patches of the Moiré structure begin to form. These patches appear first at the step edges, growing onto the upper terrace. The profile shown in Figure 2.10f (along the white line in Figure 2.10b) highlights that these emerging Moiré patches appear darker and, thus, lower than the surrounding terrace, which is attributed to their different electronic properties.
- Continued Growth (Figure 2.10(c-e)): as time progresses, the Moiré structure continues to grow steadily from the step edges, eventually covering the entire upper terrace. The series of images shows this gradual expansion, demonstrating the slow kinetics of Moiré formation under these conditions.
- Unusual Behavior of Sulfate on Cu(111): the formation of the Moiré structure in small initial patches is surprising because the negative charge of the sulfate anions would typically lead to repulsive interactions, preventing such early aggregation. The co-adsorbed water molecules likely play a crucial role in stabilizing the Moiré structure by screening the repulsive interactions between the negatively charged sulfate anions. This screening effect allows the sulfate anions to aggregate and form the stable Moiré structure even at an early stage of adsorption.

Therefore, to summarize, the STM observations in Figure 2.10 illustrate the slow and controlled formation of the Moiré structure on Cu(111) during sulfate adsorption. The formation begins at step edges and spreads onto the terraces,

driven by the stability of the Moiré structure and the screening effect of co-adsorbed water molecules. highlighting the unique interactions between sulfate anions and the Cu(111) surface.

2.1.2 Desorption Process Overview

Figure 2.11 [55] shows the complete desorption process, that, in contrast with the adsorption one, is much more rapid and occurs in a relatively small potential window during the cathodic run. As the reconstruction of the copper surface is lifted, the sulfate molecules desorb directly from the surface without the need for the complex reordering that characterized their adsorption.

- **Initial Coverage:** in Figure 2.11*a*, the surface is almost entirely covered by the Moiré structure. The brighter areas on the terraces correspond to defects and disordered regions within the sulfate adlayer, indicating irregularities in the otherwise well-ordered Moiré pattern. These defects serve as initiation points for the desorption process.
- **Desorption Initiation:** the desorption of the Moiré structure begins at the defects and at the lower step edges of the terraces. This observation suggests that these regions are less stable, making them the first sites where the Moiré structure starts to break down.
- **Progression of Desorption:** as desorption progresses, from picture *b* to picture *i*, the Moiré structure gradually disappears. The desorption process moves from the lower to the upper step edges, eventually leading to the complete removal of the Moiré structure. Despite the overall desorption, small patches of the Moiré structure persist until the very end, highlighting the unusual stability and resistance of this structure.

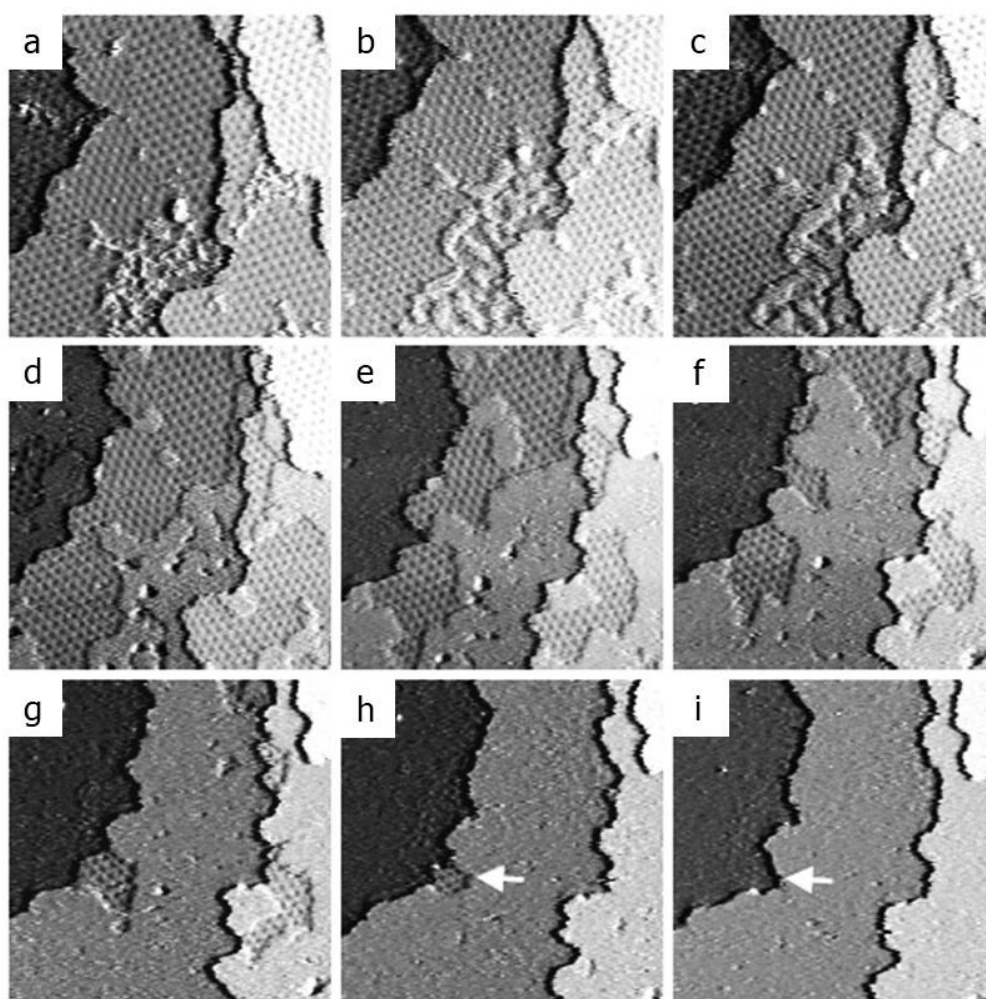


Figure 2.11: [55] Series of STM images showing the decay of the Moiré adlayer; total recording time 15 minutes. Notice the persistence of small Moiré patches at the upper step edges, even when the sulfate coverage is reduced to very low levels (panel h). Tunnelling parameters for all images: size 84 nm × 84 nm; bias voltage $U_b = 40$ mV, tunneling current $I_t = 1$ nA; electrode potential $E = 210$ mV vs RHE.

2.1.3 Unveiling the Moiré-Superstructure: A Comprehensive Analysis through STM Imaging

For further clarity and completeness, the following images again depict the formation of the Moiré-superstructure. In the first image (Figure 2.12), a detailed view of the Moiré pattern formation at the step edges can be observed

[55]. Note how the depressions of the Moiré structure consistently appear closed at the step edges (Figure 2.12a), meaning that these depressions are always fully encircled by rims of adsorbed molecules imaged at higher z values (as shown in parts b and c). This observation confirms the strong substrate-adsorbate interaction, as the adsorbate appears to reinforce the substrate structure at these step edges.

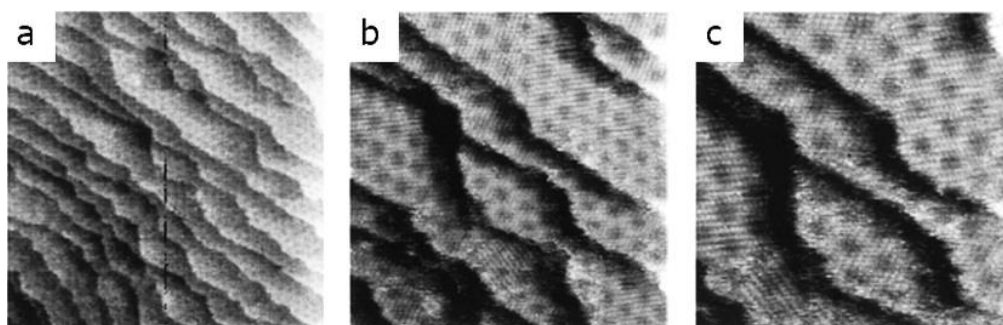


Figure 2.12: [55] *Cu(111)* in 5 mM H_2SO_4 , step orientation of a sulfate covered copper surface: (a) 102 nm \times 102 nm; $I_t = 1$ nA, $U_b = 166$ mV, $E = -465$ mV; (b) 43 nm \times 43 nm; $I_t = 1$ nA, $U_b = 166$ mV, $E = -465$ mV; (c) 29 nm \times 29 nm; $I_t = 1$ nA; $U_b = 166$ mV, $E = -465$ mV. E was measured vs (Hg|Hg₂SO₄)/V.

Be aware that, on the sulfate-covered Cu surface, the steps are aligned parallel to the symmetry axes of the Moiré structure rather than parallel to the close-packed adsorbate rows (see Figure 2.13). The kinks observed correspond to the termination of a chain of complete Moiré-units, illustrating that the Moiré-unit serves as the stable building block (as will be explained in much greater detail later).

A particularly important and distinctive feature of cyclic voltammetry of *Cu(111)* in sulfuric acid is the large separation between the anodic and the cathodic peaks and, as a consequence, a strong kinetic hindrance for controlling the sulfate adsorption process and the desorption one. By this way, it is possible to have the precise control over the sulfate adsorption rate and over the rate of Moiré pattern formation, by selecting a specific constant adsorption potential.

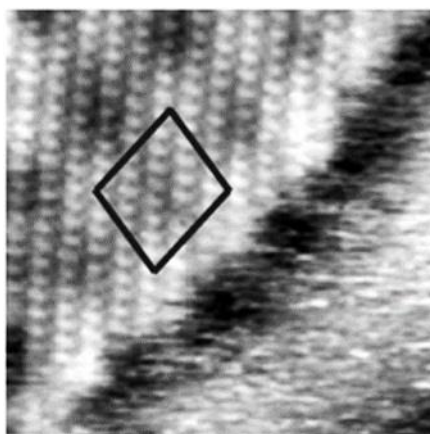


Figure 2.13: [60] The image depicts a sulfate-stabilized copper step on a Cu(111) electrode in a 5 mM H₂SO₄ solution. Observe that only the upper terrace is covered by the Moiré structure, while the lower terrace remains uncovered. Additionally, the step aligns with the rows of Moiré-units rather than with the sulfate rows. One Moiré-unit is indicated in the image. Imaging parameters are as follows: size 13 nm × 13 nm; bias voltage $U_b = -70$ mV, tunneling current $I_t = 1$ nA, electrode potential $E = -80$ mV_{RHE}, during a positive potential sweep.

In Figure 2.14, the authors demonstrate this idea, investigating directly the initial stage of sulfate adsorption and the mechanism underlying the adlayer formation process [55]. In this experiment, the CV potential sweep was halted within a potential range between the cathodic and anodic peaks during the positive voltage sweep. The closer the constant adsorption potential was set to the anodic peak, the more rapidly the adlayer formation occurred. When using more negative adsorption potentials, the Moiré nucleation rate is slow relative to the Moiré growth rate, resulting in copper terraces being covered by a few very large Moiré domains. Conversely, by selecting a more positive adsorption potential, which induces a faster Moiré nucleation rate, the Moiré domain sizes can be reduced, and the number of Moiré domains can be significantly increased.

All STM series of images in Figure 2.14 capture the same area, but at different potentials and times. Initially, the potential sweep was halted far from the adsorption regime at -850 mV_{Hg|Hg₂SO₄}, where two flat terraces of the bare

copper surface are visible (*see* Figure 2.14a). Upon shifting the sample potential to $-800\text{ mV}_{\text{Hg}|\text{Hg}_2\text{SO}_4}$ (Figure 2.14b), the copper surface's imaging properties change significantly, appearing more roughened. This change suggests an initial state of sulfate adsorption resembling a two-dimensional gas phase on the electrode surface with sulfate molecules in motion or adsorbing onto the surface. In Figure 2.14c, the sample potential is further increased to more positive values and the Moiré formation process begins slowly. The adlayer growth predominantly initiates at step edges and extends unusually to the upper terrace, rather than the lower one. Concurrently, the step edges undergo shape changes. In addition to the reorganization of copper steps, there is a slight growth of the terraces, which are immediately covered with the Moiré structure. This suggests that the copper terrace is being slightly stretched by the sulfate adsorbate, as seen in parts (b) and (c) of Figure 2.14.

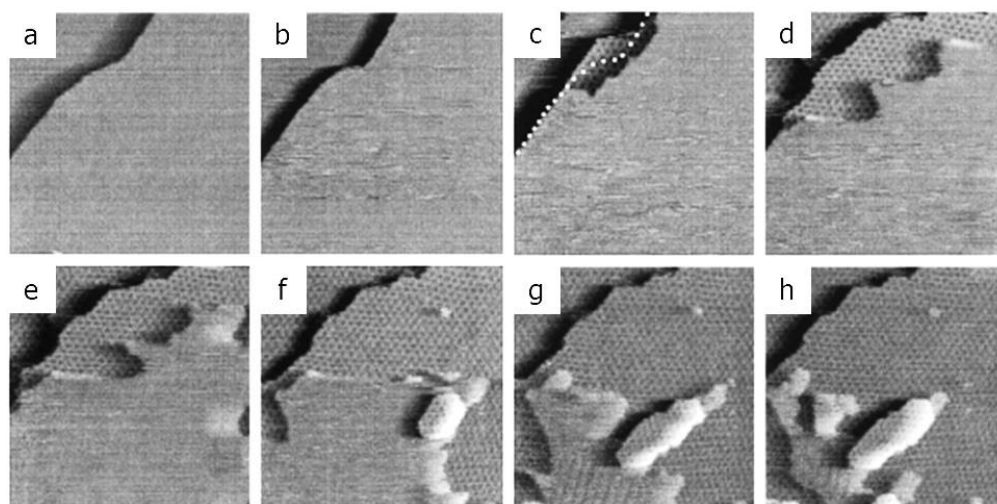


Figure 2.14: [55] Cu(111) in 5 mM H₂SO₄, STM series showing the formation of the Moiré structure: (a–h) 92 nm × 92 nm. (a) $I_t = 1\text{ nA}$; $U_b = 86\text{ mV}$, $E = -850\text{ mV}$. (b) $I_t = 1\text{ nA}$; $U_b = 86\text{ mV}$, $E = -800\text{ mV}$. (c–h) $I_t = 1\text{ nA}$; $U_b = 66\text{ mV}$, $E = -750\text{ mV}$; the time interval between successive images is 70 s; the white dots in panel (c) represent the outline of the copper step shown in panel (b), illustrating how the copper terrace stretches during the Moiré formation. E was measured vs (Hg/Hg₂SO₄)/V.

Comparing the sulfates-covered portion of the upper terrace with the adsorbates-free portion reveals that the Moiré region appears darker in the STM images with respect to the corresponding Moiré-free part, likely due to differences in electronic properties between the adsorbate and the adsorbate-free copper. In the later stages of the STM series (series (f–h) in Figure 2.14), the nucleation and growth of additional Moiré-covered copper islands can be observed on the terraces. Similar to the new areas at the step edges, these new islands are also immediately covered with the Moiré structure. The authors declared that both growth processes suggest that Moiré formation simultaneously induces mass transport from the underlying copper layer during adlayer formation.

2.2 The Impact of Tunneling Current on the STM Resolution of the Moiré-superstructure

To briefly summarize the points discussed so far, sulfate anions co-adsorb with water molecules on the Cu(111) surface at positive electrode potentials, forming a ($\sqrt{3} \times \sqrt{7}$) structure. This structure is aligned with a reconstructed, expanded, and slightly distorted first copper layer. The misalignment between this reconstructed first copper layer and the underlying unreconstructed second copper layer gives rise to the Moiré-superstructure. Direct evidence for the sulfate-induced expansion of the topmost copper layer can be provided through a comparative analysis of EC-STM images obtained under varying tunneling parameters, as demonstrated by Broekmann *et al.* in reference [60]. In this work, the authors present a sequential series of STM images, all recorded at the same sample potential ($E = 100$ mV) but under varying tunneling parameters. The tunneling current was altered between two corresponding images, decreasing from 10 nA to 2 nA. In Figure 2.15a, the expected characteristics of the long-range Moiré modulation, including the distorted hexagonal arrangement of adsorbed

molecules, are clearly visible for this electrode potential. However, in Figure 2.15*b*, while the dimensions of the Moiré-unit cell remain consistent, the molecular resolution is no longer observable. A similar experiment was conducted on an atomic scale, as depicted in Figure 2.15*c* and *d*. Again, a reduction in the tunneling current from 10 nA to 2 nA led to the disappearance of the adsorbed sulfate structure. Instead, a hexagonal structure with a significantly smaller lattice vector becomes apparent. Notably, this structure retains the same distorted long-range Moiré periodicity observed in Figure 2.15*c*. To better illustrate the structural relationship between the two structures, a unit cell of the sulfate adlayer from Figure 2.15*c* is superimposed on the hexagonal structure in Figure 2.15*d*. Therefore, the authors interpreted this coincident overlay in a highly plausible manner, considering Figure 2.15*b* and *d* as STM images of the reconstructed copper surface beneath the sulfate layer.

It is important to note that neither the reconstructed (expanded) copper substrate nor the sulfate structure perfectly matches a hexagonal symmetry, but instead deviates slightly. The authors detected these small distortions judging the thermal drift negligible in the STM images shown in Figure 2.15*c* and *d*. The lattice constants for the reconstructed, sulfate-covered copper surface were determined as $a' = 0.26 \pm 0.01 \text{ nm}$ and $b' = 0.273 \pm 0.01 \text{ nm}$ with the angle between these lattice vectors of $(56^\circ \pm 1^\circ)$, which is a 4° deviation from the ideal 60° (Figure 2.15*d*). This suggests that the slight distortion in the long-range Moiré-superstructure is likely due to this distortion in the reconstructed first copper layer. By selecting tunneling parameters between the extremes of 2 nA and 10 nA, a continuous transition from the sulfate-dominated structure to the copper-dominated structure can be detected. A noteworthy detail is the specific tunneling currents employed to generate Figure 2.15*a-d*. The reconstructed copper structure becomes visible at lower tunneling currents (2 nA, corresponding to a larger tip – sample distance), whereas the adsorbate image emerges at higher currents (10 nA, corresponding to a smaller tip – sample distance). This unexpected behavior suggested that the Cu electron wave functions may extend further into the electrolyte than those of the sulfate.

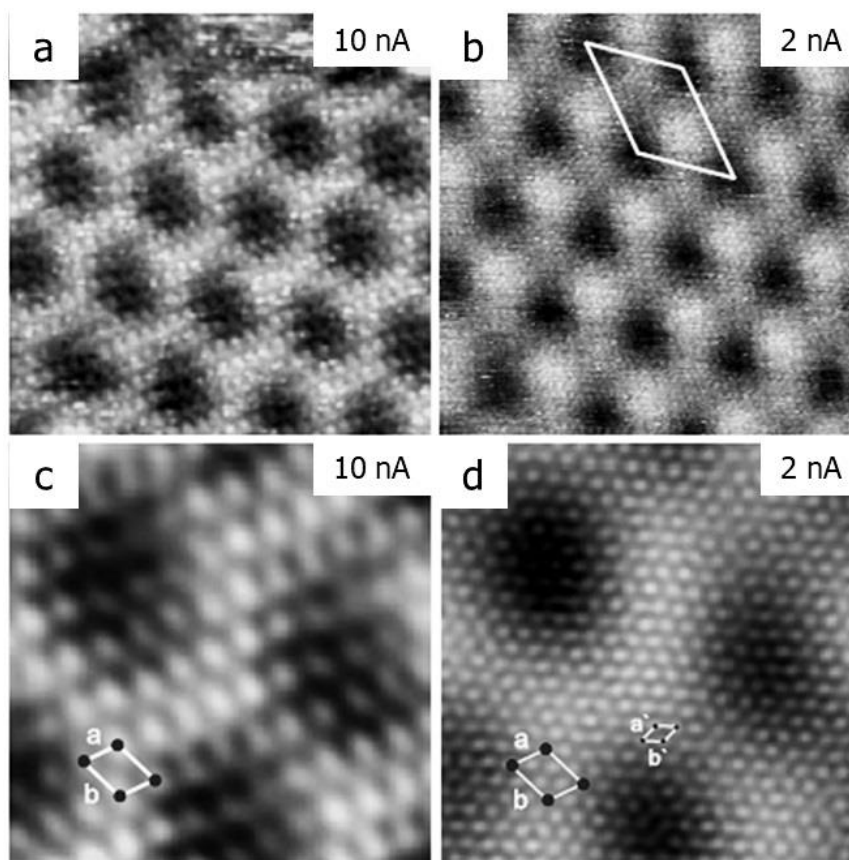


Figure 2.15: [60] Dependence of the sulfate-induced structure on Cu(111) as a function of tunneling conditions. The tunneling parameters of the STM images are: (a) image size $13.7 \text{ nm} \times 13.7 \text{ nm}$; bias voltage $U_b = -2 \text{ mV}$; tunneling current $I_t = 10 \text{ nA}$. (b) $13.7 \text{ nm} \times 13.7 \text{ nm}$; $U_b = -2 \text{ mV}$; $I_t = 2 \text{ nA}$. (c) $5.9 \text{ nm} \times 5.9 \text{ nm}$; $U_b = -2 \text{ mV}$; $I_t = 10 \text{ nA}$. (d) $5.9 \text{ nm} \times 5.9 \text{ nm}$; $U_b = -2 \text{ mV}$; $I_t = 2 \text{ nA}$. In all cases the electrode potential is $E = 100 \text{ mV}_{\text{RHE}}$, negative potential sweep.

It is important to emphasize, however, that not only the tunneling parameters but also the potential at the working electrode significantly influences these experiments. A slight variation in the working potential by approximately 30 mV rendered this approach ineffective, resulting in only the "usual" Moiré structure, as shown in Figure 2.6, being observable.

Hence, the Moiré pattern results from the superposition of two lattices that have a lattice mismatch Δa and are rotated by an angle α , leading to the formation of a

third superlattice, the Moiré. The characteristics of this Moiré superlattice are highly dependent on Δa and α , allowing for the determination of precise structural parameters beyond what can be observed from STM images alone. According to reference [60], by analyzing the relative positions of particles at equivalent sites imaged at the same height, it is possible to establish conditions for the coincidence between the expanded first copper layer and the unreconstructed second copper layer, considering the imaged anions as markers for the $\sqrt{3}$ and $\sqrt{7}$ positions on the expanded copper layer. As evident from Figure 2.6, travelling along a sulfate row in the $\sqrt{3}$ direction for ten steps and one step in the perpendicular direction is required to move between two depressions in the Moiré structure and reach the next closely packed sulfate row. The distance between two coincidence positions with the substrate, in terms of the expanded copper lattice constant $a_{unreconstr}$ can be derived:

$$d = \sqrt{(10\sqrt{3})^2 + \left(\frac{5}{2}\right)^2} a_{unreconstr} \quad (1)$$

The misalignment of the Moiré depressions from the $\sqrt{3}$ direction of the sulfate layer indicates that the lattice constants of the substrate and the adsorbate are not only different but also rotated relative to each other. The exact rotation angle and the stretching factor of the lattice constant are not known a priori. For the repetition of equivalent lattice sites at a distance d , a necessary condition is that d can also be expressed as a combination of the lattice vectors of the unreconstructed second copper layer:

$$d = \sqrt{(n\sqrt{3})^2 + (m)^2} \quad (2)$$

where n and m are both either integers or half-integers.

By equating d from (1) and (2), the rotation angle α between both lattices is:

$$\alpha = \arctan \frac{m}{n\sqrt{3}} - \arctan \frac{5/2}{10\sqrt{3}}$$

If $a_{reconstr.}$ is considered a freely adjustable parameter, an infinite number of n, m pairs can theoretically be found. However, reasonable restriction can be imposed that the ratio $a_{reconstr}/a_{unreconstr}$ should differ by only a few percent. Furthermore, the Moiré pattern's slight rotation relative to the $\sqrt{3}$ direction of the adsorbate, as previously described, imposes an additional constraint. This condition narrows down the possible solutions to just two distinct pairs for the equations (1) and (2):

$$m = \frac{1}{2}, \quad n = 10\frac{1}{2}, \quad \frac{a_{reconstr}}{a_{unreconstr}} = 1.040, \quad \alpha = -6.64^\circ$$

$$m = 3\frac{1}{2}, \quad n = 10\frac{1}{2}, \quad \frac{a_{reconstr}}{a_{unreconstr}} = 1.058, \quad \alpha = 2.68^\circ$$

By taking $a_{unreconstr} = 0.256$ nm for the second copper layer, Broekmann *et al.* obtained the following results:

For case one, $\sqrt{3}a_{reconstr} = 0.461$ nm and $\sqrt{7}a_{reconstr} = 0.704$ nm

For case two, $\sqrt{3}a_{reconstr} = 0.469$ nm and $\sqrt{7}a_{reconstr} = 0.717$ nm

In both scenarios, the calculated values fall within the error margins of those derived from direct STM image inspections. However, the values obtained in case (1) are closer to the measurements directly taken between the sulfate particles.

3.

Experimental Equipment and Theoretical Description

3.1 The Electric-Double Layer (EDL)

When a metallic solid and a liquid come into contact, microscopic changes take place at the electrode-electrolyte interface. The formation of an electric double-layer (EDL) at the solid-liquid interface is the basic notion for the description of interfacial science [66] [67]: this implies that the appropriate concentration of ions at the interface must be taken into account, in terms of atomistic and continuum theory. The fundamental model for the interpretation of the EDL accumulation has been developed more than 100 years ago by Hermann von Helmholtz (1879) [68]. The solid-liquid interface is the region where electronic conduction converts to ionic conduction: because of the transfer of the electrons sunk in the metal, the electrode exchanges charges with incoming ions as soon as the metal is wetted. Then, due to a secondary charge transfer mechanism, the electrode metal oxides and metal atoms leave the surface as charged cations and enter the solution. According to the simple Helmholtz model, the double-layer can be conceptualized as a molecular parallel-plate capacitor (hence the name electrical double-layer),

with one plate represented by the charges in the metal and the other plate by the ions, at a minimum distance in the solution. Thus, the capacitance assumes the value:

$$C_H = \frac{\epsilon_r \epsilon_0 A}{d}$$

where ϵ_r is the dielectric constant inside the EDL, ϵ_0 is the vacuum permittivity, A is the electrode surface area and d is the distance between the two plates. ϵ_r and d are thus the two parameters effectively describing the Helmholtz theory.

Since, in a metal, atoms are tightly bound, only the electrode surface contributes to the double-layer formation, which extends only into the electrolyte side and not into the metal side. The distance between the "plates" is on the order of molecular dimensions, hence the capacitance value is very high. Helmholtz was thus the first to interpret and recognize that a charged electrode will attract counterions from the electrolyte. This attraction results in a linear potential drop within the Helmholtz layer, as depicted in Figure 3.1, in which the double-layer charge is read as a function of the distance perpendicular to the surface [69] [70].

The Helmholtz model is applicable only to solutions with high concentration of electrolyte. In more diluted solutions, the transition goes on stepwise and the thickness of the double-layer increases. Gouy and Chapman refined the Helmholtz model by assuming a thermal diffusion of the ions distribution: in this theory, the thickness of the diffuse electric layer is correlated to the value of the distance from the metal plate at which the ions are able to run away from the bulk with a motion lead by thermal energy [71]. Nevertheless, the Gouy model shows notable deviations from experimental observations at high solution concentrations. To address this, Stern [72] proposed combining the Helmholtz and Gouy-Chapman models for a more accurate description of the double-layer (*see* Figure 3.1). This approach integrates the potential linear behavior with the exponential decreasing one at the EDL, at the interface between the electrode (the electronic conductor) and the electrolyte (the ionic conductor). It follows that the EDL is composed of

a compact layer in series with a diffuse layer (see the lowest part of Figure 3.1b): the Stern layer includes any adsorbed ions. Within the Gouy-Chapman-Stern theory, the Stern layer has the same physical weight as the Helmholtz layer, representing the closest outlook of the counter-ions to the metal surface. At high electrolyte concentrations, the Helmholtz layer predominantly contributes to the overall capacitance.

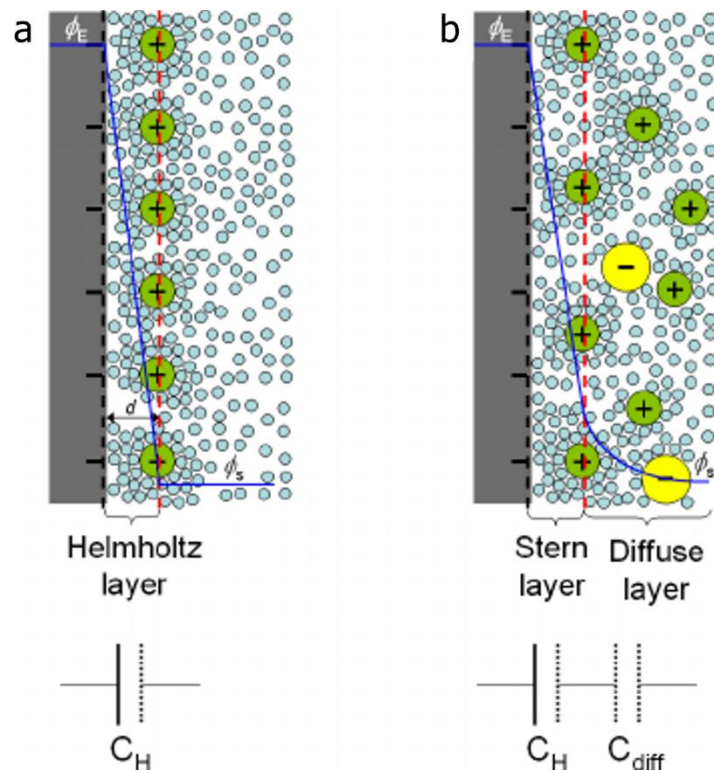


Figure 3.1: [70] a) The Helmholtz model and b) the Stern model of the electric double-layer and electric potential as function of the distance from the metallic electrode. In the picture, Φ_E is the surface potential and Φ_s is the potential at the Stern layer. The Stern model combines the Helmholtz theory (potential linear behavior) with the Gouy-Chapman theory (potential exponential decreasing behavior). In both models, the Helmholtz double-layer can be schematized in terms of capacitance C_H , with the two plates represented respectively by the charges in the metal (the left one) and by the ions in the electrolyte (the right one).

The electric potential distribution in the diffuse layer of the Stern model follows the Poisson-Boltzmann equation, for electrolytes with monovalent ions [70]:

$$\nabla(\varepsilon_r \varepsilon_0 \nabla \Phi) = 2e c_\infty \sinh\left(\frac{e\Phi}{k_B T}\right)$$

where ε_r is the dielectric constant inside the EDL, ε_0 is the vacuum permittivity, Φ is the electric potential, e the electron charge, c_∞ the bulk electrolyte concentration, k_B the Boltzmann constant and T the absolute temperature.

Starting from the electric potential distribution and solving the Poisson-Boltzmann equation, the capacitance of the diffuse layer is represented by [70]:

$$C_{diff} = \left(\frac{\varepsilon_r \varepsilon_0 A}{\lambda_D}\right) \cosh\left(\frac{e\Phi_{diff}}{2k_B T}\right)$$

where Φ_{diff} is the potential drop across the diffuse layer. For monovalent electrolytes, the characteristic Debye length λ_D is measured as:

$$\lambda_D = \left(\frac{\varepsilon_r \varepsilon_0 k_B T}{2e^2 c_\infty}\right)^{\frac{1}{2}}$$

The Stern theory still has limitations and there have been numerous attempts to refine it, giving consideration to many critical factors, namely *i*) the ability to adsorb or desorb substances at the EDL, *ii*) the non-linear property of the EDL, *iii*) the fact that the electrode is schematized as a perfect conductor, *iv*) the surface charge as continuous and uniform and *v*) that ions are considered to be perfect point charges (without considering their finite sizes), giving rise to ideal electrostatic interaction processes. On the contrary, it is now well-known that the mere presence of the aqueous electrolyte combined with the hydrogen layer leads to significant charge rearrangements within the further-up layers. Still, ion-ion interactions are neglected. A further limitation is given by ε_r , the dielectric

constant of the solvent in the diffuse layer, usually supposed as that of the bulk electrolyte. In addition, like the inclusion of the diffuse layer on the electrolyte side to the Helmholtz (or Stern) layer at the interface, a space charge layer on the electrode side can expand into the bulk of the electrode [73]. This effect is minimal in metallic electrodes due to the very short Debye screening length in metals. However, it cannot be ignored in semiconductors, thereby resulting in a system of three capacitors in series. In this work, we have employed a copper metallic electrode, so the model is fully valid.

In spite of these restrictions, this model remains reasonable in dilute electrolytes and for low potential drops across the diffuse layer ($k_B T/e \approx 25$ mV at room temperature).

3.2 STM (Scanning Tunneling Microscope) Basic Working Principle

The STM (Scanning Tunneling Microscope), that was developed in 1981 by Gerd Binnig and Heinrich Rohrer (Nobel prize 1986), is an instrument that utilizes a sharp, electrically conductive probe that scans just above the surface of an electrically conductive sample, for imaging at the atomic level [74] [75] [76]. The operating principle of STM relies on electron tunneling between the conductive probe and the sample: when the tip is sufficiently close to the sample (at a distance of about 1 nm or less), an electrical current moves (or tunnels) between the tip and the sample, provided that the two objects have different electric potentials, creating a measurable current (*see* Figure 3.2). The bias voltage between the tip and the sample is less than the work functions¹ [11] [77] of the tip and the sample. Depending on the bias voltage, electrons tunnel from the tip to the sample or, conversely, from the sample to the tip. The typical tunneling current required is around 1 nA and it is regulated by a feedback loop continuously adjusting the tip

¹“work function” \equiv The work function is defined as the minimum energy required to remove an electron from a material at 0 K.

height [78] [79] [80]. By this way, it was possible for the first time the real space analysis and the direct determination in three dimensions of surface structures. For rough surfaces, in the “slow imaging mode”, the tunneling current is kept constant (≈ 1 nA). This results in a topographic image of the sample surface, that represents the tip height as it moves across the surface, done by vertically (z) moving the probe at each (x, y) data point until a “setpoint” current is reached. If the setpoint value is set too negatively, the system will behave as though the tip is in contact with the sample, even when it is not. Because of this, the tip will fail to accurately map the surface topography, potentially resulting in a completely flat image. Adjusting the setpoint to a more positive value increases the force exerted by the tip on the sample. However, applying too much force can lead to excessive wear on the tip and might even damage the tip or the sample. The ideal setpoint value, which varies depending on the sample and probe, should apply just enough force to the tip to accurately trace the surface topography without exerting unnecessary pressure. The constant current method is most common in STM. Conversely, in the “fast imaging mode”, the tip scans along a plane while the current varies: this creates an image that maps the variation in the tunneling current [79].

Electrons have both wave and particle-like properties, as described by quantum mechanics; the tunneling phenomenon arises from the wave-like behavior of electrons. When two conductors are in close proximity, their electron wavefunctions overlap. With a small, applied voltage, electrons can traverse the gap between the probe, ideally ending in a single atom, and the sample. This movement of electrons is referred to as tunneling and the gap can be of air, vacuum or liquid. For the vacuum possibility and, in particular, ultra-high vacuum UHV environment, three parameters influence the tunneling current: the density of states of the tip $\rho_t(E)$, the local density of states of the sample $\rho_s(E)$, at the position of the tip, and the “barrier penetration factor” $T(E, eV)$ [81].

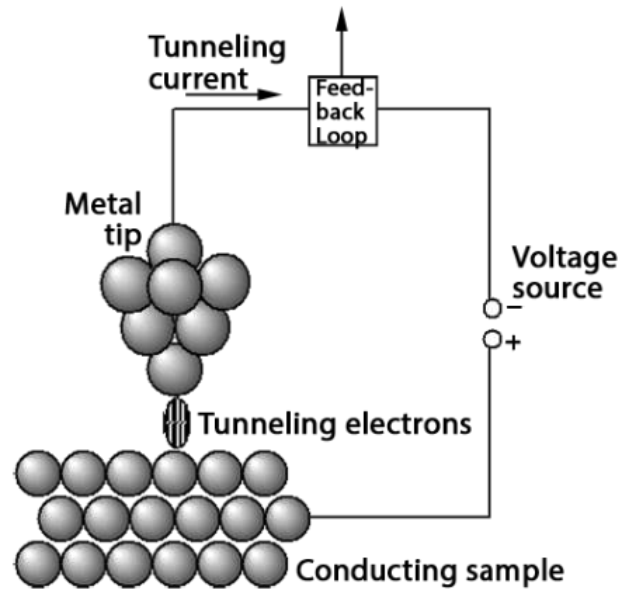


Figure 3.2: [82] STM feedback loop and tunneling effect scheme. When electrons move through the tip and the sample, the feedback loop regularly tracks the resulting tunneling current, to translate this useful information into STM images. For rough surfaces, the feedback loop constantly makes adjustments to the tip to maintain a constant current; for flat surfaces, the feedback loop can be switched off to have a constant height image, while varying the tunneling current.

An extensive graphical report of the quantum tunneling is illustrated in Figure 3.3. Imagine two metal electrodes separated by an insulating layer of thickness L . When the electrodes are at the same potential, the system reaches thermodynamic equilibrium, and their Fermi levels align, as shown in Figure 3.3a. Conversely, if the electrodes have different potentials, current can flow between them, as depicted in the energy diagram of the electrodes with an applied bias energy (eV), in Figure 3.3b. All the current in the system is assumed to be tunneling current. The width of the potential barrier for electrons at the Fermi level is given by:

$$\delta_z = z_2 - z_1.$$

The height of the potential barrier is indicated by Φ_z .

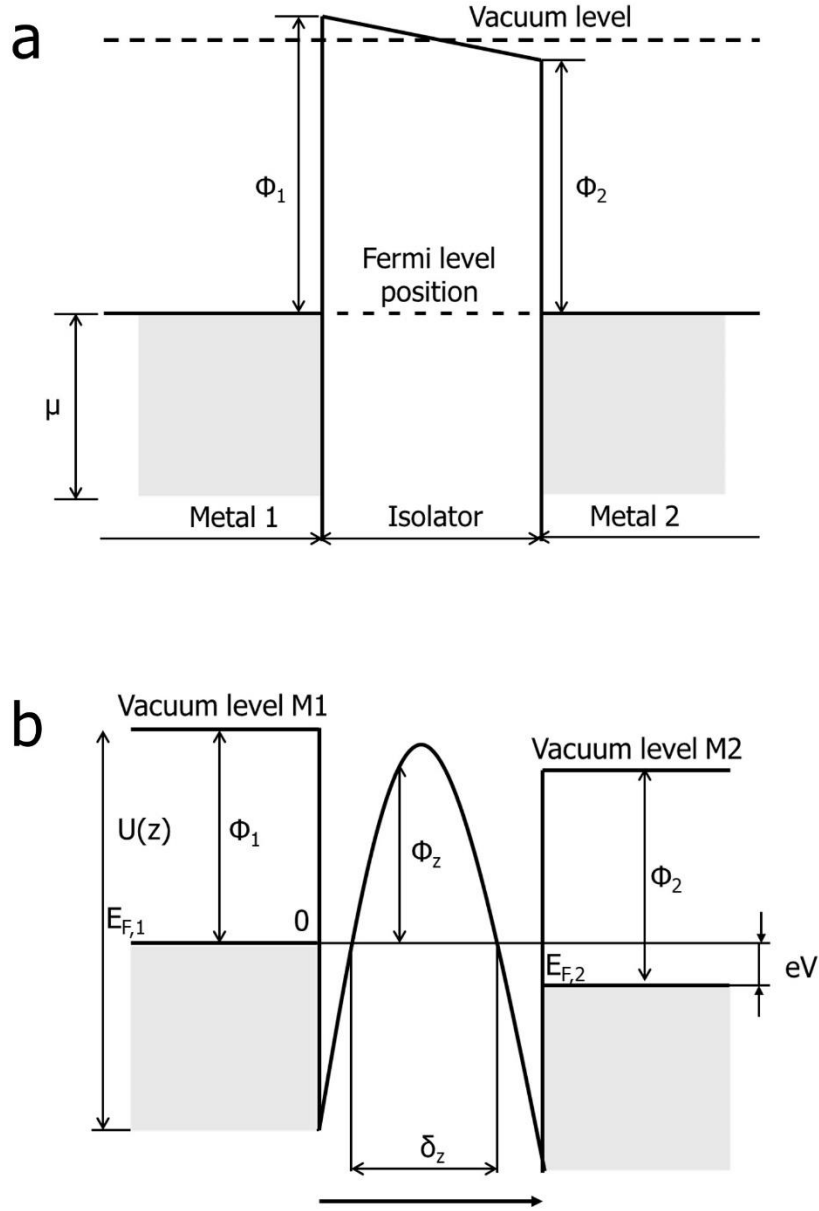


Figure 3.3: a) Metal-Isolator-Metal schematic representation of the system in equilibrium. b) Metal-Isolator-Metal schematic representation of the system with an arbitrary shape potential barrier; positive potential is applied to the right metal.

Coming back to the detailed STM tunneling current, the expression that evidences its proportionality to the above-mentioned factors is:

$$I \propto \int_0^{eV} \rho_s(E) \rho_t(eV - E) T(E, eV) dE$$

The “barrier penetration factor” or “transition factor” is defined as [79]:

$$T(E, eV) = \exp(-2d\kappa)$$

where d is the tip-sample distance. Defining Φ the average work function, as [79]:

$$\Phi = \frac{(\Phi_{tip} + \Phi_{sample})}{2} \approx 4eV$$

and V the external bias voltage, κ will be outlined, neglecting dependence on the electron’s wavevector, as [79]:

$$\kappa = \left(\frac{2m}{\hbar^2}\right)^{\frac{1}{2}} \left(\Phi - E + \frac{eV}{2}\right)^{\frac{1}{2}}$$

where m is the mass of the electron, e is the charge of the electron and \hbar is the reduced Plank constant, defined as:

$$\hbar = 1.054571817 \times 10^{-34} Js.$$

Therefore, supposing, as stated before, the work function Φ to have a value of $\approx 4eV$, the current results to have a strong dependence on the tip-sample distance (exponential decay): when the gap increases by 1\AA , the current will decrease by an order of magnitude. Electrons with energies near the highest lying Fermi level have the greatest transmission probability, although tunneling can occur for all electrons within the energy range between the two Fermi levels.

Going deeper in the STM theory, the tunneling current is given to first order in Bardeen’s formalism by [83]:

$$I = \frac{2\pi e}{\hbar} \sum_{\mu, \nu} f(E_\mu) [1 - f(E_\nu + eV)] |M_{\mu\nu}|^2 \delta(E_\mu - E_\nu)$$

where $f(E)$ is the Fermi function, V is the applied voltage, $M_{\mu\nu}$ is the tunneling matrix element between states Φ_μ (of the tip) and Φ_ν (of the sample) and E_μ is the energy of state of the tip in the absence of tunneling.

For room temperature or below and for small voltage, the above equation turns in [81]:

$$I = \frac{2\pi}{\hbar} e^2 V \sum_{\mu, \nu} |M_{\mu\nu}|^2 \delta(E_\nu - E_F) \delta(E_\mu - E_F)$$

The expression can be further simplified if you consider the limiting case of replacing the tip by a point probe, to obtain the maximum possible resolution. By this way, Φ_μ does not appear in the matrix element, which will be directly proportional to the amplitude of the sample Φ_ν at the position \vec{r}_0 of the probe [81]:

$$I \propto \sum_{\nu} |\Phi_\nu(\vec{r}_0)|^2 \delta(E_\nu - E_F)$$

The term on the right refers to the surface local density of states (LDOS) at the Fermi level (E_F), which corresponds to the charge density from states at energy E_F . Therefore, the tunneling current is directly proportional to the surface LDOS at the location of the point probe. The microscope image displays a contour map of constant surface LDOS.

Looking at a more realistic configuration, you need to solve $M_{\mu\nu}$. Bardeen found that [83]:

$$M_{\mu\nu} = \frac{\hbar^2}{2m} \int d\vec{S} \cdot (\Phi_\mu^* \vec{\nabla} \Phi_\nu - \Phi_\nu \vec{\nabla} \Phi_\mu^*)$$

where the expression inside the parentheses represents the current operator and the integration is performed over any surface that is completely within the vacuum (barrier) region that separates the two sides.

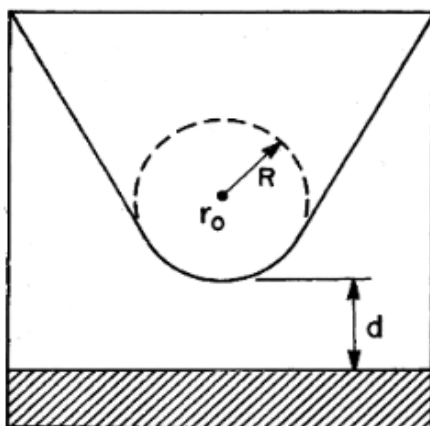


Figure 3.4: [81] Tip geometry scheme: it is assumed locally of spherical shape, in the point of nearest approach to the surface (at a distance d). \vec{r}_0 is the center of curvature of the tip. R is the local radius of curvature about the center located at \vec{r}_0 .

At this point, by calculating Φ_v , one can get Φ_μ , considering the microscopic tip, whose structure is actually unknown, as a locally spherical potential well at its closest point to the surface, as depicted in Figure 3.4.

3.3 Electrochemical Tunneling

Taking up the description of the tunneling process reported above, the reader is reminded that tunneling describes the movement of electrons (or other light charge carriers) across a nanometer-sized gap, a molecule, or even an insulating layer between two electrodes. When a bias voltage (V_{bias}) is applied between the two electrodes, negatively charged electrons are more likely to move towards the positively biased electrode, resulting in a detectable tunneling current (I). This current depends exponentially on the gap size (denoted as “ s ” (Å) in the formula below), which explains the high spatial resolution of STM, the applied voltage

V_{bias} and the electronic structure of the medium in the gap (*see* the electron band structure of the two conductors (ϕ , *i.e.*, the effective tunneling barrier (eV)) *in the formula below*) [14].

$$I_t = I_0 \frac{V_{\text{bias}}}{s} e^{-k\sqrt{\phi_b s}}$$

k is a constant. Consequently, the electrode junction can be represented by a transmission function that characterizes the probability of electrons traversing the gap from one electrode to the other, summarized over all energy levels. Therefore, the more accessible the energy levels in the junction and the better their electronic coupling to the electrodes, the higher the current across the junction [84].

Thus, tunneling is not limited to any specific state of matter and can occur through thin insulating (solid) films, vacuum, air, and even in solution environments [85]. The EC-STM signal is acquired by scanning a tip across a conductive sample with an electrolyte filling the tunneling gap in between. To prevent chemical reactions, the tip is insulated, often with a layer of wax [86]. When a voltage is applied between two electrodes in liquid environment, a measurable tunneling current is produced, which is extremely sensitive to the gap size, the applied voltage, and the medium within the gap. This phenomenon presents exciting possibilities for using tunneling currents as a precise tool to investigate fundamental interfacial processes and to grow a new class of sensor devices with unique capabilities, examine chemical reactions at the single molecular level or even to analyze the composition of biopolymers like DNA, RNA, or proteins [84] [87]. Today, STM is routinely used in various solution environments, including aqueous electrolytes, organic solvents, and ionic liquids [88]. In 1931, Gurney recognized the importance of quantum mechanical tunneling in electrochemical reactions at metal electrodes and his work represents the first application of quantum mechanics to an electrochemical problem [89]: he focused emphasis on the interpretation of quantum mechanics and on the physical processes lying in electrolysis which underpin some of the most elementary phenomena.

3.4 Evolution of Electrochemical STM Application Over the Years

Since the first (1981) successful STM experiments by Binnig and Rohrer, where they integrated the vacuum tunneling effect with a piezoelectric driven system to create a scanning tunneling microscope, the technique rapidly developed in an efficient way for surface and interface analysis [75] [78]. Initially, STM was used to study the solid/gas interface and was primarily operated in ultrahigh vacuum (UHV). Then, it was adjusted for use in air on Pt and Au electrodes, after electrochemical treatment, due to its ability to perform *in-situ* and in real-time imaging with a highly variable resolution range [90]. Sonnenfeld and Hansma demonstrated that STM could produce highly resolved images in aqueous electrolyte solutions [91]. The early STM experiments used a simple two-electrode electrical circuit, consisting only of the sample and the tip, which did not guarantee defined potential control. Siegenthaler was the first to introduce a reference electrode in the electrochemical STM cell, enabling independent control of the potentials of the sample (working electrode 1) and tip (working electrode 2) using a bipotentiostat [92]. Itaya *et al.* then extended this circuit by adding a counter electrode, creating a four-electrode setup that allowed measurement of faradaic currents and enabled EC-STM to be used as an operando microscopic technique during electrochemical experiments [93]. Since these early developments, numerous scientists have made pioneering contributions to the advancement of EC-STM. Bard's group studied the dissolution of copper (Cu) single crystal electrodes in aqueous chloride media, achieving atomic resolution to understand the reaction mechanism [94] [95]. Behm *et al.* attained atomic resolution on gold (Au) single crystals and on sub monolayer electrodeposits of Cu on gold's three low-index planes [96]. Ertl's group imaged adsorption/desorption phenomena on Pt single crystal [97] [98]. Kolb significantly contributed to the EC-STM initial steps toward atomic resolution, studying Cu cluster deposition on Au(111) electrodes, by transferring copper from the STM tip to the surface [99]. Magnussen developed a STM video system with enhanced time resolution, capturing 10-30 images per second [100]. Soriaga

imaged the dissolution of Pd single-crystal electrodes catalyzed by adsorbed iodine. Wandelt's group designed an EC-STM optimized for investigating potentiodynamic processes and used it to study, among others, sulfate adsorption on Cu(111), correlating anodic and cathodic peaks in cyclic voltammograms with sulfate adlayer adsorption and desorption [56] [65] [101].

Metal corrosion and anodic passive film formation for metals such as Nickel (Ni), Chromium (Cr), Aluminum (Al), Iron (Fe), Copper (Cu), and Cobalt (Co) have been extensively studied using EC-STM and EC-AFM and even some technologically significant bulk oxides, like TiO₂, which were previously only observed under UHV conditions, have also been analyzed with EC-STM [50].

Copper has played a crucial role in advancing society, particularly in the 20th century, where its electrical properties made it a key material in chip design for the computer and microelectronic industries, replacing aluminum in transistor systems [46] [50]. Understanding the passivation behavior and structure of copper's anodic oxide layer is vital. The formation of protective anodic oxides on Cu in aqueous electrolytes depends on pH, applied potential, and polarization time, aligning with thermodynamic predictions of the Pourbaix diagram. In acidic solutions (pH < 5), the dissolution of anodic oxides is too rapid to provide passivity. The composition of Cu oxide layers formed at higher pH levels has been studied using various electrochemical and surface analytical methods, including X-ray photoelectron spectroscopy (XPS), photoacoustic spectroscopy, ion scattering spectroscopy, *in-situ* Raman spectroscopy, and infrared spectroscopy [50].

3.5 AFM (Atomic Force Microscope) Basic Working Principle

Atomic Force Microscopy (AFM), first introduced in 1985 by G. Binnig, C.F. Quate, and Ch. Gerber, has revolutionized the field of surface characterization by enabling high-resolution imaging at the microscale, nanoscale, and even atomic scale. Unlike techniques such as STM, which rely on electrical current to probe

surfaces, AFM utilizes mechanical forces, making it capable of imaging both conductive and non-conductive materials. This capability is crucial for the broad range of scientific and engineering applications, particularly in materials science, nanotechnology, and biological research [102].

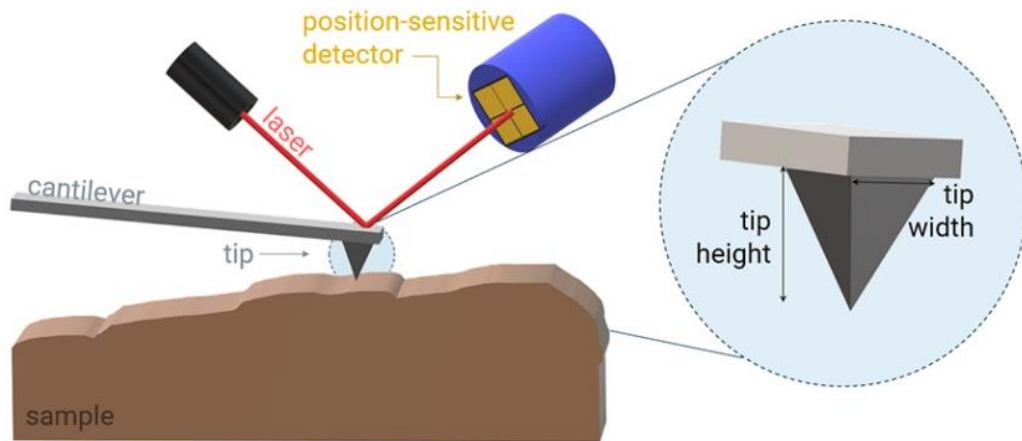


Figure 3.5: Atomic Force Microscopy basic working principle block. Reproduced from <https://www.bruker.com/en/products-and-solutions/microscopes/materials-afm/faq.html>.

Atomic force microscopy, with its ability to operate in contact and non-contact modes, is a critical tool for high-resolution surface analysis. Its flexibility in imaging both conductive and insulating materials, combined with its capability to function in various environments, makes it indispensable for advanced research in Physics Engineering and related fields.

An AFM system primarily consists of a microscope integrated with X/Y motion controls, a precision scanner, a sharp probe (tip), and a sensitive detection system. The heart of the AFM is the cantilever with a sharp tip at its free end, which interacts with the sample surface. The tip scans over the surface, and these interactions cause the cantilever to bend or deflect. A laser beam is focused on the back of the cantilever and reflects onto a four-quadrant photodiode detector. As the cantilever bends due to forces exerted by the sample surface, the movement of the laser spot on the detector is translated into an electrical signal measured in

volts, providing data about surface topography and properties (Figure 3.5) [103]. When the cantilever presses the tip against the sample, it bends instead of forcing the tip closer to the sample atoms. This bending serves as a reliable indicator of the surface topography. Additionally, during a typical scan, the cantilever twists in the direction of the scan as the tip encounters regions with varying friction and topography, while also deflecting vertically. The detector detects changes in the cantilever's twisting motion and outputs them as the lateral deflection (friction) signal, results that are plotted in the friction image (V) [104].

3.5.1 AFM Imaging Modes

AFM operates mainly in two force regimes: contact mode and non-contact (tapping) mode, each suited for different types of surface interactions and material characteristics.

In the contact mode, the tip remains in continuous contact with the sample surface, causing the cantilever to deflect according to the topography. There are two approaches within contact mode:

- **Constant Height Mode:** The scanner maintains a fixed height as it moves across the sample. This mode is sensitive to small changes in topography, ideal for atomically flat surfaces, but does not capture true topographical information.
- **Constant Force Mode:** The tip's height is dynamically adjusted using a feedback loop to maintain a constant force, ensuring detailed imaging even on rough surfaces. This mode provides accurate topographical data but may be limited by scanning speed and noise from the feedback circuit.

In non-contact mode, the cantilever oscillates at or near its resonant frequency, with the tip lightly tapping the sample surface. This reduces frictional forces and minimizes direct contact, making it suitable for imaging soft or delicate structures. In liquid environments, non-contact mode reduces the influence of

capillary and van der Waals forces, enhancing image quality and allowing the study of dynamic processes at solid-liquid interfaces. This mode is especially advantageous for imaging soft or organic materials, such as biological samples or thin films, as it minimizes the risk of mechanical damage and preserves the sample's integrity [105].

Non-contact mode offers several key advantages over contact mode, particularly for the analysis of soft or sensitive materials:

- 1) **Enhanced Resolution and Sensitivity:** by avoiding direct contact, non-contact AFM minimizes sample deformation, enabling the acquisition of high-resolution images. This mode also captures additional parameters such as oscillation amplitude, frequency, and phase shift, providing deeper insights into the sample's chemical and physical properties.
- 2) **Reduced Sample Damage:** the lower interaction forces in non-contact mode help prevent elastic or plastic deformation, preserving the natural morphology of the sample and allowing for accurate characterization of soft materials.
- 3) **Detection of Force Gradients:** non-contact mode can detect both forces and force gradients, making it sensitive to variations in surface composition and mechanical properties.

AFM is a versatile tool capable of performing in-situ imaging of samples in controlled environments, including liquid media. This capability is critical for studying processes at the solid-liquid interface, which is relevant in fields such as biophysics, electrochemistry, and materials science. However, AFM's sensitivity to environmental vibrations necessitates the use of anti-vibrational chambers to isolate the instrument from external disturbances, ensuring high-quality imaging.

In the present work, non-contact mode AFM is employed to study the anodic dissolution of Cu(111) surface in dilute 5 mM H₂SO₄ solution. This choice is based on the need to minimize the impact of tip-sample interactions on the sample's structural integrity, thereby accurately capturing the morphological evolution of the surface. Non-contact AFM allows the recording of both topographical data and chemical surface properties, making it a powerful method for comprehensive surface characterization.

3.5.2 Fundamentals of Atomic Force Microscope

The interaction between the AFM tip and the sample can be effectively described, to a first approximation, by the empirical Lennard-Jones potential, which models interatomic and intermolecular forces (*i.e.*, it describes the interaction between a pair of nonionic particles, such as atoms or molecules, that do not form ionic bonds). The Lennard-Jones (or 12-6) potential is mathematically represented by the following equation [106]:

$$V(r) = 4\epsilon \left[\left(\frac{\sigma}{r} \right)^{12} - \left(\frac{\sigma}{r} \right)^6 \right]$$

where:

- $V(r)$ is the potential energy as a function of the distance r between two particles,
- ϵ represents the depth of the potential well, indicating the strength of the interaction,
- σ is the distance at which the interparticle potential is zero, and
- r is the distance between the particles.

This potential describes both the repulsive forces (dominant at short distances) and the attractive forces (dominant at longer distances) between the AFM tip and the sample.

The repulsive term, $\left(\frac{\sigma}{r}\right)^{12}$, represents the repulsive force between particles. The repulsive interaction dominates when particles are very close to each other, primarily due to the Pauli exclusion principle, which prevents overlapping electron clouds. The r^{-12} dependence causes the repulsion to increase rapidly as the distance between particles decreases, ensuring that particles do not collapse into one another.

The attractive term, $\left(\frac{\sigma}{r}\right)^6$, accounts for the attractive van der Waals forces, which arise from induced dipole-dipole interactions. The attractive force becomes significant at larger distances, where the electron clouds of the particles begin to interact weakly. The r^{-6} dependence reflects the long-range nature of these attractive forces, which decrease more slowly with increasing distance compared to the repulsive forces [107].

The resulting force as a function of the tip-sample atomic distance, depicted in the picture below (Figure 3.6), exhibits distinct regions.

Therefore, the attractive region is dominated by the weak, long-range van der Waals interaction between dipoles, which follows a $\left(\frac{\sigma}{r}\right)^6$ law. On the other hand, the repulsive region is governed by a $\left(\frac{\sigma}{r}\right)^{12}$ term, which becomes significant at very short distances, typically below 1–2 Å (the length of a chemical bond). At short distances (when $r < \sigma$), the repulsive term dominates, resulting in a steep rise in potential energy, which effectively pushes the particles apart. At intermediate distances ($r \approx \sigma$), the attractive and repulsive forces balance each other out, and the potential reaches its minimum value $-\epsilon$, indicating the most stable configuration. At larger distances (when $r > \sigma$), the attractive term dominates, leading to a negative potential energy, which signifies that the particles attract each other but with diminishing strength as the distance increases.

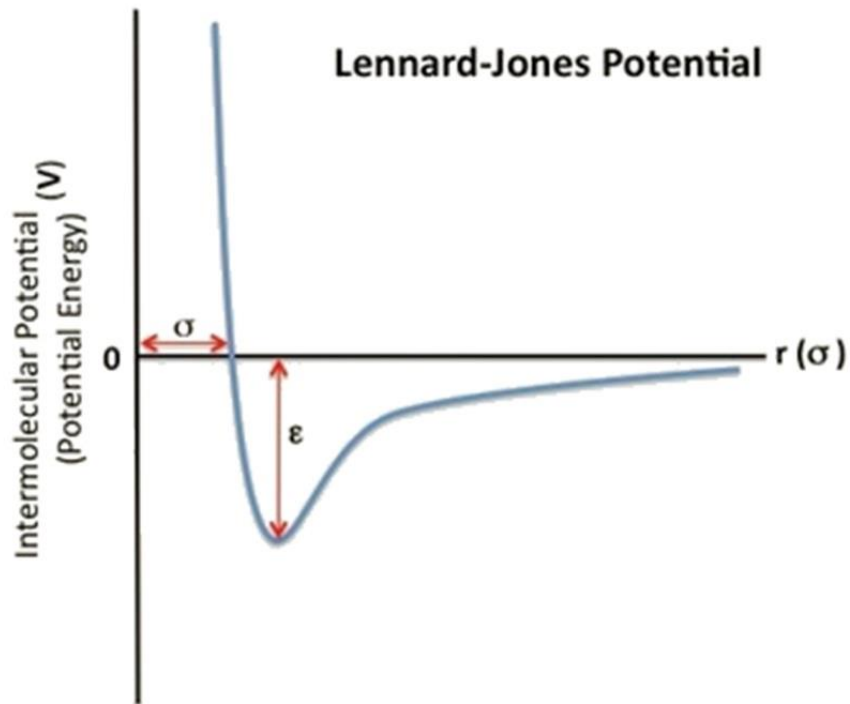


Figure 3.6: The LJ potential describes both the attraction and repulsion between non-ionic particles. The first part of the equation, $\left(\frac{\sigma}{r}\right)^{12}$ describes the repulsive forces between particles while the latter part of the equation, $\left(\frac{\sigma}{r}\right)^6$, refers to the attractive forces.

Anyway, a comprehensive description of the tip-sample interaction must also consider specific short-range forces, such as adhesion/contact forces and capillarity forces, that are not captured by the Lennard-Jones approximation. Adhesion/contact forces arise when two bodies come into contact and deform, with the degree of deformation dependent on the elastic properties of the materials involved. The analytical relationship between the applied force and the resulting deformation, expressed through the stress (σ) and strain (ϵ) tensors, can be modeled using various theoretical frameworks that incorporate surface energy contributions. Capillarity forces, on the other hand, are attractive forces generated by the liquid meniscus that forms between the tip

and sample under ambient conditions, due to the adsorption of a thin water layer on a hydrophilic surface [108, 109].

3.6 Electrochemistry

As mentioned in the introduction, although electrochemistry is deeply embedded in the "chemical sciences," numerous significant contributions have also originated from the "physics" community. One of the most notable early examples is Michael Faraday, after whom the electron transfer-induced current flow is named [110]. Electrochemistry stands for "electrically driven chemistry" and it involves applying a voltage across a solid-liquid interface (or, in general, a junction) to drive a reaction. From a physics perspective, this process can be interpreted in terms of single particle picture, to analyze the electrons motion [111]. Electrochemistry is a process operating far from equilibrium, so a wide range of reactions is not fully understood yet and this is true for tunneling reactions too [112]. Tunneling effect in electrochemistry involves all those reactions that are not chemisorption or physisorption (*i.e.*, they are not adiabatic) reactions onto the solid: electrons are exchanged between the electrolyte and the solid but they are not deposited on it or they are not bonded with the surface [113].

Therefore, understanding the electrochemical tunneling reactions from a physical point of view implicates concepts in the field of electrochemistry, often absent in solid-state systems. The system depicted in Figure 3.7a delineates a metal electrode in equilibrium state with a liquid medium. The electrode on the left, *i.e.* the metal, where the electrochemical reactions occur, is called the working electrode (WE), ideally composed of an inert metal such as gold (Au) [114]. The electrode placed in the liquid is known as the counter electrode (CE). To initiate an electrochemical reaction, a voltage source, like the battery shown in the upper part (not yet connected), is used. In the liquid (the ionic electrolyte), there are various ionic species present, depicted in white with "+" (positively charged supporting electrolyte ions) and "-" (negatively charged supporting electrolyte

ions) signs. These ions facilitate the potential drop necessary for driving electron transfer even if they do not participate in the electrochemical reaction by accepting or donating electrons. Really, the supporting electrolyte ions could be able to act as reactants, depending on the magnitude of the applied bias, that is, if their reactant energy levels lie outside the so-called “bias window”, *i.e.*, the electrolyte stability region and if sufficient high bias is applied. Ideally, the concentration of supporting electrolyte ions is much higher than that of the reactants being studied. The reactants are shown in red and blue, and they are the reduced and oxidized species, respectively. A reduced species gains electrons, so it has one more electron than an oxidized species. Even in equilibrium state, electron transfer occurs, but there is no net current flow because the rate of electron transfer from the electrode to the oxidized species (blue arrow in Figure 3.7a) is equal to the rate of electron transfer from the reduced species to the electrode (red arrow in Figure 3.7a).

In Figure 3.7b, a bias V is applied to the system: the negative potential is applied to the WE, causing electrons to accumulate on its surface and positive counter charges from supporting electrolyte ions to gather at the solid–liquid interface. This process often has an associated time constant due to the diffusion of supporting electrolyte ions, which will not be discussed here [115]. As a result, the negatively charged electrons on the metal electrode and the counterions in the solvent act like a capacitor, creating the electrostatic potential drop Φ shown in green in Figure 3.7b. The exact profile of this non-equilibrium potential drop Φ is exactly the complex double-layer, described in this elaborate in chapter 3.1. Therefore, the primary purpose of Φ is to alter the electrochemical potential of the metal with respect to that of the liquid, allowing preferential electron transfer to or from a reactant species.

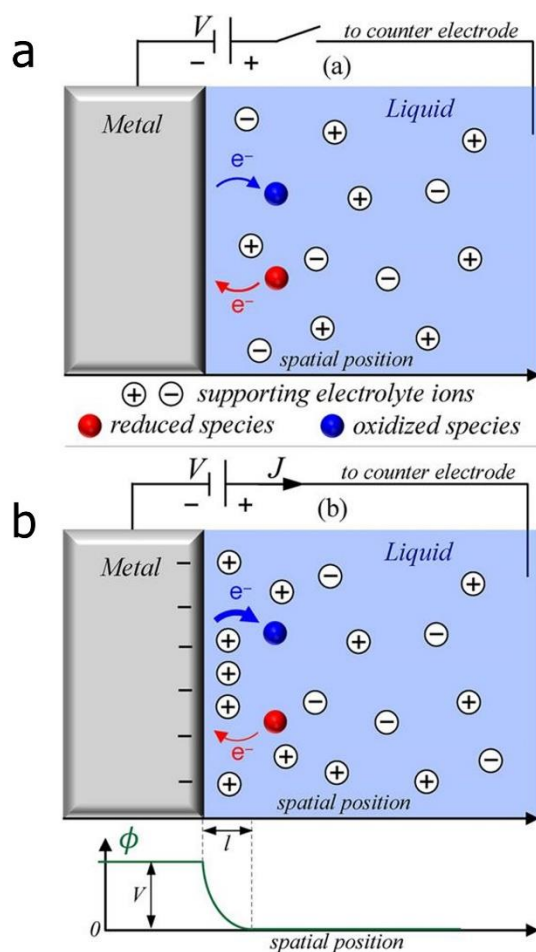


Figure 3.7: [111] (a) Scheme of the solid-liquid interface in equilibrium in a tunneling electrochemical reaction. The metal is in equilibrium with the liquid that contains reactant species, the blue ones are oxidized (i.e., once oxidized, they “receive” an electron from the electrode and are therefore reduced) and the red ones are reduced (i.e., once reduced, they “donate” an electron to the electrode and are therefore oxidized), and supporting electrolyte ions. (b) Scheme of the solid-liquid interface when a bias V is applied in a tunneling electrochemical reaction. As a consequence of the applied bias, a non-equilibrium potential drop Φ develops at the solid-liquid interface: this creates a capacitive-like junction between the charges on the metal and the counter charges of the supporting electrolyte ions. Positive current flow (J) occurs when there is a greater transfer of electrons from the working electrode (WE) on the left to the oxidized species in the solution; than J occurs from the reduced species in the solution back to the WE. Under equilibrium conditions, as in (a) case, these two transfer processes are balanced.

Regarding the configuration in Figure 3.7*b*, the accumulation of negative charge on the working electrode increases its electrochemical potential relative to that of the liquid, favoring electron transfer from the electrode to the blue oxidized species in the liquid (*see* the blue arrow in Figure 3.7*b*) and lowering the rate of electron transfer from reduced species in the liquid to the electrode (indicated by the red arrow in Figure 3.7*b*). The net electron transfer from the working electrode to reactants in the solvent is defined as J , and is a positive current flow if considered, as in Figure 3.7*b*, in the opposite direction to electron flow [111]. Just referring to Figure 3.7*b*, the applied bias is depicted as dropping across the WE solid–liquid interface due to the assumption that the surface area of the WE is much smaller than that of the CE. This concept can be explained as follows: the solid–liquid interaction at each electrode can be initially approximated as parallel plate capacitors of the form:

$$C_{WE} = \frac{\epsilon_r \epsilon_0 S_{WE}}{l}, C_{CE} = \frac{\epsilon_r \epsilon_0 S_{CE}}{l}$$

where ϵ_r is the liquid relative permittivity, ϵ_0 is the vacuum permittivity, S_{WE} is the surface area of the working electrode, S_{CE} is the surface area of the counter electrode and l is the thickness of the double layer in the liquid region. These two parallel plate capacitors are in series for the external bias, so the total capacitance is:

$$C = \frac{C_{WE} C_{CE}}{C_{WE} + C_{CE}} \approx C_{WE}, S_{CE} \gg S_{WE}$$

Thus, it is reasonable to assume that most of the voltage drop occurs across the working electrode. This approximation, however, may not always be practical or realistic [111]. Consequently, the use of reference electrodes (RE) has been adopted. A RE is an electrode with a well-fixed electrochemical potential against which the offset of the electrochemical potential of the WE are measured.

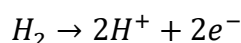
Therefore, by employing a RE, the WE potential drop changes under an external bias V can be estimated.

It still holds true that we are interested in potential drop changes at the WE and this is the reason why it is assumed to happen entirely at the WE in Figure 3.7 [111].

3.6.1 The Standard Hydrogen Electrode (SHE)

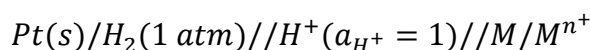
The absolute single electrode potential is an intrinsic property of a metal, and while it cannot be directly measured, it can be assessed in relation to a reference electrode such as the standard hydrogen electrode (SHE). The SHE consists of a platinum electrode immersed in a solution where hydrogen ions are present at unit activity, which can be achieved by using a 1 mol/L HCl solution. To establish unit hydrogen gas activity, hydrogen gas is passed over the platinum electrode at 1 atmospheric pressure.

The SHE operates based on the reaction [116]:



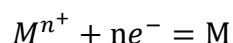
By definition, the SHE has an electrode potential of zero at all temperatures, and this forms the foundation for comparing the electrode potentials of other metals. The electrode potential of a given metal can be determined by measuring the electromotive force (emf) of the cell, *i.e.*, the maximum potential difference between two electrodes of a cell, formed by the metal and the SHE. The overall cell emf represents the electrode potential of the metal half-cell in reference to the SHE.

The general representation of such a cell is:

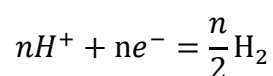


The metal ion concentration M^{n+} affects the cell potential, which is why its activity must be specified. The corresponding half-reactions are:

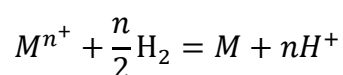
- for the metal electrode,



- for the standard hydrogen electrode,



The full cell reaction, derived from the difference between these two half-reactions, is:



The emf of the overall cell can be expressed as:

$$E_{cell} = E_{M^{n+}/M} - E_{H^{+}/H_2}^0$$

Since E_{H^{+}/H_2}^0 is defined as zero, the equation simplifies to:

$$E_{cell} = E_{M^{n+}/M}$$

Thus, the emf of the cell directly corresponds to the electrode potential of the metal half-cell with respect to the standard hydrogen electrode. This method provides a reliable and universally accepted way to measure and compare the electrode potentials of different metals.

3.7 Understanding Vicinal Surfaces: Key Notions About Their Formation, Structure and Fundamental Principles

Vicinal surfaces, characterized by their step-terrace structure, play a pivotal role in surface science, catalysis, and electrochemistry. Derived from single crystals, these surfaces are slightly miscut from low-index planes, introducing periodic steps of one or more atomic layers in height and terraces, *i.e.*, regions of atomic flatness, that enhance surface reactivity and catalytic activity.

Mathematically, vicinal surfaces are often indexed using the Miller indices that describe the orientation of the terraces. The terraces themselves correspond to a low-index plane, such as (100), (110), or (111), while the presence of steps gives the surface a higher Miller index, reflecting the deviation from the perfectly flat plane. The vicinal surface is then described as having steps that deviate from the ideal plane by a small angle (usually less than a few degrees), leading to a periodic arrangement of atomic rows. At atomic steps on vicinal surface, the surface atoms are less coordinated compared to atoms in the bulk or flat surface terraces, rendering them more chemically reactive. This property is especially relevant in fields such as heterogeneous catalysis and surface electrochemistry, where the surface structure heavily influences reaction mechanisms and kinetics.

Particularly, vicinal surfaces are typically derived from single crystals, which are crystalline materials with a continuous and unbroken lattice structure throughout the sample. To create a vicinal surface, a single crystal is cut at a small angle relative to one of its low-index planes, resulting in a surface that is not perfectly aligned with the atomic planes. This process introduces atomic steps between the terraces, each of which corresponds to the underlying low-index plane of the crystal. The starting point is to select a high-quality single crystal, which has a homogeneous and defect-free lattice. For most studies, metals such as copper (Cu), platinum (Pt), or silicon (Si) are used due to their well-understood surface structures. The crystal is oriented with respect to a specific crystallographic axis using techniques such as X-ray diffraction (XRD) or Laue back reflection. Once

oriented, the crystal is cut at a small angle near (“vicinal”, *i.e.*, typically between 1° and 10°) to a low-index facet, such as (111), (100), or (110). The cutting angle determines the density of steps on the surface: a small angle results in wider terraces and fewer steps, while a larger angle produces narrower terraces and a higher step density.

After cutting, the surface of the crystal is typically polished to remove any roughness or imperfections introduced during the cutting process. Following this, the crystal is annealed (heated) in a controlled environment, usually in ultra-high vacuum, to allow surface atoms to rearrange into a more ordered structure. During annealing, atoms on the vicinal surface migrate to reduce surface energy, which often results in the straightening and alignment of the steps [26].

The periodicity of the terraces and steps can be calculated based on the miscut angle (θ) and the lattice constant, *i.e.*, the distance between atomic layers in the crystal, (a) of the crystal [117]. The terrace width (L) can be approximated using simple geometric relationships:

$$L = \frac{a}{\tan \theta}$$

where a is the lattice constant, or the height of steps, and θ is the miscut, or vicinal, angle, *i.e.*, the angle between the surface of the vicinal plane and the flat reference plane, like (111), (100), or (110) [118].

In idealized models, vicinal surfaces are composed of perfectly straight steps and uniform terraces. However, real vicinal surfaces often deviate from this ideal structure due to various factors, such as surface energy minimization, faceting, or interactions with adsorbates. For example, faceting occurs when the surface rearranges into a structure with higher steps and wider terraces, maintaining an overall crystallographic angle but lowering the surface energy.

In Figure 3.8, the schematic representation of a vicinal surface emphasizes the key parameters: the miscut angle, step height, and terrace width [119].

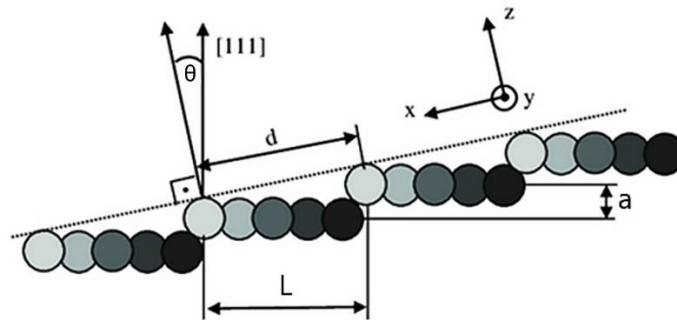


Figure 3.8: Schematic representation of a vicinal surface. The figure highlights the miscut angle θ , the step height a , and the terrace width L .

Vicinal surfaces are typically characterized using a combination of techniques that provide information about the atomic structure, step density, and surface morphology. Common techniques include STM, that provides atomic-scale images of stepped surfaces, revealing the arrangement of atoms along the terraces and steps, as well as LEED or AFM, which is employed to measure the topography of vicinal surfaces. Due to their unique stepped morphology, vicinal surfaces such as platinum and palladium have several important applications, for instance, in catalytic converters, where the steps and kinks enhance the dissociation of molecules like CO and NO. In the field of epitaxial growth, vicinal surfaces are crucial for the growth of thin films and nanostructures (e.g. 1D nanowires). The presence of steps on vicinal surfaces provides nucleation sites for adatoms, which promotes layer-by-layer growth in molecular beam epitaxy (MBE). By controlling the miscut angle and terrace width, researchers can tune the growth mode and properties of the deposited films. Vicinal surfaces are also important in surface reconstructions and phase transitions: the presence of steps influences how surfaces reconstruct when exposed to external stimuli, such as changes in temperature, pressure, or chemical environment. Still, studies of vicinal surfaces have provided insights into surface diffusion, step-flow dynamics, and the interaction between adsorbates and surfaces [26].

4.

Experimental Methods

4.1 Electrochemical Scanning Probe Microscope (EC-SPM)

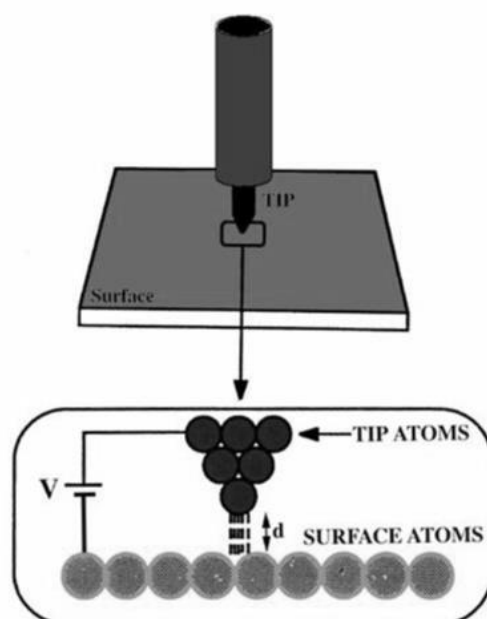


Figure 4.1: SPM scheme of the tip-sample interaction [120].

A commercial Keysight Technologies 5500 Scanning Probe Microscope (SPM) has been used for this experimental work. It can provide atomic-scale resolution in many areas of research, such as electrochemistry, life science, materials science

as well as nanolithography, biotechnology and electrical characterization. The SPM instrument has a sharp probe, as illustrated in Figure 4.1, with radius of curvature of the order of nanometer, probing the sample immediately beneath (\approx nanometers deep) the surface and immediately above (\approx tens of nanometers high) the surface. Then, the tip-surface interactions are mapped [120] [121]. The sharpness of the probe tip is essential to the SPM high resolution. Two primary configurations were utilized: Electrochemical Scanning Tunneling Microscope (EC-STM) and Electrochemical Atomic Force Microscope (AFM).

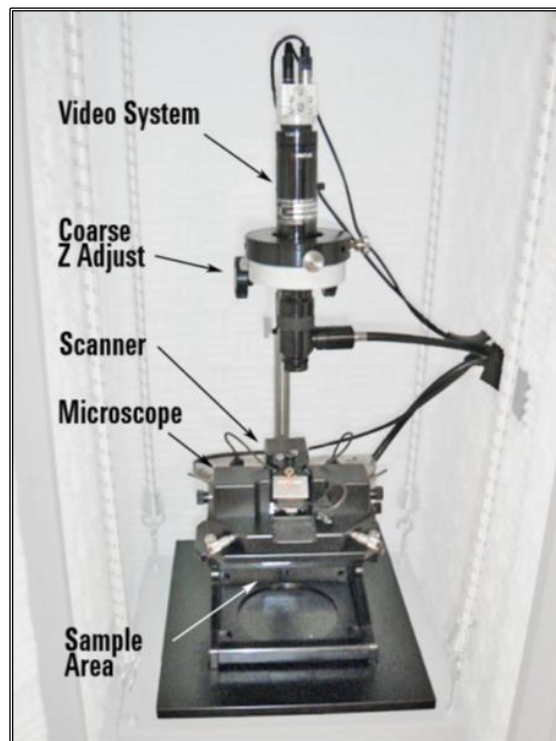


Figure 4.2: Major components of the Keysight Technologies 5500 SPM. [120].

The major Keysight 5500 SPM components (*see* Figure 4.2) are:

- the video system that, for AFM imaging, allows the alignment of the laser on the probe tip, when highly reflective samples are analyzed, and eases the choice of the region to analyze;

- the microscope, including magnetic base for supporting the sample plate, electronic connections, manual X/Y positioning micrometers and coarse z-axis motors;
- the scanner, in which the tip is located, that is composed of piezo-ceramic materials, elongating or contracting as an electric field is applied to them (Figure 4.3 below);

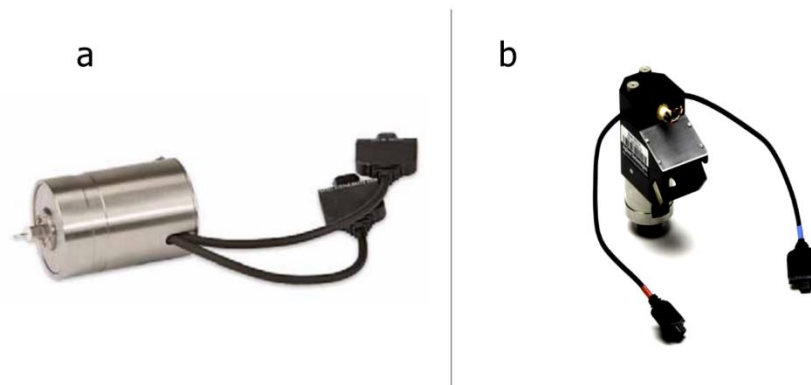


Figure 4.3: (a) STM scanner and (b) AFM scanner [120]. The probe is attached to the piezoelectric scanner (indifferently, (a) or (b)), in which piezoelectric materials are incorporated. Piezoelectric materials have a permanent dipole moment across their unit cell, being able to change their length in an applied field if the dipoles are oriented. If a negative voltage is applied, the piezoelectric material retracts; conversely, if a positive voltage is applied, the scanner will extend. Most SPM use a piezoelectric scan tube technology, which combines (and that's the case) independent piezos to control the three directions x , y and z . By this way, it is possible to have a z motion, if all the three directions are involved, or a x - y scanning (raster) motion.

- the nose assembly, *i.e.* the part of the scanner that retains the cantilever (a spring clip secures the probe in the right position) and enables its motion;

- the photodiode detector, mounted in the scanner, that senses the laser's movement between its four quadrants, receiving the SUM signal, the lateral LFM signal (*i.e.*, the friction) and, for AFM imaging, the reflection of the laser spot off the back of the cantilever;
- the head electronic box, that takes the signal from the detector, setting out the SUM signal (*i.e.*, the sum of the four quadrants of the detector) and the deflection signal and the friction signal, for the AFM imaging;
- the vibration isolation chamber, that isolates the whole microscope (*see* Figure 4.2) from vibrations and acoustic noise and, indeed, takes care of the imaging quality.



Figure 4.4: Keysight's sample plates. The sample plate in the left part is used in the air: the sample can be fixed by the two clamps to get stability and ease of use. The sample plate in the right part of the picture serves the purpose for the electrochemical measurements: the sample is mounted in the Teflon EC-cell and a Viton O-ring is used to seal and to avoid any leakage of liquid. The WE, RE and CE are inserted in the three outlets in the white holder. By using magnetic suspension, loading becomes more convenient and mechanical drift is eliminated [120].

The instrument is located on a platform and held up by four cords, through four adjustable bungee mounts. The 5500 SPM employs Keysight's PicoView as an imaging and analysis software package to enables full control over all scanning parameters, even in more sophisticated experiments. Topography images are the most frequently produced in SPM, where the Z-axis represents the sample surface

height at specific X/Y coordinates. These measurements are generally calibrated using height standards. Consequently, as long as the systems are properly calibrated and operated, and the data is correctly interpreted, topography images can provide reliable quantitative information.

The two sample holders that have answered the purpose of this research are represented in Figure 4.4 and described in the relative caption.

STM tips are wire tips made from Platinum-Iridium (Pt-Ir) or Tungsten (W) wires, prepared by cutting or electrochemical etching. AFM cantilevers, constructed from silicon or silicon nitride, incorporate a sharp tip at their free end. The selection of probe and cantilever parameters, such as tip geometry, spring constant, and resonance frequencies, depends on the specific application, sample's surface type, imaging environment, and the kind of image being produced. Tip geometries include tetrahedral, pyramidal, and conical shapes, with tip sharpness - defined by the radius of curvature and sidewall angles - playing a crucial role in determining the probe's resolution. Cantilever shapes can be triangular (V-shaped) or rectangular (beam-shaped), with spring constants ranging from very soft (fractions of N/m) to very stiff (tens or hundreds of N/m). Additionally, cantilevers used in specific imaging modes may be coated with materials that are reflective, conductive, or magnetic.

4.2 Tip Preparation

STM tungsten (W) tips were primarily used for this research work, even if some attempts of measurement were performed also with Platinum/Iridium (Pt/Ir) tips. Pt/Ir tips are stable throughout all the potential interval for a given electrolyte, up to high potential values. On the contrary, W tips can dissolve when too high potentials are employed. Nonetheless, the hardness of W tips makes them a great choice for STM characterization: because tungsten is exceptionally hard, these tips stay intact even when they make gentle contact with softer sample surfaces. Furthermore, tungsten maintains its stability over a wide pH range. The Pt/Ir tips

are instead easier to deform, due to their lower hardness, making their preparation procedure more difficult too.

W tips are prepared by electrochemical etching by hand; therefore, it is useful to prepare multiple tips before conducting an experiment. The tips are electrochemically etched in a 3M NaOH solution; the diameter of the wire is of 0.25 mm and about 2 cm in length of wire are required for each tip. The method consists in passing the tungsten wire through a droplet of the alkaline NaOH solution, held in suspension in a gold ring; a potential of around 2 V is applied until the region of the wire that is immersed separates, after consumption, creating a very sharp tip (*see* Figure 4.5).

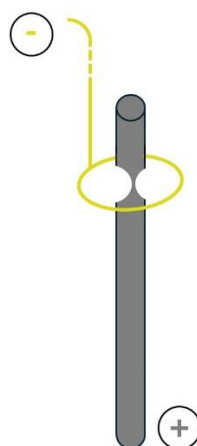


Figure 4.5: Tips electrochemical etching procedure scheme. The W wire is moved through a droplet of NaOH solution, suspended in a gold ring at an applied potential of 2 V: at that position, the wire is consumed, and a sharp tip is produced.

Pt/Ir tips are prepared by manually cutting a wire with a thickness of 0.25 mm, using a nipper: the inclination of the cutting angle is the crucial point maximizing the efficiency (i.e., the sharpness) of the tip. For this reason, also in this case, it can be useful and, really, it is often required to prepare a lot of tips before doing an experiment.

Tips are rinsed with high purity water in either case. Then, tips must be insulated by shielding, except for the very end, with wax, to avoid the background electrochemical current flowing through them, once immersed inside the liquid

electrolyte for running the experiment. The tunneling current should be less than 1 nA, and ideally below 0.1 nA. The solid wax is melted by using a heating device in which a little platinum plate is connected to a power supply: the plate has a linear slot thick enough to let the tip pass through it. A very little quantity of solid wax is put on the platinum plate; once the wax is melted after reaching the specific temperature by heating the device, the tip is guided through the linear slot – so, through the drop of melted wax, utilizing a mechanical system that enables manual movement along the three axes x, y, and z. The operator's manual dexterity is crucial for this step: the efficiency of the tip and of the tunneling effect depends on the extent of its coating, which should ideally be sufficient to cover the entire portion immersed in the liquid solution, except for the very tip itself at the end.

4.3 Solution Preparation (H₂SO₄ 5mM)

Sulfuric acid (H₂SO₄) is a highly hazardous inorganic compound, characterized as a colorless, viscous liquid that is fully soluble in water at any concentration. Its structural formula is reported in Figure 4.6: it can be noticed from the picture that sulfuric acid is a sulfur oxoacid that consists of two oxo- groups and two hydroxy-groups, linked to a central sulfur atom with covalent bonds. It is extremely corrosive and toxic. Exposure to sulfuric acid can occur through inhalation, ingestion and skin contact: for this reason, a protective equipment is always required when handling this acid. Sulfuric acid, or hydrogen sulfate, is highly reactive, dissolving most metals. As a concentrated acid, it oxidizes, dehydrates, or sulfonates most organic compounds; it reacts aggressively with alcohol and water, releasing heat in the process. When diluted with water, it can react with most metals to generate flammable hydrogen gas, posing a potential explosion hazard.

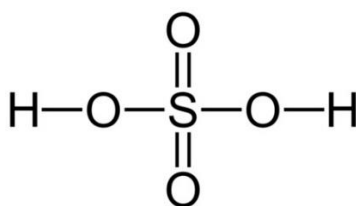
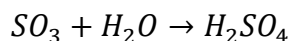
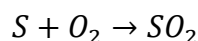


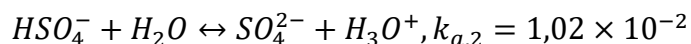
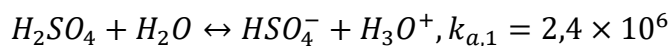
Figure 4.6: Structural Formula of Sulfuric Acid.

Sulfuric acid is synthesized from elemental sulfur via a three-step process, even if there are various specific and detailed methods for its commercial production. In general, the three reactions for the manufacturing of sulfuric acid are:



First, sulfur reacts with dry air in an exothermic reaction (combustion of elemental sulfur) producing sulfur dioxide: the product must be cooled to prevent the reaction from reversing. Then, sulfuric acid is produced by sulfur trioxide.

The solution utilized for these experiments was prepared by diluting with deionized water a commercial ultrapure solution of sulfuric acid to obtain the required concentration of H_2SO_4 5mM. The dilution can be schematized as follows:



where HSO_4^- is the bisulfate anion, SO_4^{2-} is the sulfate anion, $k_{a,1}$ (strong acid) and $k_{a,2}$ are the acid dissociation constants. Although sulfuric acid is a strong

diprotic acid, only the first proton fully dissociates in solution while the second proton has an acid dissociation constant $k_{a,2}$ of $1,02 \times 10^{-2}$.

Therefore, given that sulfuric acid is a strong acid for its first dissociation but not for the second one, the pH of a 5mM sulfuric acid solution can be calculated like this, for the first dissociation:



For the second dissociation:



$$[H_3O^+] = [HSO_4^-] = 0,005 \text{ M}$$

	HSO_4^-	H_2O	\leftrightarrow	SO_4^{2-}	H_3O^+
<i>initial state</i>	0,005			//	0,005
<i>variation</i>	-x			+x	+x
<i>at equilibrium</i>	0,005 - x			x	0,005 + x

$$k_{a,2} = 1,02 \times 10^{-2} = \frac{[H_3O^+][SO_4^{2-}]}{[HSO_4^-]} = \frac{(0,005 + x)(x)}{(0,005 - x)}$$

Then, by solving the quadratic equation:

$$x^2 + 0,0152x - 5,1 \times 10^{-5} = 0$$

You obtain:

$$x = 2,83 \times 10^{-3}$$

And:

$$[H_3O^+] = 7,83 \times 10^{-3} M$$

$$pH = -\log[H_3O^+] = 2,1$$

4.4 Surface Preparation

Flat Cu(111) and its vicinal Cu(221) and Cu(21 21 16) single crystals surfaces were acquired from Surface Preparation Laboratory (SPL). The sample dimensions must be compatible with the STM stage of the instrument being used: square shaped samples, with dimensions of 10 mm × 10 mm × 1 mm. Achieving atomically resolved EC-STM images requires meticulous surface preparation. Extended surface terraces on Cu(111), Cu(221) and Cu(21 21 16) can be obtained through a preparation process that involves mechanical polishing, followed by electropolishing in phosphoric acid.

4.4.1 Electropolishing

The three surfaces were prepared using an initial electropolishing process in orthophosphoric acid (H₃PO₄(aq.)) 70% by weight to remove the thick natural oxide layer from the surface. According to established methods, the entire samples were immersed in the orthophosphoric acid solution, parallel to the solution surface, with the oriented surface pointing upwards. The counter electrode was a platinum wire shaped into a spiral and a potential of 2 V was applied for 3 minutes. During the process, care was taken to ensure that a thin liquid film consistently covered the copper surface to protect it. After the electropolishing, the surfaces were rinsed with the same solution used in subsequent experiments (5 mM H₂SO₄). However, this rough electropolishing

procedure could potentially impact the quality of the crystal surface, especially for vicinal surfaces, which are more reactive. The high reactivity of these surfaces makes them more susceptible to imperfections or alterations during the electropolishing process, potentially affecting the overall surface quality needed for precise imaging and analysis (*see the Experimental Results and Discussion section* for further details).

4.5 Setting the Experiment

In this research, a custom modification was implemented to the commercial Keysight EC-SPM, enabling seamless transitions between scanning tunneling microscopy and atomic force microscopy without altering the sample environment. This flexibility is crucial and became necessary for monitoring the entire corrosion process of the Cu(111) surface in 5 mM H₂SO₄, allowing the use of both EC-STM and EC-AFM within the same experiment. Throughout the experiments, the sample remained immersed in a sulfuric acid electrolyte and connected to a potentiostat to maintain a constant potential. When switching to STM mode, the system was reconfigured to a bi-potentiostat setup.

To integrate the EC-STM and EC-AFM systems, a specialized electrochemical cell was developed. While EC-STM measurements only require the insulated tungsten tip to be immersed in the electrolyte, in-situ AFM imaging demands the use of a more substantial head to accommodate the cantilever chip. The custom-designed cell, illustrated in the picture below (Figure 4.7), was positioned directly over the copper sample and secured in place with a polydimethylsiloxane (PDMS) O-ring to prevent any electrolyte leakage.

AFM measurements were performed in non-contact mode, with the tip's resonance frequency measured at approximately 300 kHz in air and 140 kHz within the electrolyte.

Following the previously outlined procedure, the STM tips, fabricated from tungsten wire, were prepared via electrochemical etching and subsequently coated

with a wax layer for insulation. Only the very apex of the tip was unexposed, enabling the detection of the tunneling current necessary for imaging.

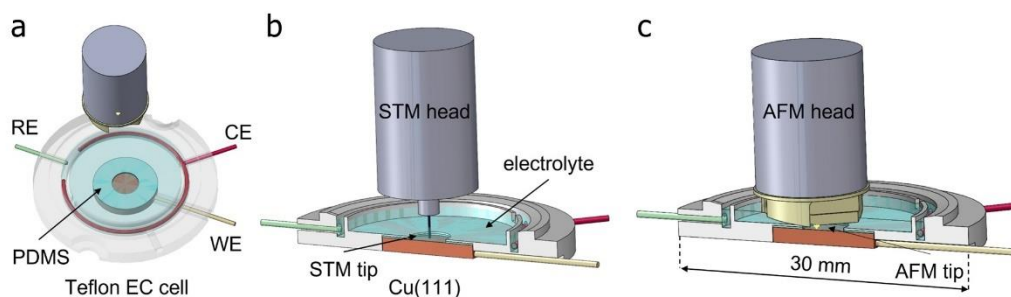


Figure 4.7: [122] a) Sketch of the custom EC cell used for the experiments. b) Image of the STM head immersed in the electrolyte. c) Being more massive, the AFM head requires a wide cell in view of properly purging the tip inside the electrolyte. In particular, our cell can be filled with about 2 ml of electrolyte. Only the working electrode [Cu(111)] is indicated in panels b) and c).

In the electrochemical setup, a platinum wire coiled around the cell served as the counter electrode (CE), and the copper sample functioned as the working electrode (WE) [123]. A second platinum wire was employed as a quasi-reference electrode: since the platinum wire does not utilize a redox couple to stabilize the reference potential, it is termed a quasi-reference electrode (Pt-QRef.). Despite this, in acidic environments, the Pt wire remains stable within a few millivolts and exhibits a shift of +800 mV relative to the SHE. In particular, the Pt-QRef is an advanced electrode designed for electrochemical analysis to deliver a stable reference potential. Unlike conventional reference electrodes, such as silver/silver chloride (Ag/AgCl) or saturated calomel electrodes (SCE), which are optimized for precise potential measurements across various solutions, the Pt-QRef is employed where a robust, solid-state reference is beneficial. Typically made from high-purity platinum, the Pt-QRef utilizes the metal's inherent stability and electrochemical neutrality to provide a nearly constant potential relative to the solution. This characteristic is especially valuable in challenging experimental environments where traditional reference electrodes may face issues like

contamination or potential drift. Due to its durability and minimal upkeep needs, the Pt-QRef is increasingly favored in both industrial and research settings where dependability and long-term performance are essential. Its uses include sensor calibration and electrochemical reaction investigations, highlighting its adaptability and effectiveness in contemporary electrochemical applications [124].

The electrolyte solution was prepared by diluting sulfuric acid with deionized Type 1 water, resulting in a final pH of 2. Prior to conducting the experiments, the electrolyte was purified by bubbling high-purity argon through it for several hours to eliminate dissolved oxygen.

The copper sample is secured from the outside using an O-ring against a hole in the bottom of the electrochemical flow cell, ensuring that only the prepared top surface contacts the electrolyte: this proper seal avoids any leakage. The surface area exposed to the electrolyte is circular-shaped, with a diameter of 0.5 cm². It is essential to wear disposable nitrile, powder-free gloves when handling the cell to avoid contamination. The electrodes should never be touched with any metal objects or unclean tools to prevent damage or interference with the measurements. Before introducing the electrolyte into the cell, the electrodes must be connected to their respective terminals, and the connections should be tested using an ohmmeter to ensure proper contact and functionality. This step verifies that the system is correctly assembled and ready for the introduction of the electrolyte for subsequent experiments.

Before starting an experiment, it is crucial to ensure that the electrochemical cell, typically made of PTFE plastic, along with the platinum electrodes, O-rings, and any related glassware such as small beakers for electrolyte solution and water, are thoroughly cleaned. Proper cleaning is essential to avoid contamination that could affect the accuracy of the results. The cleaning process generally involves rinsing the components with deionized water to remove any residues, followed by cleaning with an appropriate solvent, such as isopropanol or ethanol, to dissolve any organic impurities. Weakly, specific cleaning procedures may be required for the cells and the electrodes, like rinsing with acid solutions – particularly, Piranha

solution, depending on the nature of the experiment. Once cleaned, all components should be dried in a clean, dust-free environment before being reassembled for the experiment.

4.6 Data Analysis

The output of an STM measurement consists of a series of topographic profiles generated by scanning the tunneling tip over the sample along a defined scan line. Each profile corresponds to a specific length, and by applying a color gradient to the vertical z scale, the elevation at every point along the scan can be represented by a corresponding color. If the tip accurately traces the surface roughness, the resulting false-color image, created from these topographic profiles, provides a visual representation of the surface morphology. This visualization is facilitated by specialized software.

The software controlling the STM performs an initial image processing step, producing raw images that are considered unfiltered and represent the original data captured by the instrument. Additional software tools are available to enhance these images by applying specific filters. This software provides a large number of data processing functions, including all the standard statistical characterization, levelling and data correction, filtering or grain marking functions. These filters can increase contrast, reduce noise, and correct bad data points. In this study, Gwyddion, a modular program for SPM data visualization and analysis, was utilized for image processing and enhancement.

4.7 Calibration of the Microscope

The STM instrumentation requires manual calibration to ensure it produces dimensionally accurate images. The operation relies on the deformation of a piezoelectric tube, which moves the scanning tip across the sample surface. The

conductive sectors of the piezoelectric tube are polarized by the STM unit, resulting in the tube's deformation and subsequent displacement of the tip. The STM unit is designed to record images of a fixed, predetermined size by applying discrete voltage values to the conductive sectors, which causes specific deformations in the piezoelectric tube.

To achieve accurate measurements, it is crucial to calibrate the system using known substrates. This calibration process involves determining the conversion factor that accurately translates the applied voltage into the corresponding nanometer displacement of the scanner. By analyzing the response on a substrate with known dimensions, the correct conversion value can be assigned, allowing the STM to measure and image surfaces with precise scale accuracy.

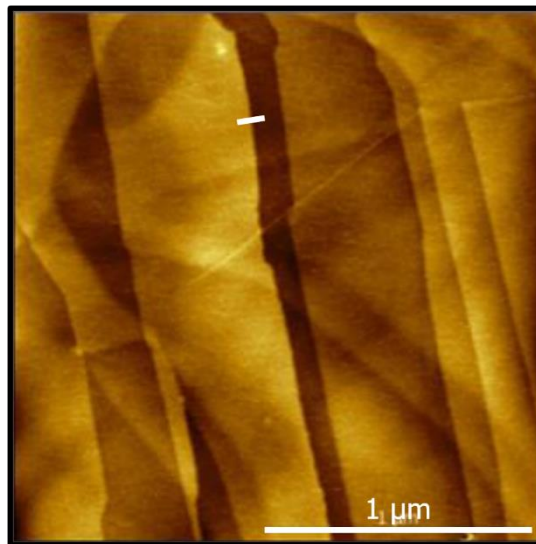


Figure 4.8: AFM topographic image of HOPG, $2 \times 2 \mu\text{m}^2$. The white line indicates an extrapolated profile (see below) [121].

To estimate these uncertainties, a comparison was made between the measurement of a step on Highly Oriented Pyrolytic Graphite and an ideal HOPG reference step. As depicted in Figure 4.8, the steps are clearly visible, with the white line indicating the extrapolated profile, which is further detailed in Figure 4.9.

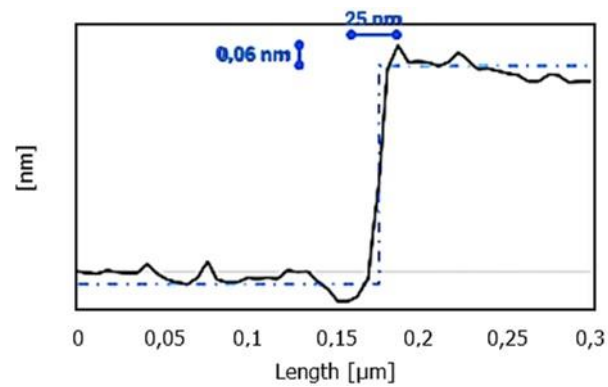


Figure 4.9: Step profile of Figure 4.8 [121].

The step shown in Figure 4.8 corresponds to a bi-atomic step, as its height is approximately twice the interlayer distance between graphite sheets (0.335 nm). From the image, the vertical uncertainty of the AFM tip is estimated to be around 0.06 nm. Regarding the horizontal resolution, it is estimated to be approximately 25 nm. This value is primarily attributed to the physical dimensions of the AFM (or STM) tip, particularly its radius of curvature, which typically ranges from 10 to 20 nanometers.

5.

Experimental Results and Discussion

5.1 Initiating the Experiment: Setup and Initial Procedures

Before attaching the sample holder to the microscope head, the sample surface needs to undergo electrochemical reduction. This process begins by adding the H₂SO₄ 5 mM electrolyte to the cell and performing a cathodic sweep, reducing the sample down to hydrogen evolution potential (≈ -0.6 V vs SHE) and then sweeping up to about -0.3 V vs SHE, as shown in Figure 5.1. This step removes any air-formed oxide film present on the sample surface. The process is repeated until the cathodic peak, which corresponds to the reduction of the oxide, is no longer visible in the voltammogram (*see* curve b in Figure 5.1). Once the oxide reduction is complete, it's helpful to run a few additional cyclic voltammograms to identify the positions of the peaks and ensure the system is operating correctly. Any irregularities, such as a tilted baseline, could indicate a contaminated electrolyte. Once the surface is fully reduced, and the cathodic peak is no longer observed in the voltammogram, the sample plate can be attached to the microscope. During this process, care should be taken not to touch the electrodes,

as this could alter the sample's potential and cause unwanted reactions. The mounting should be adjusted so that the STM tip is located near the center of the electrochemical cell for optimal measurements.

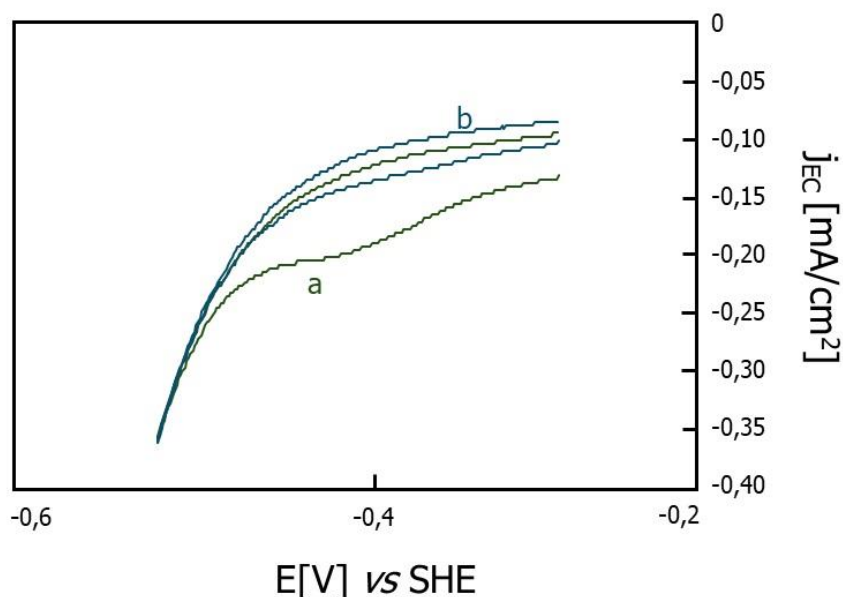


Figure 5.1: The voltammogram for the reduction of the air-formed oxide film on Cu(111) in 5 mM H_2SO_4 presents distinct features across the two sweeps. The potential was swept initially (a) from ≈ -0.3 to ≈ -0.6 V and then back up to -0.3 V again. The scan rate is 20 mV/s. The potential values are reported with respect to SHE. In the b curve, after repeating the cycle, the oxide has been fully reduced: the reduction peak is now diminished or shifted, as most of the oxide was removed during the first sweep. The process can be performed again until no significant reduction peak is visible anymore, suggesting that the oxide film is entirely reduced. The current response is now stable, confirming the surface has been cleaned of air-formed oxides.

Please be aware that, although, as previously mentioned, the reference electrode used in this work is the platinum quasi-reference electrode, the potential values have been converted to the SHE for more direct comparison with the literature.

When beginning electrochemical scanning tunneling microscopy imaging, one can choose to start at a potential where the copper surface is bare, typically below -0.3 V vs SHE, or at a potential where the surface is covered by the sulfate

adlayer, within the range of -0.2 V to $(-0.1 \div 0.1$ V) vs SHE. Since sulfate adsorption onto the Cu(111) surface is completely reversible, the specific starting potential is flexible. However, it is important to note that terraces on the Cu(111) surface tend to be more well-defined before any adsorption–desorption cycles occur. Repeated cycling can potentially alter terrace edges or surface features, leading to less ideal imaging conditions. Therefore, initiating imaging before the surface has undergone significant adsorption–desorption cycles is preferable to obtain clearer, more stable images of the terraces.

A well-prepared STM tip exhibits a very low tunneling current over a broad range of tip potentials. This low current is indicative of minimal faradaic current contributions and good insulation of the tip, ensuring high-quality imaging and reducing interference during electrochemical experiments. Maintaining this small current across a wide potential range is crucial for obtaining stable and reliable data during EC-STM imaging. The set point current is the imposed tunnelling current and is normally set to values of around 1.0 nA, or less, depending on the conditions. For these experiments, the tip voltage was set to have a tip bias (bias = $E_{\text{tip}} - E_{\text{sample}}$) around 0.3V (positive or negative bias at 0.3 V, both perform very well).

5.2 Cu(111) in Dilute H₂SO₄ Solution

As already mentioned in the introduction, the thermodynamic behavior of copper when immersed in a dilute sulfuric acid solution is well-represented by the Pourbaix diagram, which maps out the stable phases of copper as a function of pH and potential. In the context of this study, where the Cu(111) surface is exposed to a 5 mM sulfuric acid solution (pH = 2), the corresponding potential region that can be analyzed by STM measurements is located within the immunity zone, beneath the onset of anodic dissolution (*please, go back to Figure 2.1*).

In the picture below (Figure 5.2), the characteristic cyclic voltammogram for Cu(111) in this environment reveals the electrochemical responses of copper, with

a scan rate of 20 mV/s, bounded by two key processes: hydrogen evolution at negative potentials and copper oxidation at positive potentials. Notably, the cathodic peak, labeled in the picture as B = Cu_{red}, corresponds to the re-deposition of copper during the reverse scan.

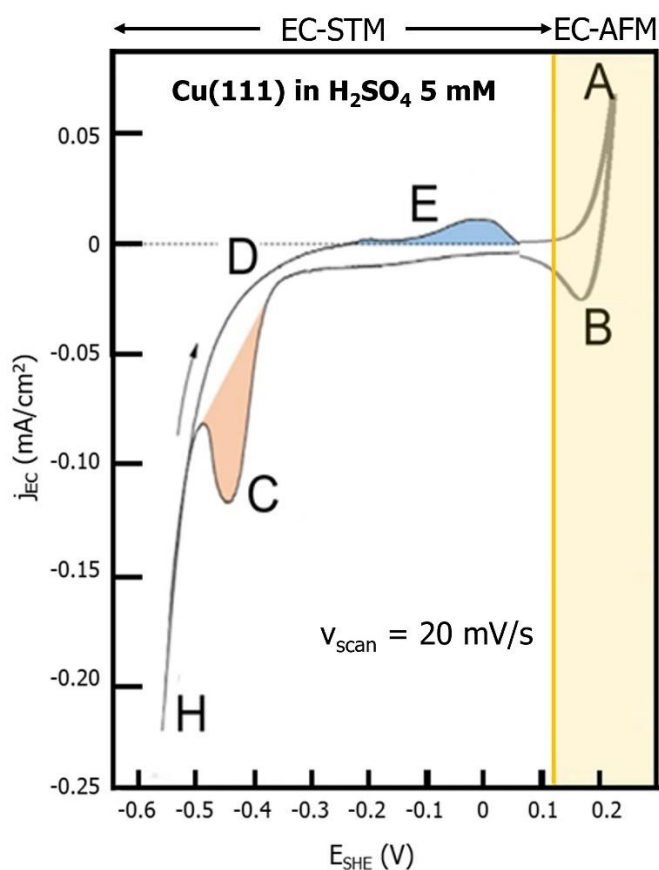


Figure 5.2: CV of Cu(111) immersed in sulfuric acid electrolyte (pH = 2). A: anodic corrosion; B: copper re-deposition; C: sulfate desorption; D–H: hydrogen evolution; E: sulfate adsorption regime. Scan rate is 20 mV/s. Note, in the upper part of the image, the indication of the area that is analyzed by STM, and of the less stable anodic region that can be explored by AFM.

Sulfate anion adsorption and desorption play a significant role in the electrochemical behavior of Cu(111), with adsorption occurring between -0.1 V and $+0.1$ V (vs SHE). The voltammogram shows distinct anodic and cathodic peaks related to sulfate adsorption and desorption (E and C letters in Figure 5.2,

respectively). The colored areas are proportional to the exchanged anodic (blue) and cathodic (pink) charges, for which we estimate $Q_a = 14 \mu\text{C}$ and $Q_c = 37 \mu\text{C}$, respectively. According to the literature, the cathodic desorption peak is unexpectedly [in fact, for a reversible process like this, the anodic and the cathodic peaks in a CV should have equal areas] much larger than the anodic adsorption peak in the CV, a discrepancy previously attributed to the Frumkin effect, as already mentioned in the introductory section. As long as sulfate anions desorb, their negative charge draws H_3O^+ ions toward the surface, lowering the overpotential required for hydrogen evolution. This results in an enhanced hydrogen evolution current that overlaps with the sulfate desorption process. Once sulfate is fully desorbed, hydrogen evolution continues on the bare Cu(111) surface. Recent studies suggest that the excessive cathodic current may also be linked to the formation of a surface copper hydride (CuH) phase, as observed through electrochemical mass spectrometry and advanced spectroscopic techniques. These methods support the hypothesis that the high desorption peak results from a combination of the sulfate desorption current and a sulfate-induced hydrogen evolution current. In rare instances, these two current components can even be distinguished separately within the cyclic voltammogram [60] [62] [125] [126].

The Pourbaix diagram highlights copper's stability at $\text{pH} = 2$ within a potential range of approximately -0.3 V to $+0.15 \text{ V}$ vs SHE. In this range, copper remains solid and stable unless the anodic corrosion limit is reached, where copper begins to dissolve as Cu^{2+} ions. The voltammogram of Cu(111) in sulfuric acid further confirms this, with a significant anodic current increase at $+0.2 \text{ V}$ indicating copper dissolution (*part A in Figure 5.2*), and a corresponding re-deposition peak observed at $+0.15 \text{ V}$ during the reverse scan. Sulfate desorption occurs around -0.36 V , while hydrogen evolution begins at approximately -0.3 V , manifesting as a rising cathodic current (*D-H section in Figure 5.2*).

Real-time electrochemical scanning tunneling microscopy imaging of the sulfate adsorption and desorption process is feasible at specific potentials, where faradaic currents are minimal. However, during hydrogen evolution and copper corrosion,

the high faradaic currents generated at the surface can interfere with tunneling current collection. Additionally, during anodic corrosion, the surface undergoes structural degradation, which complicates STM imaging. In contrast, atomic force microscopy is less affected by these issues since the AFM tip is unbiased. This allows AFM to capture surface changes even during significant morphological transformations caused by corrosion, provided that feedback control is appropriately tuned to compensate for increased surface roughness [*see* the markers at the top of Figure 5.2 indicating the area that can be analyzed by STM and the anodic corrosion region amenable to AFM].

The data for the Cu(111) electrode and its vicinal surfaces at various relevant potentials will be presented and analyzed below. Furthermore, a comprehensive analysis of the dissolution process of the Cu(111) surface in the diluted sulfuric acid solution will be shown.

5.2.1 Bare Cu(111) in Dilute H₂SO₄ Solution

To provide a coherent context for interpreting the results from experiments on stepped vicinal surfaces, I first summarize the key findings related to sulfate adsorption on the flat Cu(111) surface, with an updated and more detailed analysis of high-resolution EC-STM data [60] [127]. This analysis places particular emphasis on the structural characteristics at the few step edges that are present among the broad terraces of the nominally flat Cu(111) surface. When a potential below the sulfate adsorption regime is applied to the Cu(111) sample, the STM reveals clean copper terraces, as shown in the pictures below (Figure 5.3, Figure 5.4 and Figure 5.5) [122] [127]. The height between these terraces corresponds to multiples of 0.2 nm, which matches the distance between Cu(111) crystal planes in the bulk (0.209 nm). While atomic resolution of the copper is not achieved, the terraces are found to be atomically flat.

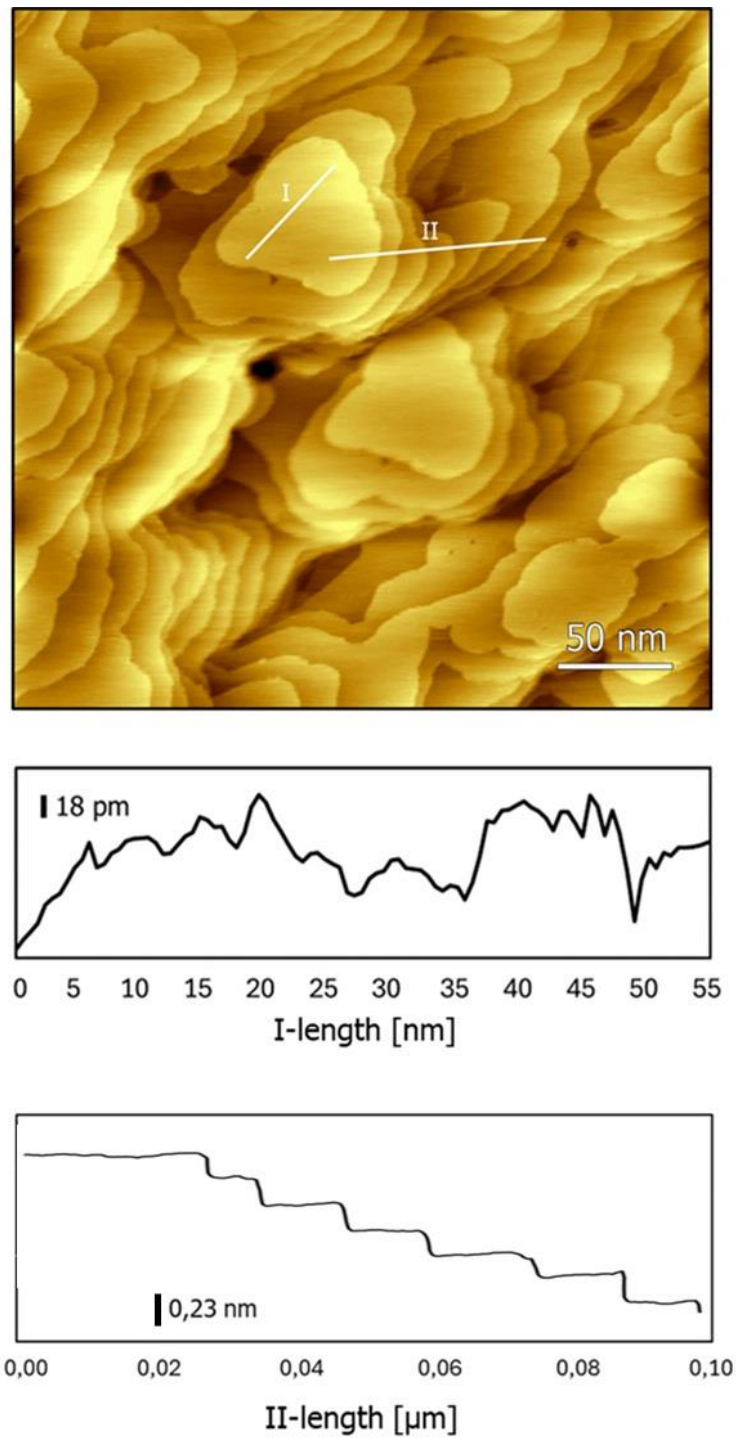


Figure 5.3: EC-STM image of the filled states ($I_{\text{tunnel}} = 1.5 \text{ nA}$; $V_{\text{bias}} = +1.1 \text{ V}$) of the clean Cu(111) surface acquired at -0.3 V ; below the image, profiles related to the I and II lines are shown.

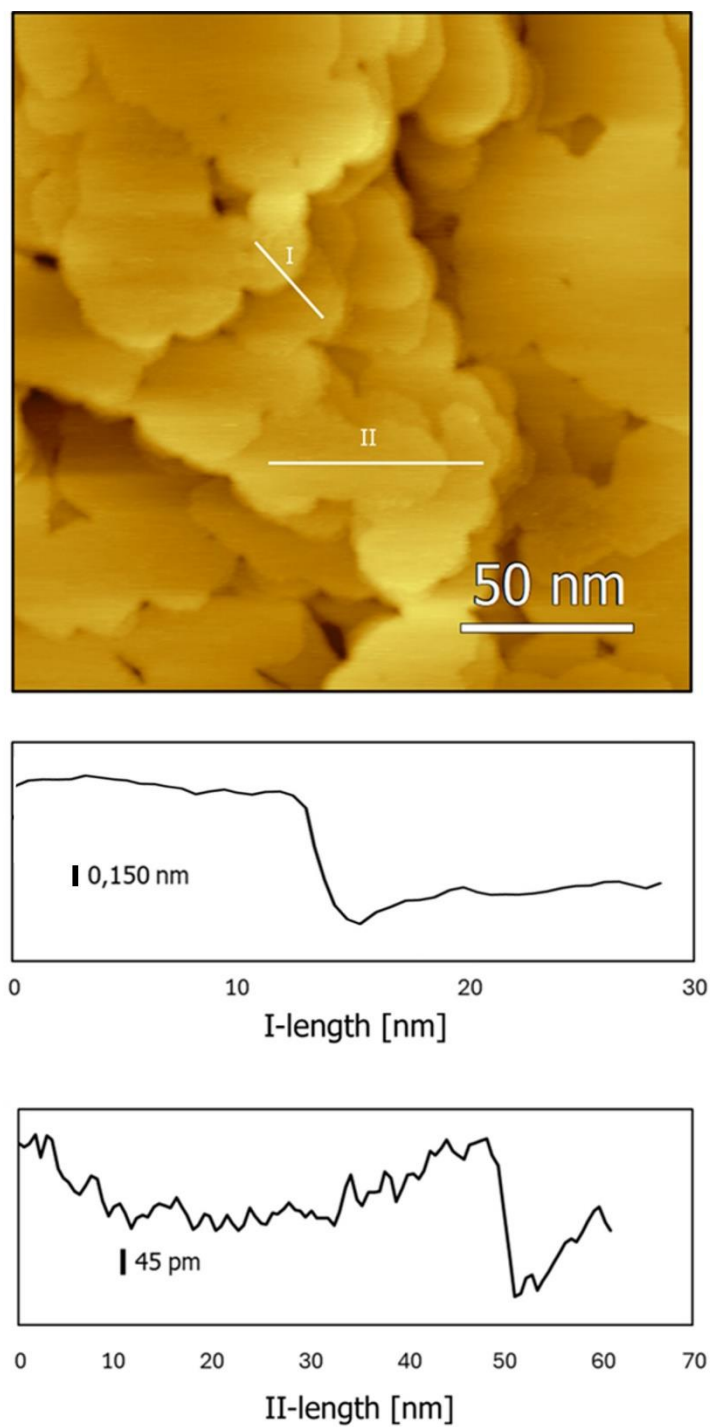


Figure 5.4: EC-STM image of the filled states ($I_{\text{tunnel}} = 1.5 \text{ nA}$; $V_{\text{bias}} = +1.1 \text{ V}$) of the clean Cu(111) surface acquired at -0.3 V ; below the image, profiles related to the I and II lines are shown.

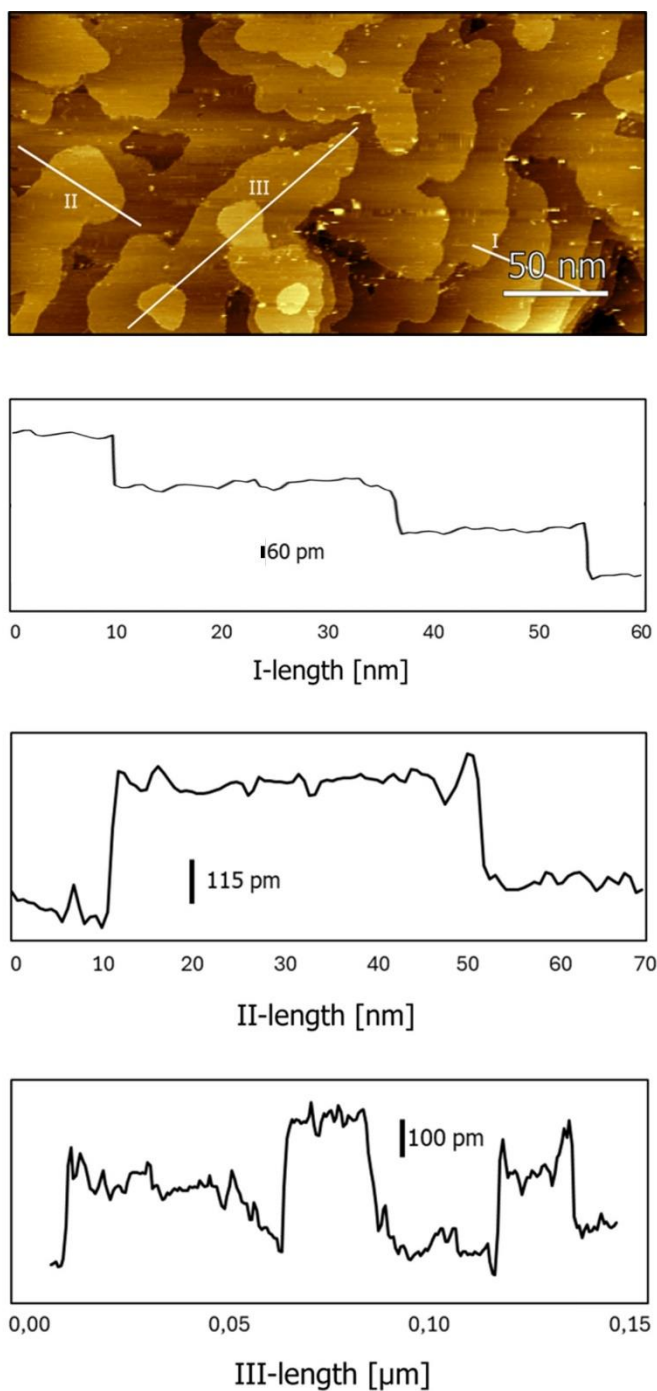


Figure 5.5 EC-STM image of the filled states ($I_{\text{tunnel}} = 1.53 \text{ nA}$; $V_{\text{bias}} = +1.1 \text{ V}$) of the clean Cu(111) surface acquired at -0.3 V ; below the image, profiles related to the I, II and III lines are shown.

Therefore, in the potential region negative with respect to the first anodic peak (typically at -0.3 V vs SHE), the surface is bare, and the atomic terraces can be

clearly observed. Their width ranges from ≈ 10 to 70 nm. Even if it can be achieved, atomic resolution of the copper surface is challenging in this region. In Figure 5.6, the atomic structure of bare copper is exhibited.

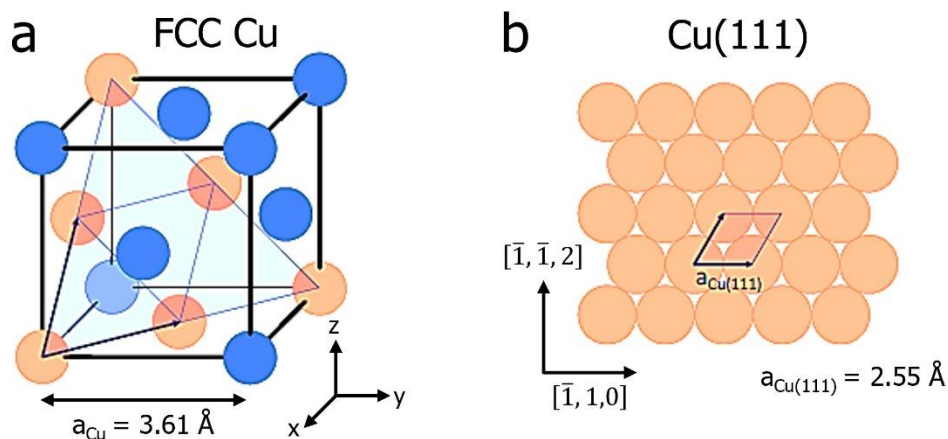


Figure 5.6: a) The cubic cell of the FCC Cu crystal, with a lattice constant parameter of $a_{Cu} = 3.61 \text{ \AA}$; the (111) plane is highlighted in blue. b) The two-dimensional Cu(111) lattice and its unit cell with a side length of $a_{Cu} = 2.55 \text{ \AA}$.

5.2.2 Moiré-superstructure Formation on Cu(111) Surface in Dilute H_2SO_4 Solution

At approximately -0.1 V/SHE , sulfate adsorption begins, leading to the formation of the distinct Moiré-superstructure. Typical STM images of the Moiré pattern, previously described, are shown in the following pictures. The superstructure is clearly visible even at the nanometric scale, where the terraces' and steps' topography are typically observed. Please, note in Figure 5.7 the simultaneous presence of the ordered adsorption phase, where both the sulfate adsorption and the formation of the Moiré pattern are visible, alongside regions of disordered adsorption, appearing as fuzzy and indistinct areas not covered by the Moiré superstructure. In these disordered regions, the surface is already fully saturated with sulfate ions, which remain mobile and disordered

prior to the formation of the ordered Moiré pattern. As a result, this disordered state is not detectable by STM at the initial stage.

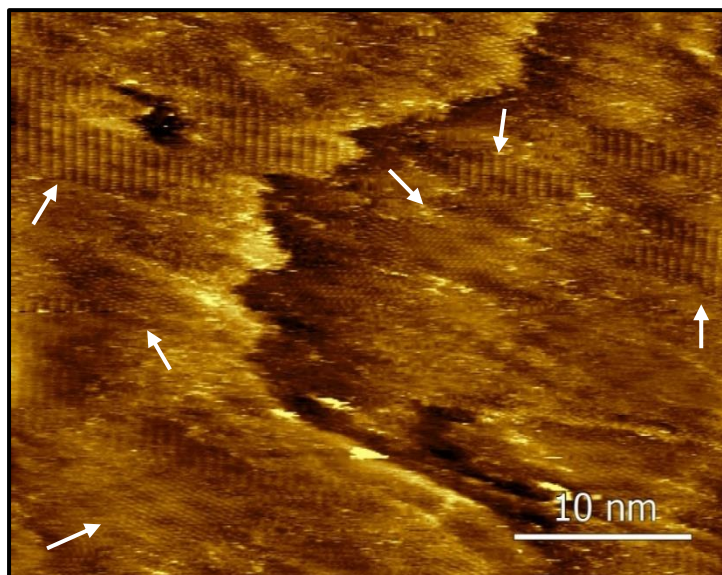


Figure 5.7: Formation of the ordered adsorption phase acquired at +0.1 V ($I_{\text{tunnel}} = 1.3 \text{ nA}$; $V_{\text{bias}} = +0.7 \text{ V}$). In the picture, it is possible to distinguish the different phases of the adsorption structure: the disordered sulfates adsorption (i.e., the fuzzy areas) and the regions where the ordered Moiré superstructure coexists with the ordered sulfate structure (like those regions marked by the white arrows).

Even Figure 5.8 is distinguished by stripe patterns, resulting from the formation of the $(\sqrt{3} \times \sqrt{7})R30^\circ$ sulfate anion structure on the Cu(111) surface. Additionally, the characteristic long-range modulation of Moiré pattern is observed. The image shows evidence of drift, which may have affected the spatial resolution during acquisition. In the picture, again, the distinct phases of the adsorbed anions can be clearly identified. These include the nebulous regions where disordered sulfate adsorption dominates, as well as areas where the ordered Moiré-superstructure is observed, accompanied by the well-defined arrangement of sulfate anions. The transition from disordered to ordered phases highlights the spatial variability of sulfate adsorption on the surface, reflecting the interplay between surface morphology and adsorbate ordering. This

distinction is crucial for understanding the underlying processes governing the formation of the Moiré-superstructure and its impact on surface reactivity. Anyway, it appears that the ordered regions have increased in number compared to those observed in the previously acquired image (Figure 5.7), suggesting that the Moiré-superstructure is continuing its expansion, progressively covering the entire scanned area. The same area shown in Figure 5.8, is reported in the image following it (Figure 5.9). The adsorption phase of sulfate anions is still clearly visible from the top of the picture; then, cycling towards the reduction direction (*i.e.*, cathodic part of the cyclic voltammetry) the desorption of sulfates is reached. As a result, the Moiré-superstructure is no longer visible.

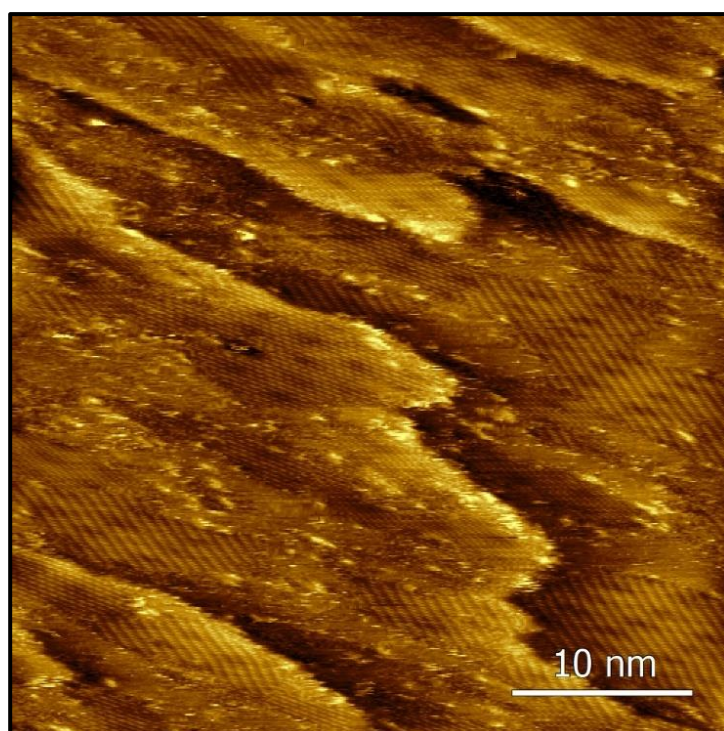


Figure 5.8: Formation of the Moiré-superstructure acquired at +0.1 V ($I_{\text{tunnel}} = 1.5$ nA; $V_{\text{bias}} = +0.7$ V). The image displays distinct phases of the adsorption anions, highlighting the nebulous regions dominated by disordered sulfate adsorption alongside areas where the ordered Moiré-superstructure and a well-defined sulfate anion arrangement are visible.

It should be noted that Figure 5.9 image was acquired *in-situ* and in real-time: starting with the potential value corresponding to the adsorption of sulfate ions (*i.e.*, $V_{\text{sample}} = +0.1$ V), we began cycling (always referring to the CV shown in Figure 5.2) until reaching the vicinity of the (pink) desorption peak, which corresponds to the white dashed line in the image [the black arrow indicates the image's acquisition direction].

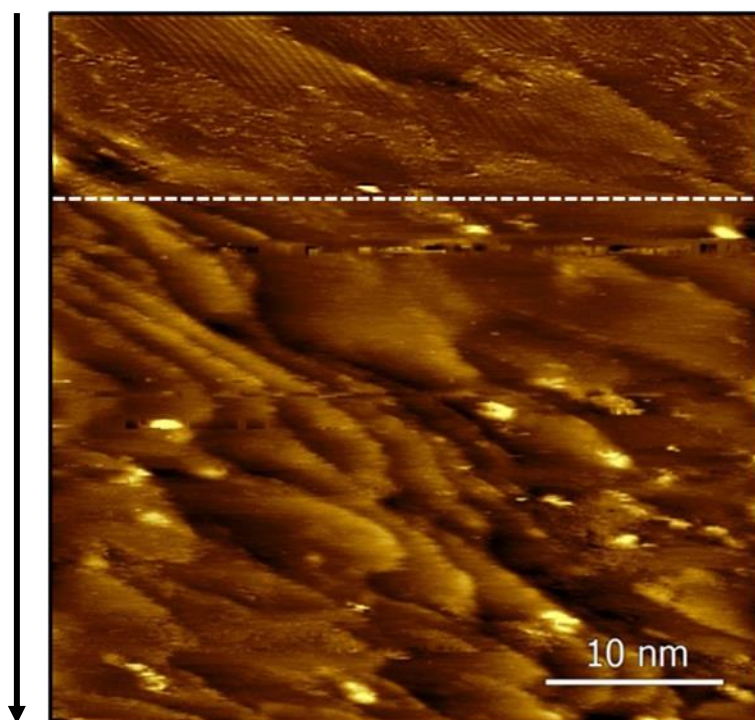


Figure 5.9: Upper part of the image: ordered adsorption phase acquired at +0.1 V ($I_{\text{tunnel}} = 1.5$ nA; $V_{\text{bias}} = +0.7$ V); *in-situ* and in real time starting of the cyclic voltammetry towards the sulfate ions desorption regime and consequent disappearance of the Moiré-superstructure at the white dashed line. The scanned area is the same as in Figure 5.8. The black arrow indicates the image's acquisition direction.

Then, following the real-time desorption process shown in Figure 5.9, the potential of -0.3 V was reached again. At this potential, a clean Cu(111) surface is obtained. According to the procedure described in Figure 5.1, after performing cycles in the cathodic region (electrochemical reduction), to ensure

the complete removal of any oxide from the surface, and allowing time for the surface to stabilize, cyclic voltammetry was restarted, reaching again the potential for sulfate ion adsorption and the subsequent formation of the Moiré-superstructure. Afterwards, an alternation between adsorption and desorption cycles was performed, as evident in Figure 5.10. The exposed sample area remained the same across all the images shown, and no experimental conditions were changed. Note how immediately the Moiré pattern appears and disappears as the sulfate ion adsorption and desorption regimes are respectively reached (the black arrow indicates the direction of image acquisition).

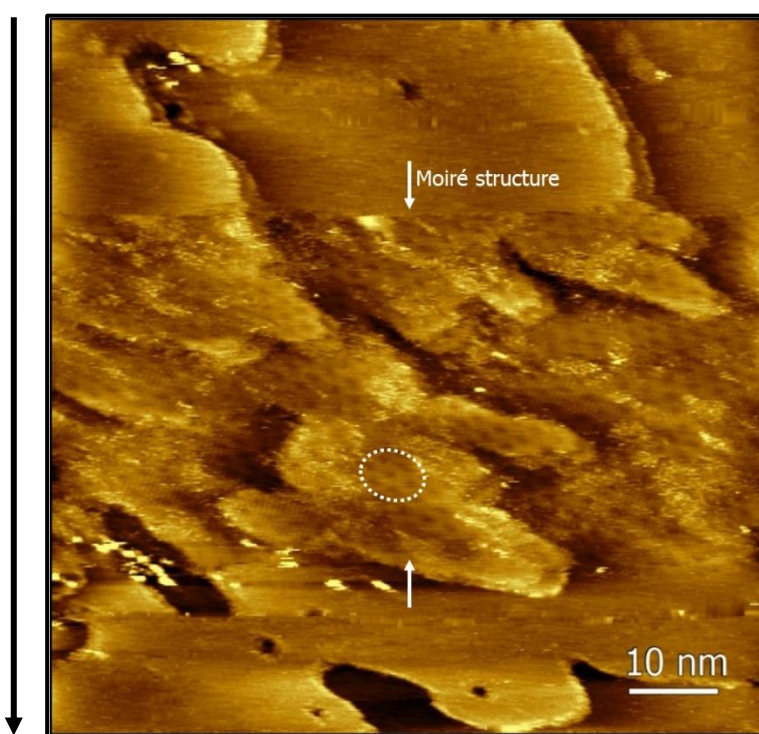


Figure 5.10: Alternation of adsorption and desorption cycles, starting from the upper part of the image in which a bare Cu(111) surface is clearly visible, with consequent appearance and disappearance of the Moiré pattern. The black arrow indicates the image's acquisition direction.

A high-resolution section of this Moiré structure is displayed in Figure 5.11, providing a detailed view of the periodic modulation. Panels *a*, *b* and *c* in Figure 5.11 present the Moiré-superstructure at varying resolutions. In panel *a*,

the superimposed "mesh" connects six darker depressions, emphasizing that the expansion of the top copper layer is anisotropic. The hexagonal mesh is slightly elongated along one of the three possible axes, a, b, and c, as indicated in panel *c* - measuring 3.45 nm along one axis and 2.70 nm along the others. Panel *b* shows a high resolved image of both the sulfate's structure and the Moiré-superstructure, marking their pattern. Panel *c* further defines the Moiré-unit, an inner hexagon of brighter intensity surrounded by the outer hexagonal Moiré-mesh of darker spots. This Moiré-unit serves as the fundamental building block of the overall Moiré-superstructure, which plays a central role in the interpretation of the sulfate adsorption process.

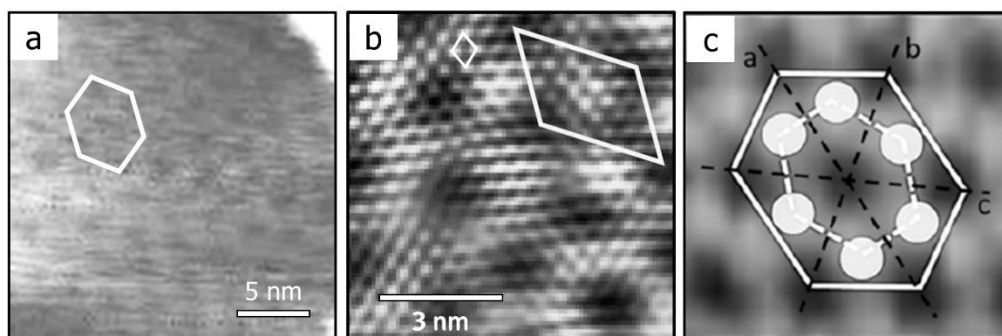


Figure 5.11: [127] a) At a potential of $E = +0.1$ V ($I_t = 1.5$ nA, $U_b = +0.7$ V), the sulfate-covered Cu(111) surface exhibits an elongated hexagonal mesh characteristic of the Moiré-superstructure. b) A highly resolved image reveals the detailed arrangement of the sulfate anions, including both the $(\sqrt{3} \times \sqrt{7})R30^\circ$ structure and the superimposed Moiré pattern, $E = +0.1$ V, $I_t = 1.5$ nA, $U_b = +0.7$ V. c) Within the Moiré-superstructure, a "Moiré-unit" (represented by an inner hexagon of brighter intensity) is nested inside the "Moiré-mesh" (the outer hexagon of darker spots), with axes labeled as a, b, and c, providing a precise depiction of the periodic modulation at the surface.

In the following discussion paragraph, I will reference previously published images to provide a clearer explanation of the phenomena occurring on the Cu(111) surface. These images will help illustrate the formation and behavior of the Moiré-superstructure during sulfate adsorption, offering valuable insight

into the processes at play. The insights gained from the Cu(111) surface will also serve as a basis for understanding the behavior on the vicinal Cu(111) surfaces data, shedding light on the key similarities and differences between these crystallographic orientations.

5.2.3 Interpretation of Surface Phenomena on Cu(111) in Dilute H₂SO₄ Solution Through Literature Images

The unidirectional expansion of the Moiré-superstructure on the Cu(111) surface can lead to the formation of three equivalent domains, each rotated by 120° relative to the others, as shown in Figure 5.12 (*particularly*, panel *a*). Evidence of the expansion of the Cu(111) layer comes from quasi-scanning tunneling spectroscopy (STS) measurements under different tunneling conditions. High-resolution STM images demonstrate this expansion: while one image (Figure 5.12*b*) shows the sulfate overlayer's structure, another (Figure 5.12*c*) reveals the expanded copper layer beneath the sulfate [128]. The copper-copper distance in the latter image is approximately 6% larger than that of a sulfate-free Cu(111) surface [60], limited to the first copper layer, which is necessary for the Moiré-superstructure formation.

This expansion introduces intra-layer stress, which can be relieved at step edges or within terraces by displacing copper atoms from the first layer. These effects are visible in Figure 5.13, where the Moiré formation begins at a step edge and spreads onto the upper terrace as copper atoms are displaced and trapped at kink sites. Eventually, copper islands, covered by the Moiré pattern, form on the terraces. Interestingly, the islands are "quantized" in complete Moiré-units, even down to a single Moiré-unit. Upon closer inspection of the small copper islands that form after sulfate adsorption, it becomes evident that these islands exhibit specific shapes and quantized sizes. Remarkably, only islands containing an integer number of Moiré-units are permitted, meaning their size and formation follow strict rules dictated by the Moiré pattern.

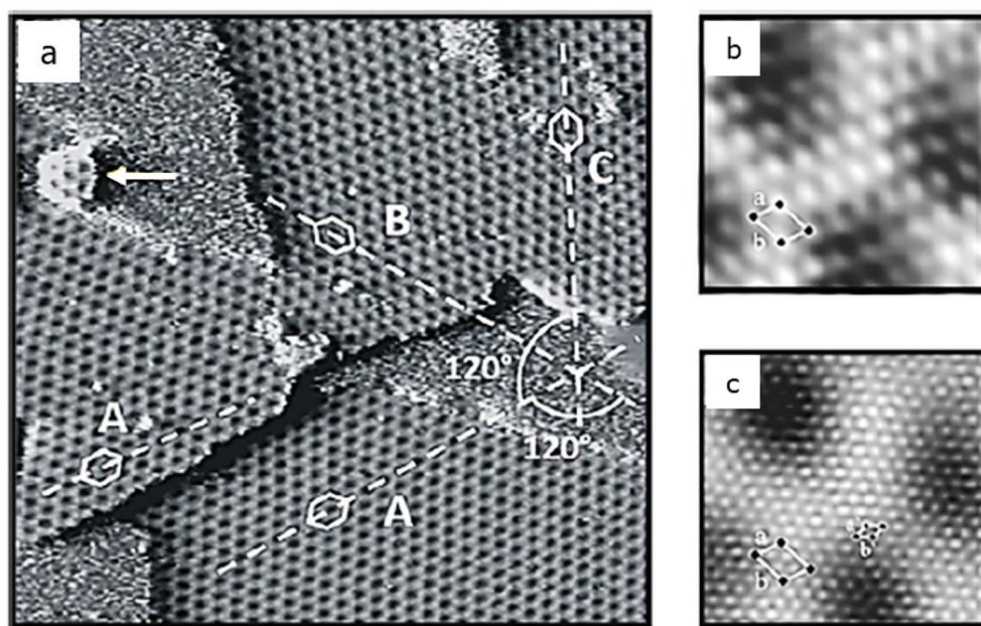


Figure 5.12: [48] [57] [62] a) EC-STM image of the Cu(111) electrode covered with the sulfate-induced Moiré-superstructure, which highlights the three rotational domains, labeled A, B, and C. Each domain is rotated by 120° relative to the others. The image covers a scan area of $101 \text{ nm} \times 101 \text{ nm}$, $U_b = 169 \text{ mV}$, $I_t = 1 \text{ nA}$. The fuzzy regions in the image indicate areas covered by sulfate SO_4^{2-} anions in a disordered phase, meaning the anions are not yet arranged in the ordered Moiré pattern. A white arrow points to a copper island that is covered by the Moiré pattern. In panels b) and c), quasi-STs imaging is used to provide direct evidence of sulfate-induced expansion of the first copper layer. Panel b) shows the $(\sqrt{3} \times \sqrt{7})R30^\circ \text{SO}_4^{2-}$ structure at high resolution over a $5.9 \text{ nm} \times 5.9 \text{ nm}$ area, $I_t = 10 \text{ nA}$, $U_b = -2 \text{ mV}$. Panel c) shows the underlying copper layer (see the smaller rhombic unit cell), again over a $5.9 \text{ nm} \times 5.9 \text{ nm}$ area, but with a lower tunneling current of $I_t = 2 \text{ nA}$ and the same bias voltage. The superimposed $(\sqrt{3} \times \sqrt{7})R30^\circ$ sulfate unit cell from panel b) emphasizes the expansion of the first copper layer induced by sulfate adsorption. This expansion is a key factor in the development of the Moiré pattern [128].

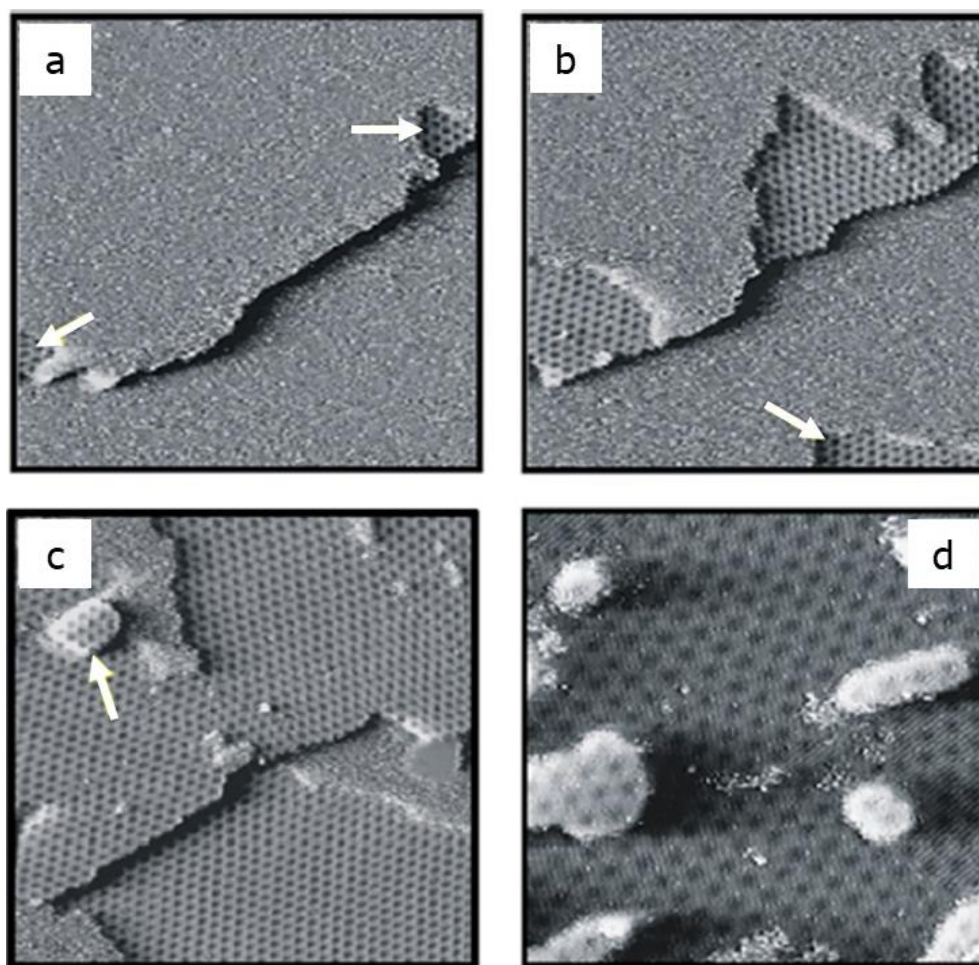


Figure 5.13: [60] Sequence of EC-STM images showing the gradual development of the sulfate-induced Moiré-superstructure on a Cu(111) electrode. The images capture key stages of this process. Panels a) to c) depict the successive growth of the Moiré-superstructure across a $101\text{ nm} \times 101\text{ nm}$ area under the conditions of $U_b = 169\text{ mV}$ and $I_t = 1\text{ nA}$. Figure 5.12a is part of this sequence, situated between panels b) and c). Panel d) emphasizes the quantized nature of the sulfate-induced copper island formation.

These islands come in various shapes, including rod-like structures with two or more Moiré-units and hexagonally symmetrical islands. Some even consist of just one Moiré depression. This observation highlights the strong structuring effect the sulfate adlayer exerts on the copper substrate. The fact that these islands follow the Moiré pattern so rigidly suggests a strong adsorbate-

substrate interaction, where the sulfate ions play a crucial role in reorganizing the copper atoms at the surface [55].

The interaction between sulfate anions and the Cu(111) surface, along with the expansion of the copper layer and the resulting Moiré formation, is summarized schematically below, in Figure 5.14.

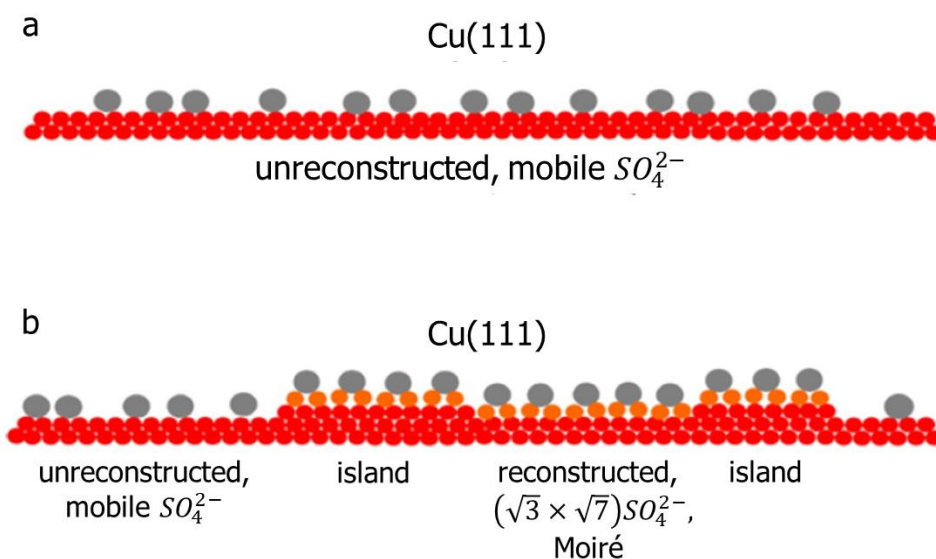


Figure 5.14: Transition from a mobile sulfate phase at negative potentials to a more structured, Moiré-superstructure phase at positive potentials, where sulfate anions enforce surface reconstruction on the copper substrate. a): at negative potentials, the Cu(111) surface remains unreconstructed, with copper (red) atoms in their original positions, and mobile sulfate anions (grey molecules) are loosely adsorbed on the Cu(111) surface, not yet in a highly ordered or structured phase. b) at positive potentials, Cu(111) surface undergoes reconstruction, resulting in a modified arrangement of copper atoms (represented as orange atoms); Cu islands form on the surface. Some regions, where the Cu(111) surface is not fully reconstructed, still show remnants of mobile sulfate anions, reflecting minor areas of the unreconstructed (111) surface.

5.3 Introduction to Vicinal Cu(111) Surfaces Immersed in Diluted H₂SO₄ Solution

The importance of studying well-defined basal plane electrodes stems from their ability to provide insight into the interaction between solution species and a single type of surface site. This allows for the acquisition of fundamental data that serve as a reference for modeling electrochemical processes. The iterative feedback between theory and experiments conducted on single-crystal surfaces enhances our understanding of reactivity and guides further refinement of experiments. In applied research, single-crystal studies have helped identify the most active surface arrangements for specific reactions. However, a conceptual limitation of basal plane electrodes is that practical electrodes do not have large, perfectly two-dimensional domains. To address this, well-defined stepped surfaces are used to better simulate the behavior of real-world nanoparticle electrodes, which are relevant for catalytic applications. Defect sites, such as steps, are often considered the most active sites for catalytic reactions. By preparing surfaces with controlled terrace and step structures, researchers can quantitatively measure the difference in reactivity between various surface features and control the density of defects [26]. Furthermore, the crystallographic structure of the electrode impacts the properties of the interphase between the electrode and the solution. Since electron transfer occurs in the narrow region between the metal surface and the solution, the characteristics of this interfacial region directly affect the rate of many reactions. Factors such as anion-specific adsorption, the distribution of charges at the interface, and the interaction of water molecules with the metal surface are crucial to fully understanding how surface structure influences electrochemical reactivity. These interfacial properties, along with surface geometry, collectively determine the overall performance and efficiency of electrochemical reactions on different crystallographic surfaces [27].

5.4 Sulfate Adsorption on Vicinal Surfaces: Structural Analysis of Cu(221) and Cu(21 21 16) Surfaces

On wide terraces, such as those on the flat Cu(111) surface, the Moiré-mesh lattice extends over long ranges. However, on narrower terraces of vicinal Cu(111) surfaces, the question arises as to whether the sulfate anions can still adsorb without Moiré formation, or whether sulfate adsorption forces a restructuring of the terraces. As we will see shortly, the study demonstrates that sulfate adsorption induces a restructuring of vicinal surfaces, governed by a "bimodal confinement effect", involving both the size of the Moiré-unit and the available "capture zone" for copper atoms, necessary to form a complete Moiré-unit.

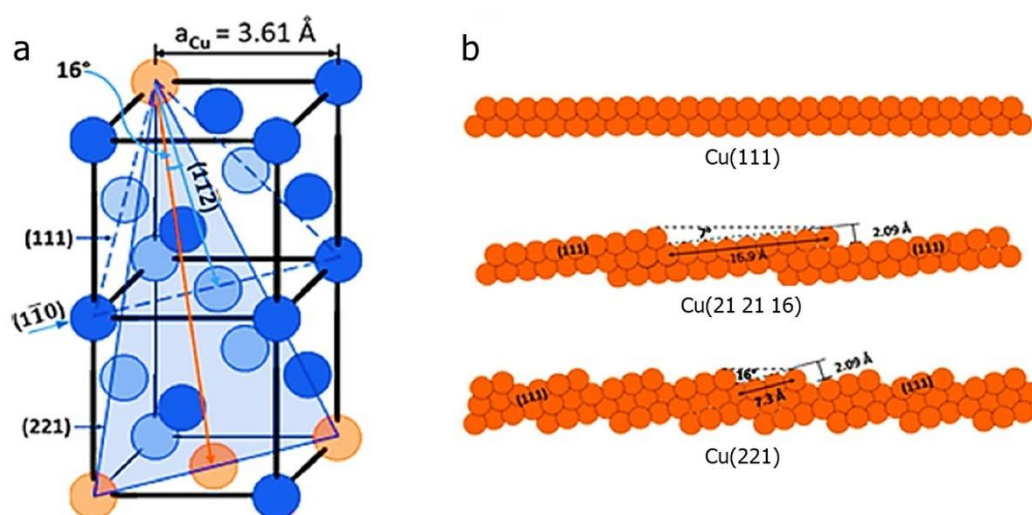


Figure 5.15: a) The FCC structure of the copper lattice, highlighting the orientation of the (111) and (221) planes. The inclination direction $[11\bar{2}]$ and the step edges direction $[\bar{1}\bar{1}0]$ are depicted, with the vicinal angle of 16° indicated. b) An ideal cross-section diagram for the flat Cu(111) surface for comparison; the Cu(21 21 16) surface, characterized by a vicinal angle of approximately 7° and terrace widths of 1.7 nm ; the Cu(221) surface, featuring a vicinal angle of about 16° , with terrace widths of 0.73 nm ; the orientation and height of the steps are clearly illustrated.

For this work, the Cu(221) and Cu(21 21 16) surfaces were selected to investigate how physical constraints affect Moiré pattern formation. The Cu(221) surface is cut with an inclination angle of about 16° , relative to the (111) plane within the (110) plane, resulting in 0.73 nm wide (111) terraces separated by monatomic steps parallel to the $[\bar{1}10]$ direction. This terrace width is smaller than the Moiré-unit dimensions, which theoretically should inhibit the formation of the Moiré pattern. In contrast, the Cu(21 21 16) surface is cut with a 7° inclination relative to the (111) plane within the (110) plane, leading to a terrace width of 1.7 nm. While this width is larger than that of the Cu(221) surface, it remains smaller than the Moiré-mesh dimensions. Therefore, both vicinal surfaces are suitable for studying how different degrees of terrace width (*i.e.*, physical restriction) affect Moiré pattern formation (Figure 5.15a and b).

5.5 Cu(21 21 16) in Dilute H₂SO₄ Solution: Expected vs Observed

Surface Structure

The ideal model for the Cu(21 21 16) surface, as illustrated in Figure 5.15b, suggests a regularly stepped surface with terraces approximately 1.7 nm wide. However, STM images (Figure 5.16) show deviations from this ideal situation. Instead of the expected uniform terrace width, the observed terrace widths range from approximately 3 to 30 nm, both before and after sulfate adsorption. This discrepancy might be due to surface irregularities caused by the harsh electrochemical etching process used in cleaning the sample.

Despite the unexpected terrace morphology, sulfate adsorption leads to the formation of a Moiré-superstructure, visible even on the narrowest sections of the terraces (indicated by white arrows in Figure 5.16). This Moiré pattern is a clear indicator of sulfate adsorption. Sulfate adsorption on the Cu(21 21 16) surface results in the formation of additional copper islands too, which are not present on the sulfate-free surface. These islands predominantly appear on broader sections

of the terraces covered by the Moiré structure. Looking in details at Figure 5.16, upon increasing the potential from -0.3 V to +0.1 V, the transition from a sulfate-free Cu(21 21 16) surface to one covered by the sulfate-induced Moiré superstructure becomes evident.

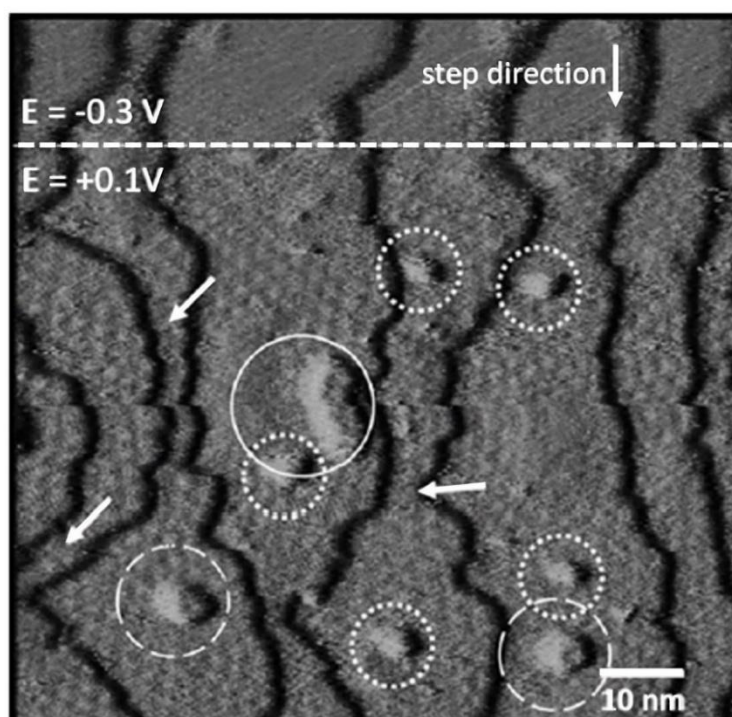


Figure 5.16: Effect of potential changes on the Cu(21 21 16) surface as observed through STM imaging. The image shows the transition [at the potential change from -0.3 V to +0.1 V] from a sulfate-free Cu(21 21 16) surface to one covered by the sulfate-induced Moiré-superstructure, highlighting the formation of islands of varying sizes corresponding to multiples of Moiré units, indicated by the white circles. Tunneling parameters are: $E = -0.3 \text{ V}$ ($I_t = 1.3 \text{ nA}$; $U_b = +1 \text{ V}$) for the bare Cu(21 21 16) surface and $E = +0.1 \text{ V}$ ($I_t = 1.5 \text{ nA}$; $U_b = +0.7 \text{ V}$) for the Moiré covered surface. Circles denoted with dotted lines enclose islands containing one Moiré unit, $r_1^* = 4.4 \text{ nm}$; circles denoted with dashed lines-----enclose islands containing two Moiré units, $r_2^* = 6.2 \text{ nm}$; circles denoted with solid lines —— enclose islands containing three Moiré units, $r_3^* = 7.5 \text{ nm}$.

This transition co-occurred with the formation of islands of varying sizes, corresponding to multiples of Moiré units. The white circles in the image enclose islands of different size. We have accurately calculated the radii of these circles in *section 5.8*. Islands containing one Moiré unit are enclosed by circles with a dotted line border, with a radius $r_1^* = 4.4$ nm, those with two units are outlined by circles with a dashed line border with a radius $r_2^* = 6.2$ nm, and those containing three units are enclosed by circles with a solid line border, with a radius $r_3^* = 7.5$ nm.

The absence of islands on sulfate-free Cu(21 21 16) and Cu(111) surfaces further highlights the role of sulfate in island formation. In addition, as emphasized in the image, there is a noticeable correlation between the position and size of the islands and the local width of the terraces. Nonetheless the unexpected surface morphology of the Cu(21 21 16) provides new insights, from non-ideal surface, into the mechanism of sulfate-induced restructuring on copper surfaces; this finding emphasizes that ideal models may not fully capture the complexities of real surfaces.

5.6 Cu(221) in Dilute H₂SO₄ solution

Cu(221) vicinal surface has narrower (111) terraces of approximately 0.73 nm, which is much smaller than the dimensions of a Moiré-mesh (~2.7 nm or 3.45 nm). This results in unique surface properties: at -0.3 V (potential at which no adsorbate is present on the Cu(21 21 16) and Cu(111) surfaces) the STM image of the Cu(221) surface immersed in 5 mM H₂SO₄ shows parallel and regularly spaced bright stripes (Figure 5.17). These stripes align with the original direction of the Cu(221) step edges, as indicated by the tip's scanning direction and sample orientation on the STM stage. When zooming into a specific region (white rectangle in Figure 5.17a), each stripe is revealed to consist of alternating brighter blobs and areas of lower intensity (Figure 5.17b). The distance between the brighter blobs is around 1.7 nm on average. Three distinct spacing values are

marked 1, 2, and 3 in Figure 5.17b, indicating variations in the distance between neighboring stripes. The truly distinctive feature of Cu(221) vicinal surface is that these values [width (1) \approx 1.5 nm, width (2) \approx 2.6 nm, width (3) \approx 4 nm] are significantly larger than the nominal terrace width of the bare Cu(221) surface, suggesting surface restructuring or other effects at play during imaging.

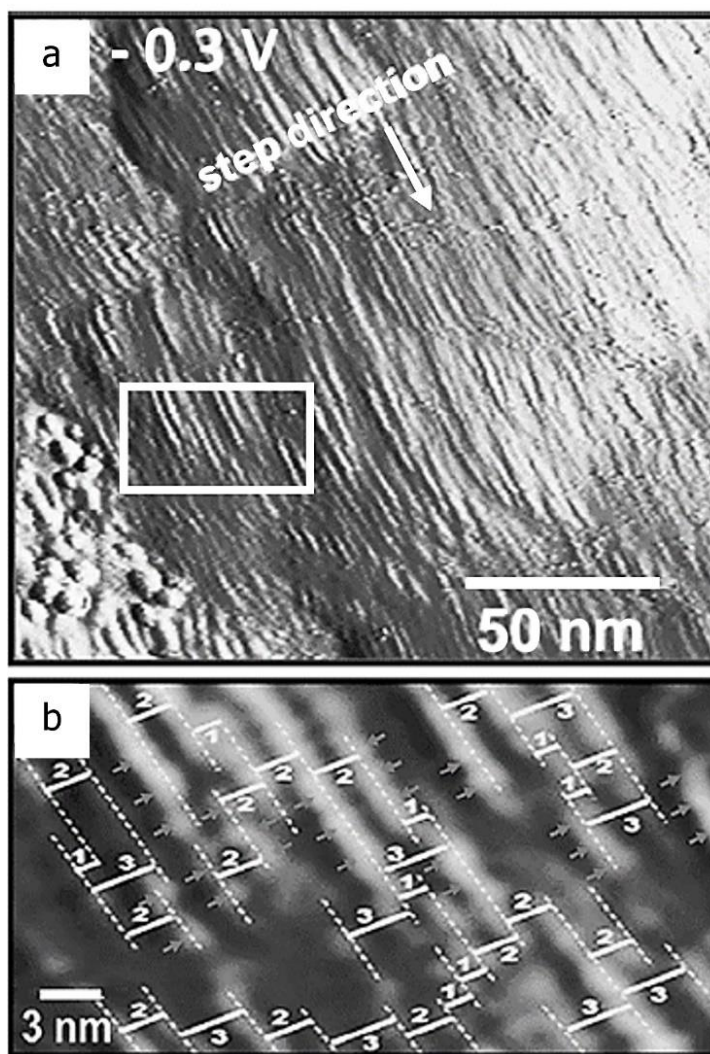


Figure 5.17: a) STM observation of the Cu(221) surface after sulfate adsorption at $E = -0.3$ V, $I_t = 1$ nA, $U_b = +0.7$ V; b) A zoomed-in view of the white rectangle in the first image shows three distinct widths between the bright stripes. These widths are: width (1) \approx 1.5 nm, width (2) \approx 2.6 nm, width (3) \approx 4 nm. The terraces' widths after sulfate adsorption are significantly larger than the original terrace width of the bare Cu(221) surface, which is only 0.73 nm.

5.7 Clarified Analysis of Step Edges on the Sulfate-Covered Cu(111)

Surface

The sulfate-induced restructuring of both the Cu(21 21 16) and Cu(221) surfaces can be understood through a unified model, taking into account the Moiré structure's formation on the flat Cu(111) surface and the associated atomic rearrangements. The following key points are involved (*see also section 2.1.3*):

- The sulfate-induced expansion of the first Cu layer on Cu(111) results in a decrease in atomic density, approximately by 12%; this causes a mismatch between the first and second copper layers, leading to the visible formation of the Moiré-superstructure and the appearance of Moiré-covered Cu islands. This expansion generates internal stresses, which are most easily relieved at step edges or within terraces. These stresses can result in the displacement of Cu atoms from the first atomic layer.
- The “Moiré-units” play a key role in the restructuring process. Step edges, kinks, islands and their rims are always composed of complete Moiré-units. The three rotational domains (A, B, and C) of the Moiré-superstructure on Cu(111) (as depicted in Figure 5.12) lead to two possible orientations of Moiré-units along step edges and rims, derived from A and B (or equivalently C) domains. These orientations are marked by white rectangles in Figure 5.18*a*, and are shown in more detail in Figure 5.18*b* and *c*.
- On the Cu(21 21 16) surface, the quantized size of the islands, each composed of multiples of Moiré-units, helps explain the relationship between island size and local terrace width. The limited terrace width constrains the formation and size of these islands, leading to the observed behavior (*see section 5.8 below*).

- On the Cu(221) surface, the orientation of the Moiré-units along step edges (derived from either A or B/C domains) provides a coherent explanation for the unique restructuring observed on this surface, particularly the changes in terrace width and step morphology (see section 5.8 below).

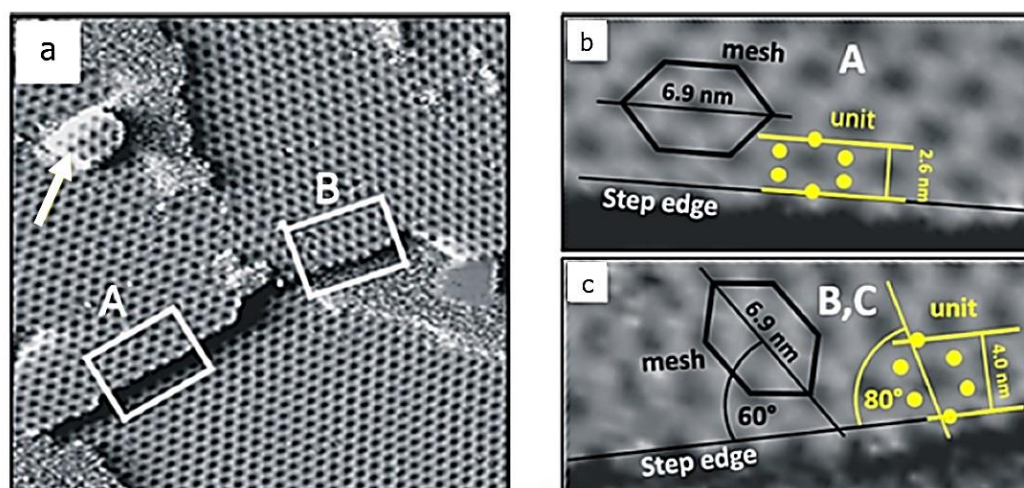


Figure 5.18: a) STM image of the growth of a Moiré-covered island [60], highlighted by the white arrow (image dimensions: 101 nm x 101 nm, bias voltage $U_b = 169$ mV, tunneling current $I_t = 1$ nA). b) and c) present zoomed-in views of the step edges contained within the white rectangles from panel a), illustrating the different orientations (A or B, C) of the Moiré-meshes.

Thus, the sulfate-induced restructuring of these surfaces, including the formation of Cu islands and terrace rearrangements, is directly linked to the intrinsic properties of the Moiré-superstructure and the resulting stress relief mechanisms at step edges and within terraces.

5.8 Discussion of Cu(21 21 16) and Cu(221) in Dilute H₂SO₄ solution

The structural analysis of the sulfate-induced Moiré-superstructure on the Cu(111) surface reveals that the size and distribution of the sulfate-induced islands on the

Cu(21 21 16) surface are closely related to the variable terrace widths. The changing width of these terraces creates a confinement effect that directly influences island formation.

The sulfate-induced islands are formed by Cu atoms expelled from the first copper layer, as a result of sulfate adsorption and the lateral expansion of the top layer. This process occurs independently of step edges, which are not the source of these atoms. The islands are monolayer-thick and are covered with sulfate, stabilizing them only when they consist of complete Moiré units. The presence of the Moiré-superstructure on the islands means that the Cu-Cu distances within the islands is expanded too; underneath the islands, the copper atoms in the second layer remain unaffected by this expansion. This means that the lattice underneath the islands retains its original Cu-Cu distance, unlike the expanded structure in the top layer. Each island forms within a "capture zone", a specific area on the terrace from which Cu atoms are drawn. The size of these zones is determined by the number of copper atoms needed for one or more Moiré units, required to form stable islands. Figure 5.16 demonstrates these capture zones, showing islands bordered by circles corresponding to their respective radii. The islands can only form on terraces wide enough to supply the necessary number of Cu atoms, explaining why no islands are observed on narrow terraces. The number of Cu atoms and the minimum surface area providing this number, *i.e.*, the minimum "capture zone", can be calculated. To achieve this, and to explain in detail the correlation mentioned so far between the surface phenomena of Cu(111) and what occurs on the Cu(221) and Cu(21 21 16) surfaces, we have developed an appropriate and accurate mathematical model, which is presented below [127].

Regular hexagon

Assuming a regular hexagonal Moiré-superstructure area, with a the length of one side of the hexagon, namely $a = 2.70$ nm, the area A of a regular hexagon can be calculated using the formula:

$$A_{hex} = \frac{3\sqrt{3}}{2} a^2$$

Therefore, the area of one regular (sulfate-covered) hexagonal mesh of the Moiré-superstructure is:

$$A_{mesh} = 18.94 \text{ nm}^2$$

This area can be split in 36 triangles X, as reported below, in Figure 5.19:

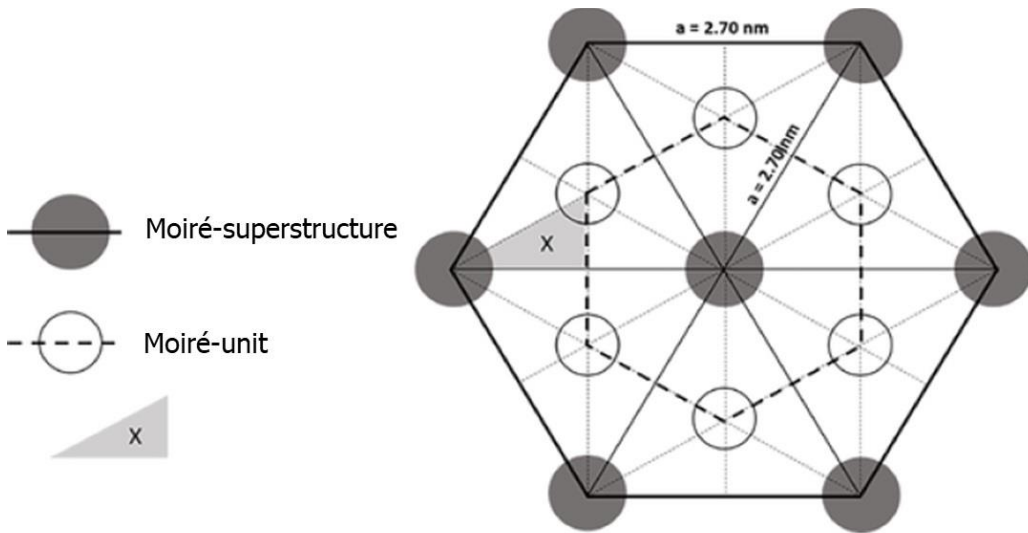


Figure 5.19: Scheme of the regular hexagonal Moiré-superstructure area, divided in 36 triangles X, and of the Moiré-unit area.

The enclosed Moiré-unit area surrounding 12 triangles, *i.e.*, the area of a Cu island covered by just one Moiré-unit, is:

$$A_{unit} = \frac{1}{3} A_{mesh} = 6.31 \text{ nm}^2$$

At the sulfate-free Cu(111) surface, the area of the smallest hexagon of Cu atoms (not the unit cell), enclosing 3 Cu atoms per cell, is:

$$A_{3Cu} = \frac{3}{2} a_{Cu}^2 \sqrt{3}$$

with $a_{Cu} = 0.256 \text{ nm}$.

Accordingly, at the sulfate-free Cu(111) surface, the specific area for one Cu-atom within the first copper layer is:

$$A_{1Cu} = \frac{1}{2} a_{Cu}^2 \sqrt{3} = 0.0568 \text{ nm}^2$$

Cu(111) surface gives the number of Cu atoms per Moiré-unit:

$$\frac{A_{unit}}{A_{1Cu}} = \frac{6.31 \text{ nm}^2}{0.0568 \text{ nm}^2} = 111 \text{ Cu atoms}$$

This means that one Moiré-unit covers an area equivalent to that of 111 copper atoms on the sulfate-free Cu(111) surface.

Given the linear expansion (6%) of the Cu(111) surface upon sulfate adsorption, the number of Cu atoms per Moiré-unit is reduced from 111 to 98. Consequently, to form a copper island hosting one Moiré-unit after sulfate adsorption, we need 98 Cu atoms (within the Moiré unit) plus 13 additional atoms to restore the unexpanded Cu layer underneath. We can suppose that the total number of 111 atoms required is collected from the area surrounding the island where Cu atoms are expelled, due to the expansion. Given the sulfate-induced expansion of the Cu(111) surface, the number of copper atoms per unit area decreases from 17.61 atoms/nm² on the unperturbed surface to 15.50 atoms/nm² on the expanded surface.

For the unperturbed surface:

$$\frac{1}{A_{1Cu}} = 17.61 \frac{\text{Cu atoms}}{\text{nm}^2}$$

For the expanded Cu surface:

$$\frac{1}{\bar{A}_{1Cu}} = 15.50 \frac{Cu \text{ atoms}}{nm^2}$$

As a result, the expansion of the Cu(111) surface upon sulfate adsorption frees 2.1 Cu atoms per nm^2 . To collect 111 atoms needed for a single Moiré-unit, the "capture zone" is calculated as $\frac{111}{2.1} = 52.86 \text{ nm}^2$. Assuming an isotropic (circular) capture zone for the free movements of Cu atoms, the radius of this zone is

$$r_1 = \sqrt{\frac{52.86}{\pi}} = 4.1 \text{ nm}$$

For islands hosting two or three Moiré-units, the collection area increases accordingly. The radii of the circular capture zones are respectively calculated as:

$$r_2 = \sqrt{\frac{2 \times 52.86}{\pi}} = 5.8 \text{ nm}$$

$$r_3 = \sqrt{\frac{3 \times 52.86}{\pi}} = 7.1 \text{ nm}$$

Elongated Moiré-superstructure and Moiré-unit

To refine the previous analysis and account for the uniaxially elongated Moiré-superstructure, we must adjust the calculations to reflect the actual elongated dimensions of the Moiré-units.

Figure 5.20, comparing the regular and elongated Moiré-superstructure, highlights how changes in the periodicity lengths affect the overall structure. In a regular

Moiré-superstructure, the periodicity length is uniform across all directions, whereas, in the elongated Moiré-superstructure, one direction has a longer periodicity (3.45 nm) compared to the others (2.70 nm and 2.70 nm). This leads to an asymmetric structure where the Moiré pattern is elongated along one direction and compressed in the perpendicular direction.

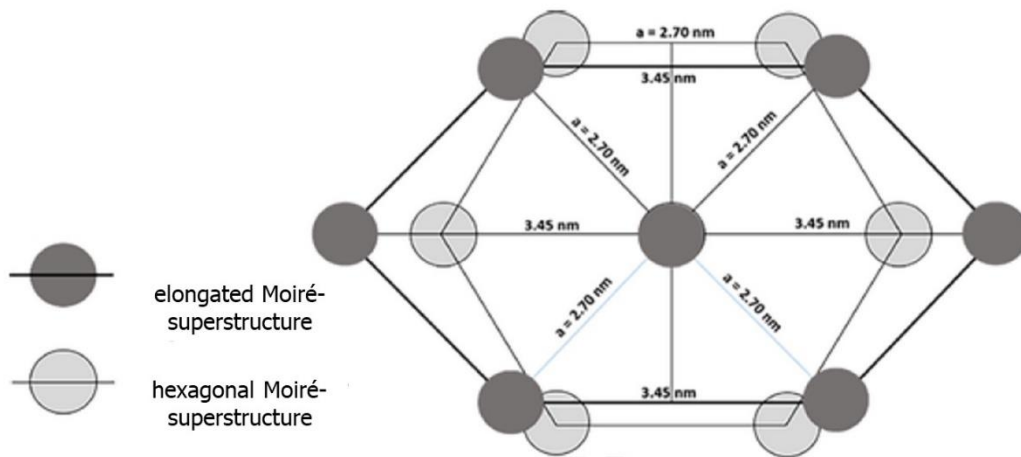


Figure 5.20: Scheme of the regular hexagonal Moiré-superstructure compared to the real elongated Moiré-superstructure.

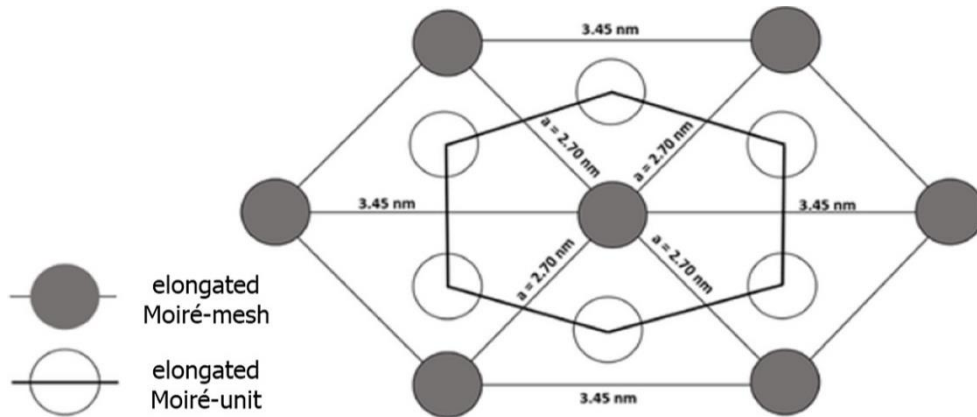


Figure 5.21: Scheme of the real elongated Moiré-superstructure area and of the real elongated Moiré-unit area inside.

Figure 5.21 illustrates one real elongated Moiré-mesh enclosing the corresponding real elongated Moiré-unit. For the sake of simplicity, the bright dots of the Moiré-

unit are placed at the center of gravity of each of the six triangles of the surrounding Moiré-superstructure. Given the dimensions of the Moiré mesh, its area can be calculated as follows:

$$A_{mesh}^* = \sqrt{(2.7nm)^2 - \left(\frac{3.45nm}{2}\right)^2} \times \frac{3.45nm}{2} \times 6 = 21.50 \text{ nm}^2$$

This value is 13.5% greater than A_{mesh} , for the regular hexagonal structure. By using this area $A_{mesh}^* = 21.50 \text{ nm}^2$, graphical determination of the area for the enclosed elongated Moiré-unit yields:

$$A_{unit}^* = 7.14 \text{ nm}^2$$

This result represents a 13.2% increase over the area A_{unit} . Consequently, the ratio of the unit area to the mesh area is:

$$\frac{A_{unit}^*}{A_{mesh}^*} = \frac{7.14}{21.50} = 0.332$$

This ratio remains approximately 1/3, consistent with the non-elongated Moiré-superstructure.

From the definition of A_{mesh}^* , and comparing it to $\frac{A_{unit}}{A_{1Cu}}$, it can be determined that the number of copper (Cu) atoms required to construct a single island equivalent to one elongated Moiré unit is:

$$\frac{A_{unit}^*}{A_{1Cu}} = 125 \text{ Cu atoms}$$

Accordingly to the model established previously, these 125 Cu atoms can be obtained from an area of 59.52 nm^2 . The corresponding radius of this “capture zone” is $r_1^* = 4.4 \text{ nm}$.

For islands containing two or three Moiré units, the radii of their respective capture zones are:

$$r_2^* = \sqrt{\frac{2 \times 59.52}{\pi}} = 6.2 \text{ nm}$$

$$r_3^* = \sqrt{\frac{3 \times 59.52}{\pi}} = 7.5 \text{ nm}$$

Therefore, the minimum number of Cu atoms per Moiré-unit is $n = 125$ Cu atoms, for one Moiré-unit originated from a minimum circular “capture zone” of radius $r_1^* = 4.4 \text{ nm}$. The zones bordered in Figure 5.16, corresponding to the growth of one, two or three Moiré-units, correlate with the local terrace width. No islands are observed on narrow terraces due to insufficient area to collect the quantity of Cu atoms necessary for the formation of a Moiré unit. It follows that the step edges, sealed by complete Moiré units, do not contribute to island formation. The islands form entirely from Cu atoms within the terrace area, and fluctuations of Moiré units from step edges onto terraces have not been observed. This further supports the idea that step edges play only a minor role in the growth process.

In conclusion, the Cu(21 21 16) surface provides a unique opportunity to study the atomistic mechanism of island formation. The confinement effect imposed by varying terrace widths determines the size and distribution of the sulfate-induced islands. This highlights the crucial role of terrace size in forming stable islands, as sufficient terrace area is required to assemble the necessary Cu atoms for Moiré-unit growth. The inertness of step edges, sealed by Moiré units, prevents them from contributing Cu atoms, further emphasizing the terrace's role in island formation.

Regarding Cu(221), the interpretation of the stripes can be reconciled with the Moiré structure observed at step edges of the Cu(111) surface, as illustrated in Figure 5.18*b* and *c*. Specifically, a row of Moiré units with orientation A along a

step edge measures approximately 2.6 nm in width, whereas a row of Moiré units with orientation B (or C) has a width of about 4 nm. These measurements correspond well with the spacings of approximately 2.6 nm and 4 nm between the bright stripes shown in Figure 5.17. This correlation supports the notion that sulfate adsorption on the Cu(221) surface leads to an expansion of the terraces to a minimum width sufficient to accommodate either one row of Moiré units of orientation A (spacing 2 in Figure 5.17*b*) or orientation B (or C) (spacing 3 in Figure 5.17*c*). The observed amplitude and periodicity of approximately 1.7 nm between the brighter features (indicated by small arrows in Figure 5.17*b*) are also consistent with the respective orientations A and B of the Moiré structure. The less common spacing, labeled as spacing 1, represents the difference between spacing 3 and spacing 2 and appears at dislocation points between these spacings. In summary, the restructuring of the Cu(221) surface upon sulfate adsorption is driven by the formation of complete Moiré units, which outweighs the stability of the adsorbate-free Cu(221) step structure. This results in terrace widening to the minimum width required to accommodate a single row of Moiré units of either orientation A or B (or C). The adsorption of SO_4^{2-} thus induces surface faceting and may alter the vicinal angle. The Cu atoms displaced during the Moiré formation are not observed as extra islands, unlike those on the Cu(21 21 16) surface, suggesting that these atoms are likely incorporated into the overall restructuring of the steps themselves.

5.9 EC-AFM of Cu(111) in Dilute H_2SO_4 Solution during Anodic Surface Dissolution Process

As mentioned above, from the Cu Pourbaix diagram in Figure 2.1 it is known that, in acidic environments such as at $\text{pH} = 2$, the electrochemical behavior of a Cu(111) electrode can be analyzed by tuning the electrochemical potential between -0.4 V and +0.2 V (*vs* SHE). This range includes the anodic corrosion

limit too, where Cu^{2+} ions are released from the electrode surface due to copper dissolution. This behavior is clearly seen in the voltammogram (Figure 5.2), where strong anodic current increase (A) at +0.2 V indicates copper corrosion or dissolution (Cu atoms are oxidized to form Cu^{2+} ions). It is also recalled that the small negative peak (B) at +0.15 V during the reverse scan represents copper re-deposition, as the Cu^{2+} ions in the solution are reduced back to solid copper on the electrode surface. This voltametric behavior reflects the typical cycle of copper oxidation and reduction in an acidic medium under applied potentials.

During sulfate adsorption and desorption processes, STM can effectively track surface changes in real-time without being affected by the charging or discharging currents of the adsorbing or desorbing anions. However, significant challenges arise during cathodic hydrogen evolution and anodic copper corrosion. These processes generate high faradaic currents at the surface, which can interfere with the collection of tunneling current, making it difficult to maintain clear imaging with STM. Furthermore, the Cu surface undergoes structural disintegration throughout the dissolution process, which further diminishes the resolution of the STM images. In such cases, AFM offers a better alternative, as the AFM tip is not biased, and the technique does not rely on tunneling current. AFM can manage the significant morphological changes caused by surface corrosion, as its feedback control can be tuned to adapt to increased surface roughness, ensuring continued high-resolution imaging despite these challenges.

After confirming the characteristic structure of the SO_4^{2-} adsorption phase (corresponding to regime E in Figure 5.2) by a complete STM characterization, a new measurement was initiated, extending the investigation into the anodic corrosion regime. To achieve this, the STM scanner was removed, and the AFM head was inserted (as illustrated in Figure 4.7). During this transition, a potentiostat was connected to the sample to maintain the Cu(111) specimen at a potential of -0.3 V, ensuring that no chemical reactions occurred on the electrode surface during the switch from STM to AFM.

The AFM image in Figure 5.22 [122] provides a large-scale view of the clean Cu(111) surface, showing flat lamellar terraces similar to those observed in the

STM image in Figure 5.3, Figure 5.4 and Figure 5.5. The terraces are occasionally attacked by globular structures, which are speculated to be contaminants or residues from the electropolishing process in orthophosphoric acid. Height profiles along the white lines “a” and “b” confirm the presence of multi-layer Cu islands, with heights reaching up to six layers (as shown in profile *b*). Panels I.II–I.IV focus on regions within panel I, featuring lamellar terraces that appear flatter, though with lower resolution than seen in STM, consistent with the flat terraces detected earlier.

As the anodic corrosion potential is reached (marked by the white solid line in Figure 5.23*a*), the copper surface undergoes a dramatic transformation, where the flat lamellar terraces disappear [122]. This is evident from the profiles acquired along the white dashed lines I and II, indicating surface roughening, with depressions as deep as 5 nm (darker holes). The image becomes blurred, suggesting increased surface mobility, and the distinct island’s contours seen in Figure 5.22*I* are lost. Despite the disintegration, a globular structure marked by a star (*) remains unaffected, suggesting it may be an insoluble copper compound from the pretreatment process rather than pure copper.

Upon reversing the applied potential (white solid line in Figure 5.23*b*) during copper re-deposition (point B in Figure 5.2), the flat lamellar terraces reappear, although their lateral size is significantly reduced. Before corrosion, the terraces had a mean diameter of about 200 nm, but after the process, this shrank to 100 nm or less.

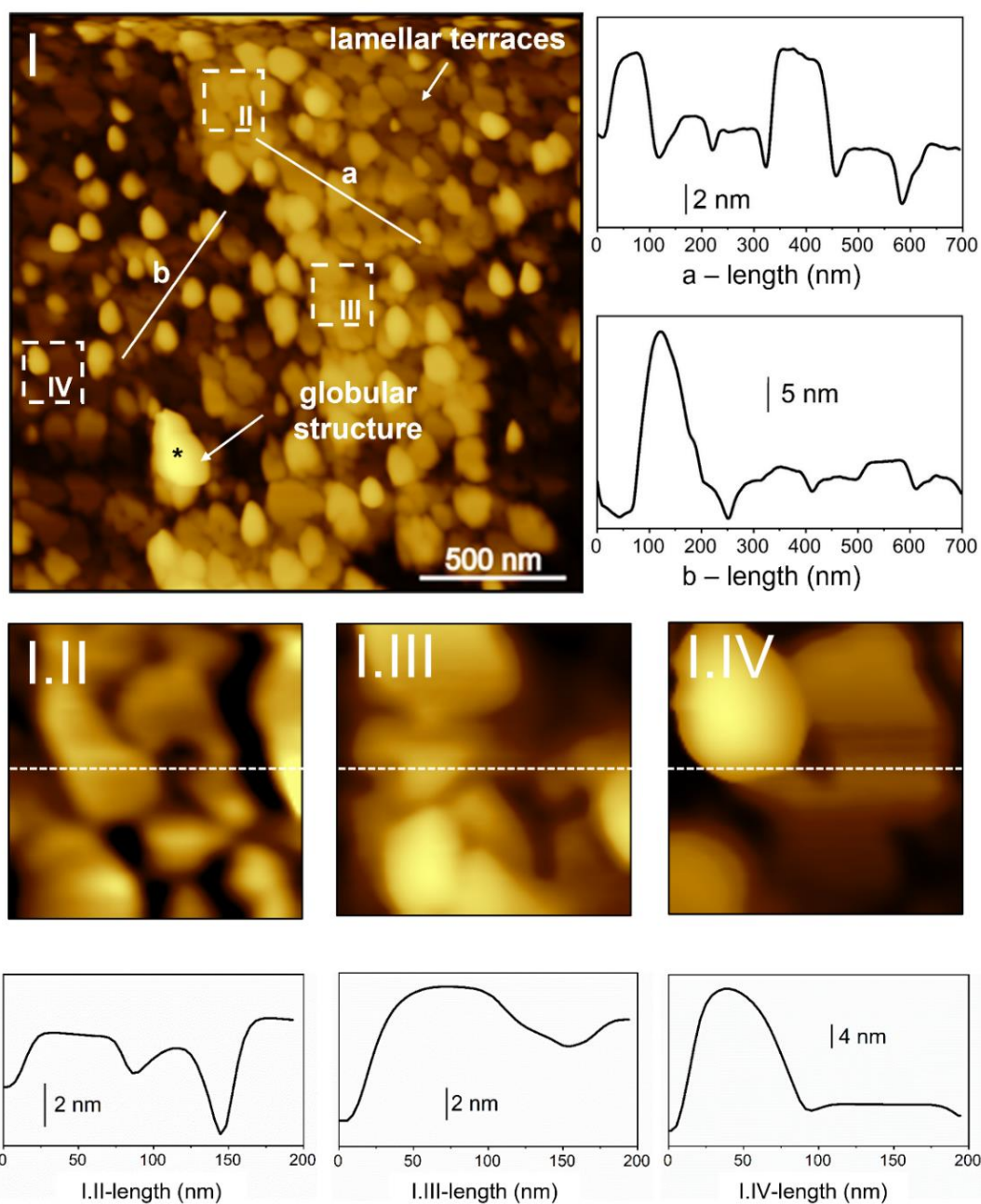


Figure 5.22: $[122]$ EC-AFM of the clean $\text{Cu}(111)$ surface immersed in sulfuric acid at -0.3 V. Panel I shows flat lamellar terraces, typical of the $\text{Cu}(111)$ surface, which are partially affected by globular structures. A dark star marks a prominent globular structure used as a reference feature for subsequent acquisitions, ensuring consistency between successive images. Profiles a and b are plotted on the right side of the image. Panels I.II - I.IV: blow-ups of specific regions of the surface, highlighted by the dashed squares in panel I.

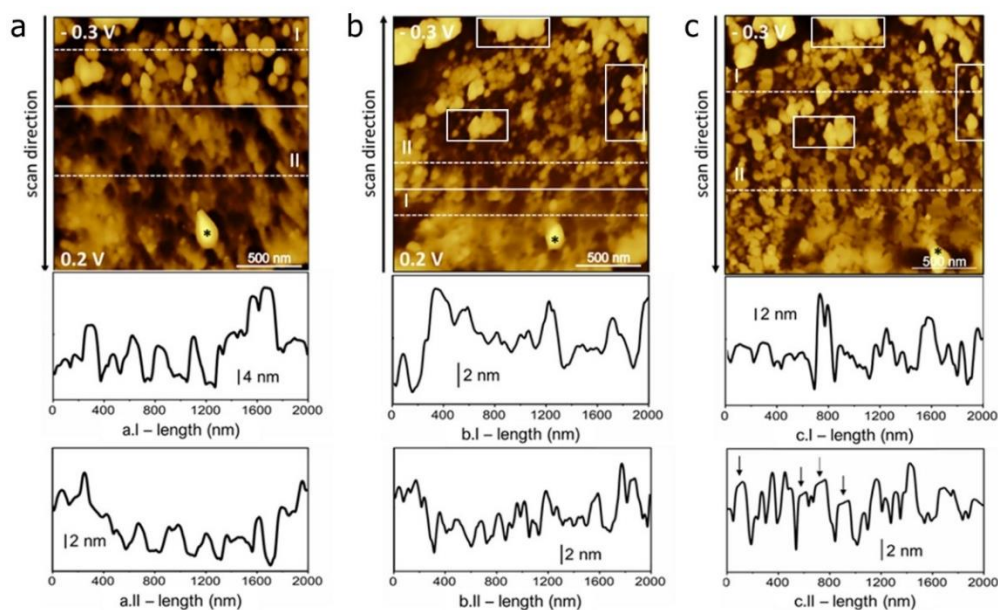


Figure 5.23: [122] EC-AFM images tracking the surface morphology of Cu(111) during the copper anodic corrosion and re-deposition processes [$(2 \times 2) \mu\text{m}^2$]. Panel a): the white solid line marks the moment when the EC potential reaches 0.2 V, i.e., the onset of copper corrosion, and is held constant during the image acquisition (see scan direction). Profiles acquired along the white dashed lines at the bottom of the panel indicate the formation of depressions, suggesting intense surface disintegration during corrosion. Panel b): copper re-deposition process. The EC potential is linearly reduced from 0.2 V to -0.3 V and then held fixed to facilitate the copper re-deposition; the white solid line indicates when the re-deposition peak is reached. Panel c): full image post re-deposition, captured at -0.3 V. The white dashed lines mark the profiles reported at the bottom of the panels, which illustrate the new surface height and the reduced size of terraces. The white squares in panels b) and c) are highlighted to compare specific regions of the scanned area with Figure 5.24, emphasizing consistent reference points for surface analysis.

A wider scan of the Cu(111) surface post re-deposition (Figure 5.24) includes the same features as Figure 5.23c, showing that the AFM tip scan had a negligible influence on the EC processes (dissolution and re-deposition) [122]. However, the central part of Figure 5.24, where previous scans were made, appears to be more uniform in height, and the interruption of the dotted white line at the bottom shows

a sharp contrast change between the brighter and darker areas. This shift correlates with the scanned region of Figure 5.23, suggesting that the AFM tip may have limited the height of the islands during the re-deposition. A similar effect might occur with the STM tip, although no clear evidence was found.

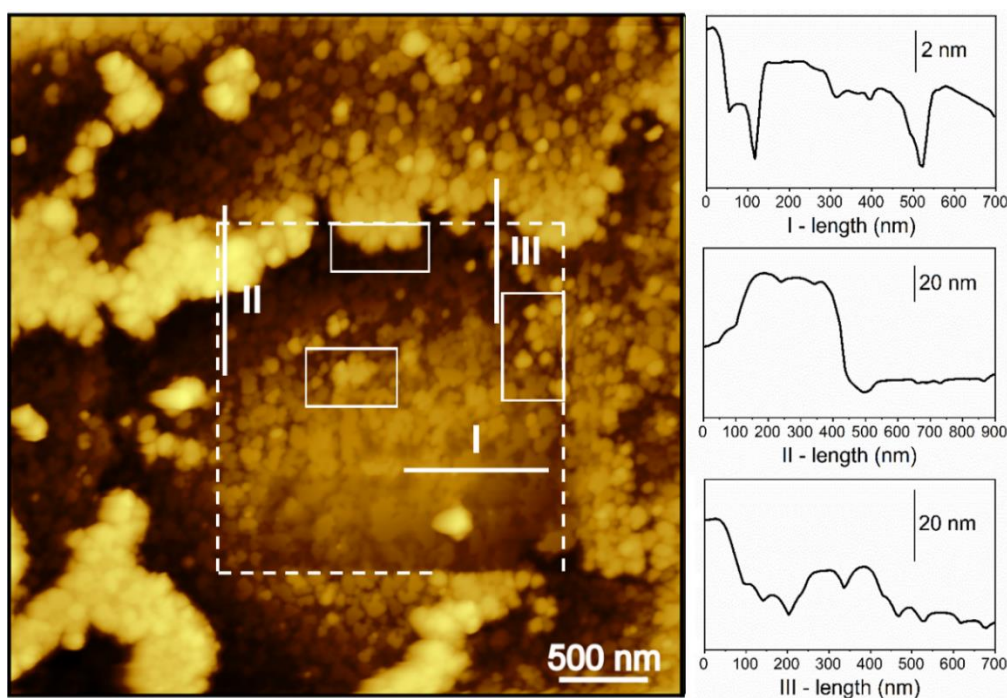


Figure 5.24: [122] [(4 × 4) μm²] EC-AFM image showing the Cu(111) surface after the copper re-deposition process at ≈ 15 V. The white dotted lines outline the specific area where the images from Figure 5.23 were taken. In addition, the large, dashed square contains three rectangular regions, which are used to correlate and compare with the same regions highlighted in Figure 5.23. The profiles on the right side were acquired along the white full lines.

To verify and corroborate our earlier observations, we replaced the AFM head with the STM scanner again to perform a final EC-STM characterization after the corrosion process (Figure 5.25) [122]. The resulting topography is markedly different from the one previously displayed in Figure 5.3, Figure 5.4 and Figure 5.6. This variation aligns with the increasing surface roughness observed as the number of dissolution and re-deposition cycles grows. The once flat and expansive

terraces have now diminished in size, a finding consistent with the results obtained from the AFM; the steps separating consecutive copper terraces are clearly visible and are delineated in the profile taken along the white full line, which is displayed at the bottom of the image. Additionally, numerous roundish features have appeared across the surface, further altering the image.

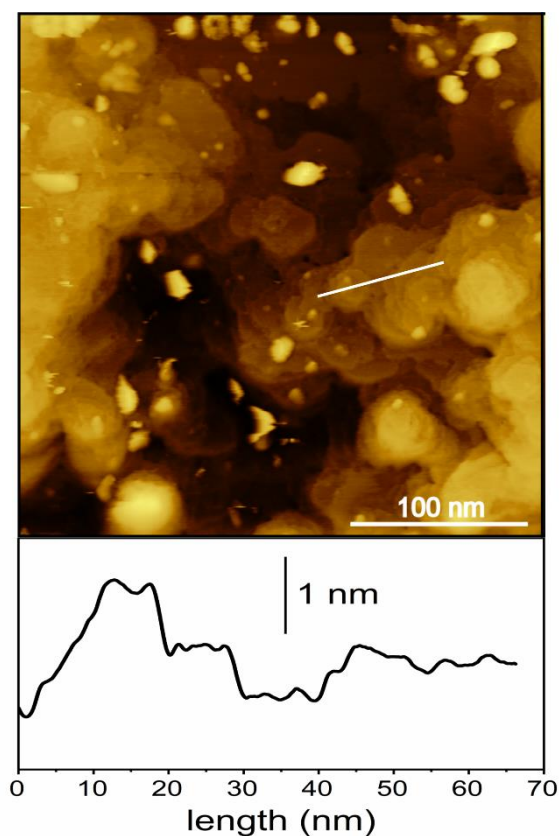


Figure 5.25: [122] EC-STM image [(300 × 300) nm²] depicting the filled states of the clean Cu(111) surface, obtained with $I_t = 1$ nA, $V_b = +1.1$ V and acquired at -0.3 V (D point in the CV in Figure 5.2), following the re-deposition process. The profile shown at the bottom was measured along the solid white line.

6.

Conclusion

This thesis has explored the intricate relationship between electrochemical phenomena and surface morphology, focusing specifically on vicinal Cu(111) surfaces. Through a detailed investigation of sulfate adsorption, surface restructuring, and the influence of surface geometry, we have provided a comprehensive understanding of how atomic-scale surface properties affect electrochemical behavior. The findings presented in this thesis offer critical insights into the role of surface structure in determining the dynamics of electrochemical processes, with important implications for both fundamental science and potential technological applications.

Particularly, vicinal surfaces, characterized by terraces and atomic steps, have been shown to play a crucial role in electrochemical reactivity. These surfaces, unlike flat basal planes, contain a large number of active sites, such as step edges and kinks, which are known to enhance catalytic performance. In this thesis, we investigated the Cu(111) vicinal surfaces, specifically Cu(221) and Cu(21 21 16), under sulfate adsorption conditions in acidic environments. These surfaces provide an ideal platform for studying how the physical confinement imposed by narrow terraces influences electrochemical processes.

The innovative aspect of this research lies in its approach to bridging the gap between well-established studies in vacuum-confined systems and the relatively

underexplored domain of nano-electrochemistry in real-world conditions. Miniaturization in vacuum environments, where physical confinement is a central factor in surface reactivity, has been extensively studied. However, when considering confined systems in electrochemical conditions, especially in the presence of specific electrolytes and at nanoscale dimensions, far less has been done. The goal of this research was specially to determine whether the same principles that govern reactivity in confined nano-systems in vacuum can be extended to nano-electrochemical systems. Specifically, this thesis introduces a novel approach: starting from a well-known electrochemical process, *i.e.*, the formation of the sulfate-induced Moiré-superstructure on the low-index Cu(111) plane, the study sought to track the evolution of the sulfate adlayer and of the long-range Moiré-superstructure when confined systems such as vicinal surfaces are introduced.

On Cu(111) surface, the sulfate-induced Moiré-superstructure emerges due to the lateral expansion of the outermost copper layer upon sulfate adsorption. The expansion creates a periodic mismatch between the first and second copper layers, resulting in the formation of a Moiré pattern. A detailed analysis revealed two possible orientations of these Moiré-units, crucial for understanding sulfate-induced restructuring. This surface reconstruction is driven by the interplay between the sulfate anions and the copper atoms: the linear expansion of the copper surface by approximately 6% results in significant changes in the local atomic environment. As copper atoms are displaced from the terraces, they form islands that are stabilized by the Moiré units. These islands, which can consist of one or more complete Moiré-units, represent a key feature of the sulfate-induced surface restructuring.

On vicinal surfaces, such as Cu(221) and Cu(21 21 16), the formation of the Moiré-superstructure is influenced by the *terrace width*. Nevertheless, under these real-world electrochemical conditions, electrochemistry proves to be a dominant force, capable of overcoming physical confinement effects. This is clearly demonstrated by the formation of islands on the vicinal Cu(21 21 16) surface, despite the physical constraints posed by the narrow terraces and steps. For

example, the principles governing the physical confinement of vicinal surfaces in vacuum include the fact that atoms near the steps are more reactive compared to those on flat terraces as well as the limited size of terraces between steps creates a physical confinement, that influences the spatial arrangement of adsorbates, affecting their ordering and self-organization on the surface. Instead, the behavior of Cu(21 21 16) surface is quite similar to what happens on the flat Cu(111) surface, and the Moiré islands form due to atoms that are expelled from the surrounding Cu terraces. The size and distribution of these islands are directly related to the width of the terraces, with wider terraces supporting larger islands due to the increased availability of displaced copper atoms. In addition, the Moiré-superstructure tends to "seal" the step edges, preventing further atom displacement from these regions. The research demonstrates that the vicinal surfaces exhibit unique electrochemical properties due to their geometric constraints: step edges, which are highly reactive sites, play a key role in adsorption processes, but the terraces themselves also contribute significantly to the overall electrochemical behavior. While step edges are important for initiating reactions, the terraces - particularly their width and spacing - dictate the long-range order of adsorbed species and surface reconstructions. On the Cu(221) surface, where the terraces are narrow (~0.73 nm), the Moiré-superstructure is constrained by the limited space, leading to terrace widening and the formation of rows of Moiré units. These findings suggest that surface processes near step edges are far more dynamic than previously thought and reopen the investigation into surface reactivity at step edges even on low-index Miller surfaces, like the Cu(111) case.

The thesis also investigates the effects of electrochemical cycling specifically on the Cu(111) surface up to the anodic dissolution and cathodic re-deposition potential regime. Using *in-situ* EC-STM and EC-AFM, we tracked the dynamic changes in surface morphology during these electrochemical processes. The results show that repeated dissolution and re-deposition cycles lead to a progressive roughening of the surface, with the once flat and ordered terraces becoming increasingly disordered. Before the corrosion process, the copper surface is characterized by large, flat terraces, typically around 200 nm in width.

However, after undergoing electrochemical cycling, the terraces shrink to about 100 nm or less. This reduction in terrace size is accompanied by the formation of roundish structures, which further alter the surface morphology. The roughness introduced by repeated cycles of dissolution and re-deposition demonstrates the irreversible nature of some electrochemical processes and underscores the challenges of maintaining surface stability in practical applications.

The findings of this thesis have important implications for the field of nano-electrochemistry and the design of advanced catalytic materials. The detailed characterization of sulfate-induced surface reconstructions provides valuable insights into the fundamental mechanisms that govern electrochemical reactions at the nanoscale. The research highlights the critical role of surface geometry, particularly the interplay between terrace width and step density, in dictating the behavior of adsorbed species and the formation of surface structures. In practical terms, these insights can be applied to the development of catalysts for a wide range of electrochemical reactions, including energy conversion and storage technologies, such as fuel cells and batteries. For example, the ability to control surface reconstruction through careful engineering of terrace widths and step edges could lead to the design of catalysts with enhanced reactivity and selectivity. By tailoring the atomic-scale structure of the catalyst surface, it may be possible to optimize the adsorption of reactants and the release of products, thereby improving the overall efficiency of the electrochemical process.

Looking forward, there are several promising avenues for future research that build on the findings of this thesis. One potential direction is the exploration of other anionic species (e.g., chlorides, phosphates, nitrates) and their interactions with vicinal copper surfaces. Different anions may induce distinct surface reconstructions, leading to new insights into the role of surface geometry in electrochemical behavior. Furthermore, extending these studies to other metals, such as gold or palladium, could provide a broader understanding of how surface structure influences electrochemical reactivity across a range of catalytic materials. Another exciting area for future exploration is the application of advanced *in-situ* spectroscopic techniques, such as shell-isolated nanoparticle-

enhanced Raman spectroscopy (SHINERS) or X-ray photoelectron spectroscopy (XPS), in conjunction with EC-STM and EC-AFM. These techniques could provide complementary information on the electronic structure and chemical composition of the surface during sulfate adsorption and re-deposition, offering a more holistic view of the electrochemical processes at play. Finally, the development of computational models to simulate the electrochemical behavior of vicinal surfaces would greatly complement experimental findings. By incorporating data on surface expansion, atomic displacement, and adsorption energies, it may be possible to predict the behavior of various surfaces under different electrochemical conditions, ultimately guiding the design of next-generation catalysts.

In conclusion, the results of this work indicate that both the terrace widening on Cu(221) and controlled island growth on Cu(21 21 16) are driven by the ordered adsorption of sulfate anions and the resulting expansion of the first copper layer. However, these electrochemical phenomena are controlled by a step-induced confinement effect related to the terrace width and step separation. The study also reveals that excess atoms expelled from the broader terraces of the Cu(21 21 16) surface are not incorporated at step edges but are captured by sulfate anions, forming energetically favorable SO_4^{2-} -covered islands. This observation aligns with the established fact that the Moiré structure induced by SO_4^{2-} begins to form at the step edges, where the displacement of Cu atoms is initially easiest. Once the steps are "decorated" with Moiré units, they become sealed and inert, preventing further liberation of Cu atoms. The observed correlation between island size and local terrace width suggests that the expelled copper atoms remain within the region of most probable displacement, highlighting the **complex interplay between electrochemical processes and surface topography in nanoscale environments**.

References

- [1] S. Lin, X. Chen and Z. Lin Wang, "Electron transfer in liquid–solid contact electrification and double-layer formation," in *Encyclopedia of solid-liquid interfaces*, Elsevier, 2023, pp. 576-599.
- [2] B. Tadesse, C. Owusu and B. Albijanic, "Solid-liquid interfaces in mineral processing," in *Encyclopedia of solid-liquid interfaces*, Elsevier, 2023, pp. 485-193.
- [3] Ø. G. Martinsen and A. Heiskanen, "Chapter 7 - Electrodes," in *Bioimpedance and bioelectricity basics*, Academic Press, 2023, pp. 175-248.
- [4] P.-A. Mante and C.-K. Sun, "Coherent phonon spectroscopy of solid/liquid interfaces," in *Encyclopedia of solid-liquid interfaces*, Elsevier, 2023, pp. 136-147.
- [5] C. Liu and Y. Meng, "Tribology at charged solid-liquid interfaces," in *Encyclopedia of solid-liquid interfaces*, Elsevier, 2023, pp. 581-588.
- [6] D. J. Davidson, "Exnovating for a renewable energy transition," *nature energy*, vol. 4, p. 254–256, 2019.
- [7] J. Duan, S. Chen, C. A. Ortíz-Ledón, M. Jaroniec and S.-Z. Qiao, "Phosphorus vacancies that boost electrocatalytic hydrogen evolution by two orders of magnitude," *Angewandte Chemie*, vol. 59, p. 8181, 2020.
- [8] H. Liu, Q. He, H. Jiang, Y. Lin, Y. Zhang, M. Habib, S. Chen and L. Song, "Electronic structure reconfiguration toward pyrite NiS₂ via engineered heteroatom defect boosting overall water splitting," *ACS Nano*, vol. 11, no. 11, 2017.

- [9] C. Tang, Y. Jiao, B. Shi, J.-N. Liu, Z. Xie, X. Chen, Q. Zhang and S.-Z. Qiao, "Coordination tunes selectivity: two-electron oxygen reduction on high-loading molybdenum single-atom catalysts," *Angewandte Chemie*, vol. 59, no. 23, pp. 9171-9176, 2020.
- [10] H.-F. Wang e Q. Xu, «Materials design for rechargeable metal-air batteries,» *Matter*, vol. 1, n. 3, pp. 565-595, 2019.
- [11] Y. Zhang, Y. Lin, T. Duan and L. Song, "Interfacial engineering of heterogeneous catalysts for electrocatalysis," *materials today*, vol. 48, pp. 115-134, 2021.
- [12] E. Ghali, W. Dietzel and K.-U. Kainer, "General and localized corrosion of magnesium alloys: A critical review," *Journal of Materials Engineering and Performance*, vol. 13, no. 1, pp. 7-23, 2004.
- [13] G. T. Burstein, C. Liu, R. M. Souto and S. P. Vines, "Origins of pitting corrosion," *Corrosion Engineering, Science and Technology*, vol. 39, no. 1, pp. 25-30, 2004.
- [14] A. K. Yagati, J. Min and J.-W. Choi, "Electrochemical Scanning Tunneling Microscopy (ECSTM) – From theory to future applications," in *Modern electrochemical methods in nano, surface and corrosion science*, Mahmood Aliofkhazraei, 2014.
- [15] J. Lipkowski and P. N. Ross, *Structure of electrified interfaces*, New York: VCH Publishers, 1993.
- [16] H. Siegenthaler and A. A. Gerwith, *Nanoscale probes of the solid/liquid interface*, Dordrecht: Springer, 1996.
- [17] N. Masuko, T. Osaka and Y. Fukunaka, *New trends and approaches in electrochemical technology*, Tokyo: Kondasha, VCH, 1993.

-
- [18] A. A. Gewirth and H. Siegenthaler, *Nanoscale probes of the solid liquid interface*, London: Kluwer Academic Publishers, 1995.
- [19] J. G. Becerra, R. C. Salvarezza and A. J. Arvia, "The influence of slow $\text{Cu}(\text{OH})_2$ phase formation on the electrochemical behaviour of copper in alkaline solutions," *Electrochimica Acta*, vol. 33, no. 5, p. 613–621, 1988.
- [20] H. Siegenthaler, "STM in electrochemistry," in *Scanning Tunneling Microscopy II*, Springer, 1995, pp. 7-49.
- [21] A. A. Gewirth and B. K. Niece, "Electrochemical applications of in-situ scanning probe microscopy," *Chemical Reviews*, vol. 97, no. 4, p. 1129–1162, 1997.
- [22] H.-H. Strehblow and B. Titze, "The investigation of the passive behaviour of copper in weakly acid and alkaline solutions and the examination of the passive film by ESCA and ISS," *Electrochimica Acta*, vol. 25, no. 6, pp. 839-850, 1980.
- [23] S. Ye, T. Kondo, N. Hoshi, J. Inukai, S. Yoshimoto, M. Osawa and K. Itaya, "Recent progress in electrochemical surface science with atomic and molecular levels," *Electrochemistry*, vol. 77, no. 1, pp. 2-20, 2009.
- [24] M. Nowicki and K. Wandelt, "Metal–electrolyte interfaces," in *Surface and interface science: interfacial electrochemistry*, Wiley-VCH, 2020, p. Chapter 57.
- [25] A. C. Society, "Electrochemistry at the nanoscale: tackling old questions, posing new ones," *Accounts of Chemical Research*, vol. 49, no. 11, pp. 2371-2668, 2016.

- [26] J. M. Feliú, E. Herrero and V. Climent, "Electrocatalytic properties of stepped surfaces," in *Catalysis in electrochemistry: from fundamentals to strategies for fuel cell development*, John Wiley & Sons, Inc., 2011, pp. 127-163.
- [27] V. Climent and J. M. Feliu, "Surface electrochemistry with Pt single-crystal electrodes. Advances in electrochemical science and engineering," in *Nanopatterned and nanoparticle-modified electrodes*, Wiley-VCH Verlag GmbH & Co. KGaA., 2017, pp. 1-57.
- [28] E. Le Goff, L. Barbier, L. Masson and B. Salanon, "Vicinal surfaces: free energy, terrace width distribution and step correlation functions," *Surface Science*, vol. 432, no. 1-2, pp. 139-154, 1999.
- [29] S. Rousset, V. Repain, G. Baudot, Y. Garreau and J. Lecoer, "Self-ordering of Au(111) vicinal surfaces and application to nanostructure organized growth," *Journal of Physics: Condensed Matter*, vol. 15, no. 47, p. S3363, 2003.
- [30] M. Giesen, U. Linke and H. Ibach, "Restructuring of the vicinal Cu(997) surface," *Surface Science*, vol. 389, no. 1-3, pp. 264-271, 1997.
- [31] Y. Qiao and B. Seger, "Recent advances in single crystal and facet dependency of copper electrodes on electrochemical CO₂ reduction," *Current Opinion in Chemical Engineering*, vol. 43, p. 100999, 2024.
- [32] I. T. McCrum, X. Chen, K. A. Schwarz, M. J. Janik and M. T. M. Koper, "Effect of step density and orientation on the apparent pH dependence of hydrogen and hydroxide adsorption on stepped platinum surfaces," *The Journal of Physical Chemistry C*, vol. 122, no. 29, 2018.

-
- [33] Y. H. Fang and Z.-P. Liu, "Surface phase diagram and oxygen coupling kinetics on flat and stepped Pt surfaces under electrochemical potentials," *Journal of Physical Chemistry C*, vol. 113, p. 9765–9772, 2009.
- [34] G. A. Attard, C. Harris, E. Herrero and J. Feliu, "The influence of anions and kink structure on the enantioselective electro-oxidation of glucose," *Faraday Discussions*, vol. 121, 2002.
- [35] X. Liu, P. Schlexer, J. Xiao, Y. Ji, L. Wang, R. B. Sandberg, M. Tang, K. S. Brown, H. Peng, S. Ringe and C. Hahn, "pH effects on the electrochemical reduction of CO(2) towards C2 products on stepped copper," *Nature Communications*, vol. 10, no. 1, p. 9, 2019.
- [36] T. H. Phan and K. Wandelt, "Self-assembly of metal free porphyrin layers at copper-electrolyte interfaces: Dependence on substrate symmetry," *Surface Science*, vol. 607, pp. 82-91, 2013.
- [37] N. Hai, B. Gasparovic, K. Wandelt and P. Broekmann, "Phase transition in ordered porphyrin layers on iodide modified Cu(1 1 1): An EC-STM study," *Surface Science*, p. 2597–2602, 2007.
- [38] J. M. Gottfried, "Surface chemistry of porphyrins and phthalocyanines," *Surface Science Reports*, vol. 70, no. 3, pp. 259-379, 2015.
- [39] T. M. T. Huynh, T. H. Phan, P. H. Nguyen and K. Wandelt, "Self-assembly of porphyrin molecules on a Cu(111) electrode: Influence of different anions and electrode potential," *Surface Science*, vol. 694, p. 121554, 2020.
- [40] L. A. Kibler, "Preparation and characterization of noble metal single crystal electrode surfaces," International Society of Electrochemistry, Ulm, Germany, 2003.

- [41] B. Madry, I. Morawski, T. Kosmala, K. Wandelt and M. Nowicki, "Porphyrin layers at Cu/Au(111)–electrolyte interfaces: in situ EC-STM study," *Topics in Catalysis*, vol. 61, pp. 1335-1349, 2018.
- [42] T. H. Phan, S. Breuer, U. Hahn, D. T. Pham, T. Torres and K. Wandelt, "Unusual demetalation and ordered adsorption of a pyridine-appended zinc phthalocyanine at metal–electrolyte interfaces studied by in situ Scanning Tunneling Microscopy and x-ray photoelectron spectroscopy," *The Journal of Physical Chemistry C*, vol. 118, no. 1, pp. 457-467, 2013.
- [43] T. Kosmala, R. Wasielewski, M. Nowicki and K. Wandelt, "Unveiling the interplay between a Au(100) electrode, adsorbed TTMAPP porphyrin cations, and iodide anions: an EC-STM and CV study," *The Journal of Physical Chemistry C*, vol. 128, p. 1773–1789, 2024.
- [44] T. Kosmala, M. Blanco, G. Granozzi and K. Wandelt, "Potential driven non-reactive phase transitions of ordered porphyrin molecules on iodine-modified Au(100): an electrochemical Scanning Tunneling Microscopy (EC-STM) study," *surfaces*, vol. 1, pp. 12-28, 2018.
- [45] R. Lindstrom, V. Maurice, L. Klein and P. Marcus, *The use of Electrochemical Scanning Tunnelling Microscopy (EC-STM) in corrosion analysis*, 2006: Woodhead Publishing, 44.
- [46] P. C. Andricacos, C. Uzoh, J. O. Dukovic, J. Horkans and H. Deligianni, "Damascene copper electroplating for chip interconnections," *IBM Journal of Research and Development*, vol. 42, no. 5, pp. 567-574, 1998.
- [47] B. Wohlmann, Z. Park, M. Kruff, C. Stuhlmann and C. Wandelt, "An in-situ and ex-situ study of chloride adsorption on Cu(111) electrodes in dilute HCl solutions," *Colloids and Surfaces*, vol. 134, pp. 15-19, 1998.

-
- [48] M. Wilms, P. Broekmann, M. Kruft, C. Stuhlmann and K. Wandelt, "STM investigation of step orientation and surface dynamics of Cu(111) in hydrochloric acid electrolyte," *Applied Physics A*, vol. 66, p. S473–S475, 1998.
- [49] J. Kunze, V. Maurice, L. H. Klein, H.-H. Strehblow and P. Marcus, "In situ STM study of the effect of chlorides on the initial stages of anodic oxidation of Cu(111) in alkaline solutions," *Electrochimica Acta*, vol. 48, pp. 1157-1167, 2003.
- [50] J. Kunze-Liebhauser, "Electrochemical Scanning Tunneling Microscopy studies of copper oxide formation - a review," Elsevier, Innsbruck, 2018.
- [51] J. Kunze, V. Maurice, L. H. Klein, H.-H. Strehblow and P. Marcus, "In situ scanning tunneling microscopy study of the anodic oxidation of Cu(111) in 0.1 M NaOH," *The Journal of Physical Chemistry B*, vol. 105, p. 4263–4269, 2001.
- [52] J. Kunze, V. Maurice, L. H. Klein, H.-H. Strehblow and P. Marcus, "In situ STM study of the anodic oxidation of Cu(0 0 1) in 0.1 M NaOH," *Journal of Electroanalytical Chemistry*, Vols. 554-555, no. 1, pp. 113-125, 2003.
- [53] V. Maurice, H.-H. Strehblow and P. Marcus, "In situ STM study of the initial stages of oxidation of Cu(111) in aqueous solution," *Surface Science*, vol. 458, no. 1-3, pp. 185-194, 2000.
- [54] D. Friebel, T. Mangan, B. Obliers, C. Schlaup, P. Broekmann and K. Wandelt, "On the existence of ordered organic adlayers at the Cu(111)/electrolyte interface," *Langmuir*, vol. 20, pp. 2803-2806, 2004.

- [55] P. Broekmann, M. Wilms, M. Kruff, C. Stuhlmann and K. Wandelt, "In-situ STM investigation of specific anion adsorption on Cu(111)," *Journal of Electroanalytical Chemistry*, vol. 467, pp. 307-324, 1999.
- [56] M. Wilms, P. Broekmann, C. Stuhlmann and K. Wandelt, "In situ STM investigation of adsorbate structures on Cu(111) in sulfuric acid electrolyte," *Surface Science*, vol. 416, pp. 121-140, 1998.
- [57] M. Lennartz, P. Broekmann, M. Arenz, C. Stuhlmann and K. Wandelt, "Sulfate adsorption on Cu(111) studied by in-situ IRRAS and STM: revealing the adsorption site and desorption behavior," *Surface Science*, vol. 442, no. 2, pp. 215-222, 1999.
- [58] P. Broekmann, M. Wilms, A. Spaenig and K. Wandelt, "Highly ordered adsorbate structures on Cu(111) in the potential regime of hydrogen evolution-An in-situ STM study," in *Thin films: preparation, characterization, applications*, Soriaga, M. P.; Stickney, J.; Bottomley, L. A.; Kim, Y.-G., 2002, p. pp 1-16.
- [59] M. M. Lohrengel, J. W. Schultze, H. D. Speckmann and H.-H. Strehblow, "Growth, corrosion and capacity of copper oxide films investigated by pulse techniques," *Electrochimica Acta*, vol. 32, no. 5, pp. 733-742, 1987.
- [60] P. Broekmann, M. Wilms, M. Arenz, A. Spaenig and K. Wandelt, "Atomic structure of Cu(111) surfaces in dilute sulfuric acid solution," in *Solid-liquid interfaces - Macroscopic phenomena - Microscopic understanding*, Berlin Heidelberg, Springer - Verlag, Wandelt, K.; Thurgate, S., 2003, p. 159.
- [61] V. Maurice, L. H. Klein, H.-H. Strehblow and P. Marcus, "In situ STM Study of the initial stages of anodic oxidation of Cu(111) in the presence of sulfates," *Journal of the Electrochemical Society*, vol. 150, p. B316, 2003.

-
- [62] P. Broekmann, M. Wilms and K. Wandelt, "Atomic structures of a Cu(111) surface under electrochemical conditions: an in-situ STM study," *Surface Review and Letters*, vol. 6, no. 5, p. 907–916, 1999.
- [63] M. Arenz, P. Broekmann, M. Lennartz, E. Vogler and K. Wandelt, "In-situ characterization of metal/electrolyte interfaces: sulfate adsorption on Cu(111)," *physica status solidi (a)*, vol. 187, no. 1, p. 63–74, 2001.
- [64] A. Frumkin, "Wasserstoffüberspannung und struktur der doppelschicht," *Zeitschrift für physikalische Chemie*, vol. 164A, p. 121, 1933.
- [65] M. Wilms, M. Kruft, G. Bermes and K. Wandelt, "A new and sophisticated electrochemical Scanning Tunneling Microscope design for the investigation of potentiodynamic processes," *Review of Scientific Instruments*, vol. 70, p. 3641–3650, 1999.
- [66] A. Groß and S. Sakong, "Modelling the electric double layer at electrode-electrolyte," *Current Opinion in Electrochemistry*, vol. 14, pp. 1-6, 2019.
- [67] N. Bruch, M. Eikerling and J. Huang, "Density-potential functional theory of metal-solution interfaces," in *Encyclopedia of solid-liquid interfaces*, Elsevier, 2023, pp. 308-331.
- [68] H. Helmholtz, "Studien über elektrische grenzsichten," *Annalen der Physik*, vol. 243, no. 7, pp. 337-382, 1879.
- [69] H. Helmholtz, "Ueber einige gesetze der vertheilung elektrischer ströme in körperlichen leitern mit anwendung auf die thierisch-elektrischen versuche," *Annalen der Physik*, vol. 165, no. 6, pp. 211-233, 1853.

- [70] V. Maunier, J. Huang, G. Feng, R. Qiao and B. G. Sumpter, "Modern theories of carbon-based electrochemical capacitors: a short review," in *Proceedings of the Computational Clean Energy Symposium*, Vancouver, Canada, 2010.
- [71] M. Gouy, "Sur la constitution de la charge électrique à la surface d'un électrolyte," *J. Phys. Theor. Appl.*, vol. 9, no. 1, pp. 457-468, 1910.
- [72] O. Stern, "Zur theorie der elektrolytischen doppelschicht," *Zeitschrift für Elektrochemie und angewandte physikalische Chemie*, vol. 30, pp. 508-516, 1924.
- [73] H. Gerischer, "The Impact of semiconductors on the concepts of electrochemistry," *Electrochimica Acta*, vol. 35, pp. 1677-1699, 1990.
- [74] D. Baird, A. Nordmann and J. Schummer, "Discovering the nanoscale," IOS Press, Amsterdam, 2004.
- [75] G. Binnig and H. Rohrer, "Scanning Tunneling Microscopy," *IBM Journal of Research and Development*, vol. 69, pp. 355-358, 1986.
- [76] G. Granek and G. Hon, "Searching for asses, finding a kingdom: the story of the invention of the scanning tunnelling microscope (STM)," *Annals of Science*, vol. 65, no. 1, pp. 101-125, 2008.
- [77] N. D. Lang and W. Kohn, "Theory of metal surfaces: work function," *Physical Review B*, vol. 3, no. 4, pp. 1215-1222, 1971.
- [78] G. Binnig and H. Rohrer, "Scanning tunneling microscopy," *Surface Science*, vol. 126, no. 1-3, pp. 236-244, 1983.
- [79] J. E. Griffith and G. P. Kochanski, "Scanning Tunneling Microscopy," *Annual Review of Materials Research*, vol. 20, pp. 219-244, 1990.
- [80] R. M. Osgood, JR. and X. Wang, "Image states on single-crystal metal," *Solid State Physics*, vol. 51, pp. 1-80, 1998.

-
- [81] J. Tersoff and D. R. Hamann, "Theory of the scanning tunneling microscope," *Physical Review B*, vol. 31, no. 2, pp. 805-813, 1985.
- [82] nanoScience Instruments, "Scanning Tunnelling Microscopy," [Online]. Available: <https://www.nanoscience.com/techniques/scanning-tunneling-microscopy/>. [Accessed 2024].
- [83] J. Bardeen, "Tunnelling from a many-particle point of view," *Physical Review Letters*, vol. 6, no. 2, pp. 57-59, 1961.
- [84] T. Albrecht, "Electrochemical tunnelling sensors and their potential applications," *nature communications*, vol. 3, no. 829, 2012.
- [85] J. Ulstrup, "Solid-electrolyte tunnelling," *Surface Science*, vol. 101, no. 1-3, pp. 564-582, 1980.
- [86] T. O. Schmidt, R. W. Haid, E. L. Gubanov, R. Kluge and A. S. Bandarenka, "Electrochemical Scanning Tunneling Microscopy as a tool for the detection of active electrocatalytic sites," *Topics in Catalysis*, vol. 66, no. 15-16, pp. 1-10, 2023.
- [87] D. M. Kolb, "Electrochemical Surface Science," *Angewandte Chemie*, vol. 40, no. 7, pp. 1162-1181, 2001.
- [88] F. Endres and S. Z. El Abedin, "In situ Scanning Tunnelling Microscopy in ionic liquids: prospects and challenges," *Zeitschrift für Physikalische Chemie*, vol. 221, no. 9-10, pp. 1407-1427, 2007.
- [89] R. W. Gurney, "The quantum mechanics of electrolysis," *Proceedings of the Royal Society A: Mathematical, Physical and Engineering Sciences*, vol. 134, no. 823, pp. 137-154, 1931.

- [90] J. Gomez, L. Vazquez, A. M. Baro, N. Garcia, C. L. Perdriel, W. E. Triaca and A. J. Arvia, "Surface topography of (100)-type electrofaceted platinum from scanning tunneling microscopy and electrochemistry," *Nature*, vol. 323, pp. 448-450, 1986.
- [91] R. Sonnenfeld and P. K. Hansma, "Atomic-resolution microscopy in water," *Science*, vol. 232, pp. 211-213, 1986.
- [92] P. Lustenberger, H. Rohrer, R. Christoph and H. Siegenthaler, "Scanning Tunneling Microscopy at potential controlled electrode surfaces in electrolytic environment," *Journal of Electroanalytical Chemistry*, vol. 243, pp. 225-235, 1988.
- [93] K. Itaya e E. Tomita, «Scanning Tunneling Microscope for electrochemistry-A new concept for the In Situ Scanning Tunneling Microscope in electrolyte solution,» *Surface Science*, vol. 201, pp. L507-L512, 1988.
- [94] D. W. Suggs and A. J. Bard, "Scanning Tunneling Microscopic Study With Atomic Resolution of the Dissolution of Cu(111) in Aqueous Chloride Solutions," *Journal of the American Chemical Society*, vol. 116, p. 10725–10733, 1994.
- [95] D. W. Suggs and A. J. Bard, "Scanning Tunneling Microscopic Study With Atomic Resolution of the Dissolution of Cu(100) Electrodes in Aqueous Chloride Media," *Journal of Physical Chemistry*, vol. 99, p. 8349–8355, 1995.
- [96] J. Wiechers, T. Twomey, D. M. Kolb and R. J. Behm, "An in situ Scanning Tunneling Microscopy study of Au(111) with atomic scale resolution," *Journal of Electroanalytical Chemistry*, vol. 248, pp. 451-460, 1988.

-
- [97] A. M. Bittner, J. Wintterlin, B. Beran and G. Ertl, "Bromine adsorption on Pt(111), Pt(100), and Pt(110)-An STM study in air and in electrolyte," *Surface Science*, vol. 335, pp. 291-299, 1995.
- [98] A. M. Bittner, J. Wintterlin and G. E. Ertl, "Effects of iodine coating and desorption on the reconstruction of a Pt(110) electrode: a Scanning Tunnelling Microscopy study," *Journal of Electroanalytical Chemistry*, vol. 388, pp. 225-231, 1995.
- [99] D. M. Kolb, R. Ullmann and T. Will, "Nanofabrication of small copper clusters on gold(111) electrodes by a Scanning Tunneling Microscope," *Science*, vol. 275, p. 1097-1099, 1997.
- [100] O. M. Magnussen, J. Hotlos, G. Beitel, D. M. Kolb and R. J. Behm, "Atomic structure of ordered copper adlayers on single-crystalline gold electrodes," *Journal of vacuum science & technology. B, Microelectronics and nanometer structures*, vol. 9, p. 969, 1991.
- [101] G. Serrano, B. Bonanni, M. Di Giovannantonio, T. Kosmala, M. Schmid, U. Diebold, A. Di Carlo, J. Cheng, J. VandeVondele, K. Wandelt and C. Goletti, "Molecular Ordering at the Interface Between Liquid Water and Rutile TiO₂(110)," *Advanced Materials Interfaces*, vol. 2, no. 17, p. 1500246, 2015.
- [102] S. Morita, F. J. Giessibl, E. Meyer and R. Wiesendanger, *Non-contact Atomic Force Microscopy*, Springer, 2015.
- [103] D. Rugar and P. Hansma, "Atomic Force Microscopy," *Physics Today*, vol. 43, no. 10, pp. 23-30, 1990.
- [104] R. García and A. San Paulo, "Attractive and repulsive tip-sample interaction regimes in tapping-mode atomic force microscopy," *Physical Review B*, vol. 60, p. 4961, 1999.

- [105] P. K. Hansma, J. P. Cleveland, M. Radmacher, D. A. Walters, M. Bezanilla, M. Fritz, D. Vie, H. G. Hansma, C. B. Prater, J. Massie, L. Fukunaga, J. Gurley and V. Elings, "Tapping mode atomic force microscopy in liquids," *Applied Physics Letters*, vol. 64, no. 13, pp. 1738-1740, 1994.
- [106] J. E. Lennard-Jones, "Cohesion," *Proceedings of the Physical Society*, vol. 43, no. 5, p. 461, 1931.
- [107] B. Cappella and G. Dietler, "Force-distance curves by atomic force microscopy," *Surface Science Reports*, vol. 34, no. 1-3, pp. 5-104, 1999.
- [108] M. S. Bradley R. A., "The cohesive force between solid surfaces and the surface energy of solids," *The London, Edinburgh, and Dublin Philosophical Magazine and Journal of Science*, vol. 13, no. 86, pp. 853-862, 1932.
- [109] K. L. Johnson, K. Kendall and A. D. Roberts, "Surface energy and the contact of elastic solids," *Proceeding of The Royal Society A*, vol. 324, no. 1558, pp. 301-313, 1971.
- [110] A. J. Bard and L. R. Faulkner, *Electrochemical methods: fundamentals and applications*, New York: Wiley, 2000.
- [111] K. H. Bevan, Y. W. Foong, J. Shirani, S. Yuan and S. A. Farraj, "Physics applied to electrochemistry: Tunneling reactions," *Journal of Applied Physics*, vol. 129, no. 9, 2021.
- [112] J. Zhang, A. M. Kuznetsov, I. G. Medvedev, Q. Chi, T. Albrecht, P. Jensen and J. Ulstrup, "Single-molecule electron transfer in electrochemical environments," *Chemical Reviews*, vol. 108, no. 7, pp. 2737-2791, 2008.

-
- [113] J. C. Tully, "Perspective: Nonadiabatic dynamics theory," *The Journal of Chemical Physics*, vol. 137, no. 22, 2012.
- [114] C. E. D. Chidsey, "Free energy and temperature dependence of electron transfer at the metal-electrolyte interface," *Science*, vol. 251, no. 4996, pp. 919-922, 1991.
- [115] M. S. Hossain and A. I. H. Bevan, "Interfacial screening in ultrafast voltammetry: A theoretical study of redox-active monolayers," *Analytical Chemistry*, vol. 88, no. 18, p. 9062–9070, 2016.
- [116] Z. Ahmad, *Principle of corrosion engineering and corrosion control*, Butterworth-Heinemann, Elsevier, 2006.
- [117] B. Joos, T. L. Einstein and N. C. Bartel, "Distribution of terrace widths on a vicinal surface within the one-dimensional free fermion model," *Physical Review B*, vol. 43, no. 10, pp. 8153-8162, 1991.
- [118] F. Finocchi, P. Geysers and A. Bourgeois, "The role of hydroxylation on the step stability and on the interaction between steps on MgO surfaces: a first-principles study.," *Physical Chemistry Chemical Physics*, vol. 14, pp. 13692-13701, 2012.
- [119] A. Mugarza, F. Schiller, J. Kuntze, J. Cordon, M. Ruiz-Osés and J. E. Ortega, "Modelling nanostructures with vicinal surfaces," *Journal of Physics: Condensed Matter*, vol. 18, p. S27–S49, 2006.
- [120] *Keysight 5500 Scanning Probe Microscope user's guide*, Keysight Technologies.
- [121] C. Filoni, *Reactive dissolution of organic nanocrystals at controlled pH*, Master's Thesis - Politecnico di Milano, 2019/2020.

- [122] C. Filoni, K. Wandelt, L. Marfori, M. Leone, L. Duò, F. Ciccacci and G. Bussetti, "A combined EC-STM and EC-AFM investigation of the sulfate adsorption on a Cu(111) electrode surface up to the anodic corrosion potential," *Applied Surface Science*, vol. 611, p. 155542, 2023.
- [123] Z. Ahmad, "Basic concepts in corrosion," in *Principles of corrosion engineering and corrosion control*, Butterworth-Heinemann, Elsevier, 2006, p. 9–56.
- [124] G. Inzelt, A. Lewenstam and F. Scholz, *Handbook of reference electrodes*, Springer, 2013.
- [125] B. M. Tackett, D. Raciti, A. R. Hight Walker and T. P. Moffat, "Surface hydride formation on Cu(111) and its decomposition to form H₂ in acid electrolyte," *The Journal of Physical Chemistry Letters*, vol. 12, no. 44, p. 10936–10941, 2021.
- [126] T. M. T. Huynh and P. Broekmann, "From in situ towards in operando conditions: scanning tunneling microscopy study of hydrogen intercalation in Cu(111) during hydrogen evolution," *ChemElectroChem*, vol. 1, pp. 1271-1274, 2014.
- [127] C. Filoni, K. Wandelt, P. Broekmann, M. Wilms, R. Yivlialin, L. Duò, F. Ciccacci and G. Bussetti, "Physical confinement versus adsorption driven reconstruction: the case of sulfate anion interaction with vicinal Cu(111) surfaces," *Electrochimica Acta*, p. 144885, 2024.
- [128] P. Broekmann, M. Wilms, A. Spaenig and K. Wandelt, "Morphological aspects of sulfate-induced reconstruction of Cu(1 1 1) in sulfuric acid solution: in situ STM study," *Progress in Surface Science*, vol. 67, no. 1-8, pp. 59-77, 2001.